ABSTRACT

ALDRIDGE, BETH ELLEN. Further Development of the Application of Adaptive Model Refinement to Nuclear Reactor Core Simulation. (Under the direction of Paul Turinsky.)

Designing the core of a nuclear power reactor is an intricate process, as there are many requirements that must be met. In order to ensure that the reactor can be operated safely, it is important to be able to predict the behavior of the core. Computational simulations of reactor behavior are based on mathematical models that can meet nearly any desired level of fidelity, though higher fidelity usually comes with a higher computational cost. There are many techniques available for optimizing the fidelity to cost ratio. This work explores and further develops the Adaptive Model Refinement (AMoR) technique introduced in the Master's thesis of Sterling Satterfield [1]. The AMoR technique is designed to integrate two or more different fidelity simulation models to create a hybrid model which can provide high accuracy solutions faster.

This proof of concept for applying AMoR to nuclear reactor neutron simulation employs as low-fidelity a point reactor kinetics solver (PKE-Solver) and as high-fidelity, the few-group diffusion code NESTLE [2]. The low-fidelity model uses an adaption of the Quasi-Static method [3] to convert the PKE-solver results into a 3-dimensional flux and delayed neutron precursor solution. The adaptation is based on the concept of the flux being separable into amplitude and shape functions. The low-fidelity solution is compared to the high fidelity solution via assorted error metrics.

This continuation undertook completing the low-fidelity solution method, expanding its modeling capabilities, determining sensitivities in the method, and optimizing the low-fidelity results. This work focused on a low-fidelity solution that was developed to enable active switching between the low-fidelity solution and the high-fidelity solution when error was deemed to be too large. The primary test cases were a 2 second and a 120 second rod insertion transient. Through the various improvements found in this work, the maximum locally normalized flux and precursor concentration errors were reduced to ~9-13% and ~3.5-14% respectively.

© Copyright 2015 Beth Ellen Aldridge

All Rights Reserved

Further Development of the Application of Adaptive Model Refinement to Nuclear Reactor Core Simulation

by
Beth Ellen Aldridge

A thesis submitted to the Graduate Faculty of
North Carolina State University
in partial fulfillment of the
requirements for the Degree of
Master of Science

Nuclear Engineering

Raleigh, North Carolina

2015

APPROVED BY:

Dmitriy Anistratov

Robert White

Paul Turinsky

Chair of Advisory Committee

BIOGRAPHY

Beth Ellen Aldridge was born in Hawaii, USA to Lee and Liza Rosenberg. After a childhood spent in various coastal cities, she obtained her Bachelor of Science degree in Nuclear Engineering from University of California, Berkeley in 2006. Upon graduation, she worked as an officer in the US Navy as a Nuclear Power School instructor for four years, teaching physics and reactor principles to prospective navy nuclear operators. Beth received an honorable discharge and left the navy in 2010. She then worked for the Tennessee Valley Authority as an Operations Instructor at a nuclear power plant, during which time she married Matthew Aldridge. In 2013 they moved to Raleigh, North Carolina where Beth pursued a master's degree in Nuclear Engineering.

TABLE OF CONTENTS

LIST OF FIGURES v
1. Introduction 1
1.1 Overview 1
1.2 Theoretical basis 2
1.3 NESTLE 4
1.4 Point Kinetics and Quasi-static Method 5
1.5 PKE-solver 6
1.6 Adaptive Model Refinement 7
2. Methodology 8
2.1 Projection Operator Production 8
2.2 Low-Fidelity Projection and Precursor prediction 11
2.3 Hereditary AMoR Setup 12
2.4 Active Switching Concept & Methodology 16
2.5 Hereditary Error Metrics 17
2.6 Additional Error Metrics 19
3. Results 22
3.1 Test Setup 22
3.2 The Hybrid Low-Fidelity Model 24
3.2.1 Original Precursor Error 26
3.2.2 Reducing Precursor Error 29
3.2.3 New AMoR Layout 35
3.2.4 Additional Modifications 37
3.3 Improving the Low-Fidelity Model 43
3.3.1 Flux-shape Error Source 44
3.3.2 Prompt Neutron Induced Error Tests 49
3.3.3 Shape-Factor Optimization 55
3.3.4 Projection Operator Frequency 63
3.3.5 Active Switching Parameter Tests 66
3.3.6 Delayed Neutron Effect Analysis 75
3.3.7 Isolation Test of Distribution Effects 85

4. Conclusions and Recommendations:.....97
4.1 Future Work.....98
REFERENCES.....99
APPENDIX.....100

LIST OF FIGURES

Figure 1: Required runs in NESTLE and PKE-solver to produce a full high-fidelity vs. low-fidelity comparison in the original and current AMoR setups. 13
Figure 2: Original low-fidelity AMoR setup. 14
Figure 3: AMoR input to GPT responses.....21
Figure 4: Maximum flux error for 25 steady-state projection operator sets. 24
Figure 5: Hot-spot flux error for 25 steady-state projection operator sets. 25
Figure 6: Maximum flux error for 0.002 second rapid-insertion projection operator sets. 25
Figure 7: Hot-spot flux error for 0.002 second rapid-insertion projection operator sets. 26
Figure 8: Maximum precursor error for 25 steady-state projection operator sets. 27
Figure 9: RMS precursor error for 25 steady-state projection operator sets.....27
Figure 10: Maximum precursor error for 0.002 second rapid-insertion projection operator sets. 28
Figure 11: RMS precursor error for 0.002 second rapid-insertion projection operator sets. 28
Figure 12: Maximum precursor error for rapid-insertion projection operators hybrid method. 30
Figure 13: RMS precursor error for rapid-insertion projection operators hybrid method. 30
Figure 14: RMS flux error for 0.002 second rapid-insertion projection operators hybrid method, with one switch halfway through the 2 second transient. 31
Figure 15: RMS flux error for rapid-insertion projection operators with suppressed DNPs and projected precursors method, with one switch halfway through the 2 second transient. 32
Figure 16: Neutron flux vs. Rod Height at a non-rodded location.....33
Figure 17: Neutron flux vs. Rod Height, zoomed in, at a non-rodded location. 34
Figure 18: Current AMoR setup.....36
Figure 19: 2 second rod withdrawal transient average neutron density. 38
Figure 20: 2 second rod withdrawal transient maximum flux error. 38
Figure 21: 2 second rod withdrawal transient RMS flux error. 39
Figure 22: 2 second rod withdrawal transient maximum precursor error.....39
Figure 23: 2 second rod withdrawal transient RMS precursor error. 40
Figure 24: 2 second rod insertion, RMS flux-shape error extended 41
Figure 25: 2 second rod insertion, maximum flux-shape error extended, with restart. 42
Figure 26: 2 second transient flux error components. 43
Figure 27: Average neutron density, 2 second rod insertion, normal beta values.....44
Figure 28: Average neutron density, 2 second rod insertion, 0.0001 beta values.....45
Figure 29: Average neutron density, 2 second rod insertion, 0.00001 beta values.....45

Figure 30: RMS flux error, 2 second transient, normal beta values, 0.002 second projection operator set....46
Figure 31: RMS flux shape error, 2 second transient, normal beta values, 0.002 second projection operator set....47
Figure 32: RMS flux shape error, 2 second transient, 0.0001 beta values, 0.002 second projection operator set....47
Figure 33: RMS flux shape error, 2 second transient, 0.00001 beta values, 0.002 second projection operator set....48
Figure 34: RMS flux shape error, 2 second transient, 0.0001 beta values, 0.01 second projection operator set....49
Figure 35: RMS flux shape error, 120 second transient, normal beta values, 0.002 second projection operator set....50
Figure 36: RMS flux shape error, 120 second transient, 0.0001 beta values, 0.002 second projection operator set....50
Figure 37: RMS flux shape error, 120 second transient, 0.0001 beta values, 0.01 second projection operator set....51
Figure 38: RMS flux shape error, 120 second transient, 0.0001 beta values, 2 second projection operator set....51
Figure 39: Hot-spot flux shape error, step insertion transient, normal beta values. ...52
Figure 40: Hot-spot flux shape error, step insertion transient, normal beta values, 1.1 x neutron velocity....53
Figure 41: Hot-spot flux shape error, step insertion transient, normal beta values , 0.9 x neutron velocity....54
Figure 42: RMS flux shape error, 2 second transient, 0.0001 beta values, 0.05 second projection operator set....56
Figure 43: RMS flux shape error, 120 second transient, 0.0001 beta values, 0.05 second projection operator set....56
Figure 44: RMS flux shape error, 2 second transient, normal beta values, 0.05 second projection operator set....57
Figure 45: RMS flux shape error, 120 second transient, normal beta values, 0.05 second projection operator set....57
Figure 46: RMS flux shape error, 120 second transient, normal beta values, 2 second projection operator set....58
Figure 47: Maximum flux error, 2 second transient, normal beta values, 0.05 second projection operator set....59
Figure 48: Hot-spot flux error, 2 second transient, normal beta values, 0.05 second projection operator set....60
Figure 49: Maximum flux error, 120 second transient, normal beta values, 0.002 second projection operator set....60
Figure 50: Maximum flux error, 120 second transient, normal beta values, 0.05 second projection operator set....61

Figure 51: Hot-spot flux error, 120 second transient, normal beta values, 0.002 second projection operator set.....61
Figure 52: Hot-spot flux error, 120 second transient, normal beta values, 0.05 second projection operator set.....62
Figure 53: Maximum flux error, 2 second transient, normal beta values, high frequency 0.05 second projection operator set.....64
Figure 54: Hot-spot flux error, 2 second transient, normal beta values, high frequency 0.05 second projection operator set.....64
Figure 55: Maximum flux error, 120 second transient, normal beta values, high frequency 0.05 second projection operator set.....65
Figure 56: Hot-spot flux error, 120 second transient, normal beta values, high frequency 0.05 second projection operator set.....65
Figure 57: RMS flux error, 2 second transient, 0.002 second projection operator set, update at 1 second, original restart parameters: (0.001 second time-steps). 66
Figure 58: RMS flux error, 2 second transient, 0.05 second projection operator set, update at 1 second, original restart parameters: (0.001 second time-steps). 67
Figure 59: RMS flux error, 120 second transient, 0.002 second projection operator set, update at 60 seconds, original restart parameters: (0.01 second time-steps).....67
Figure 60: RMS flux error, 120 second transient, 0.05 second projection operator set, update at 60 seconds, original restart parameters: (0.01 second time-steps).....68
Figure 61: RMS flux error, 2 second transient, update at 1 second, 0.01 time-step for annealing and operator production.....69
Figure 62: RMS flux error, 120 second transient, update at 60 seconds, 0.05 second annealing time-step.....69
Figure 63: RMS flux error, 2 second transient, update at 1 second, 0.001 second operator production time-step.....71
Figure 64: RMS flux error, 2 second transient, update at 1 second, 0.002 second operator production time-step.....71
Figure 65: RMS flux error, 2 second transient, update at 1 second, doubled projection operator frequency. 72
Figure 66: Maximum flux error, 2 second transient, update at 1 second, original projection operator frequency. 73
Figure 67: Maximum flux error, 2 second transient, update at 1 second, doubled projection operator frequency. 73
Figure 68: Maximum flux error, 120 second transient, update at 1 second, original projection operator frequency. 74
Figure 69: Maximum flux error, 120 second transient, update at 1 second, doubled projection operator frequency. 74
Figure 70: Flux shape, 2 second transient, rods ½ inserted.....76
Figure 71: Normalized flux shape error, 2 second transient, 0.002 lo-fi, rods 4/5 inserted.....77

Figure 72: Normalized flux shape error, 2 second transient, 0.05 lo-fi, rods 4/5 inserted. 78
Figure 73: Normalized flux shape error, 120 second transient, 0.002 lo-fi, rods 4/5 inserted. 79
Figure 74: Normalized flux shape error, 120 second transient, 0.05 lo-fi, rods 4/5 inserted. 80
Figure 75: Normalized precursor delta, 2 second transient, rods 4/5 inserted. 81
Figure 76: Normalized precursor delta, 120 second transient, rods 4/5 inserted. 82
Figure 77: Normalized delayed neutron shape delta, 2 second transient, rods 4/5 inserted. 83
Figure 78: Normalized delayed neutron shape delta, 120 second transient, rods 4/5 inserted. 84
Figure 79: Power oscillations following step rod and boron decreases, 0.01 second time-step, 1817.30ppm final boron. 87
Figure 80: Power oscillations following step rod and boron decreases, 0.01 second time-step, 1817.40ppm final boron. 87
Figure 81: Power oscillations following step rod and boron decreases, 0.01 second time-step, 1817.40ppm final boron, doubled velocity. 88
Figure 82: Power oscillations following step rod and boron decreases, 0.1 second time-step, 1817.40ppm final boron. 88
Figure 83: Power oscillations following step rod and boron decreases, 0.1 second time-step, 1817.40ppm final boron, doubled velocity. 89
Figure 84: Power oscillations following step rod and boron decreases, 0.01 second time-step, 1817.445ppm final boron, normal vs. suppressed betas, 1817.43ppm fixed boron. 89
Figure 85: Power oscillations following step rod and boron decreases, 0.01 second time-step, 1817.445ppm final boron, 0.1 second ramp reactivity change. 90
Figure 86: Steady state radial flux shape at various axial heights in the core with bank 9 control rods fully inserted. 91
Figure 87: Normalized difference in radial flux shape at various axial heights at 0.02 seconds versus 1 seconds. 92
Figure 88: Normalized difference in radial flux shape at various axial heights at 0.02 seconds versus 1000 seconds. 93
Figure 89: Normalized difference in radial flux shape, including non-fueled regions, at various axial heights at 0.02 seconds versus 1000 seconds. 94
Figure 90: Normalized difference in radial delayed neutron production distribution, at various axial heights at 0.02 seconds versus 1 second. 95
Figure 91: Normalized difference in radial delayed neutron production distribution, at various axial heights at 0.02 seconds versus 1000 seconds. 96
Figure 92: 2 second rod withdrawal transient maximum flux error, 0.05 second projection operator set. 106

Figure 93: 2 second rod withdrawal transient RMS flux error, 0.05 second projection operator set. 106
Figure 94: 2 second rod withdrawal transient maximum precursor error, 0.05 second projection operator set. 107
Figure 95: 2 second rod withdrawal transient RMS precursor error, 0.05 second projection operator set. 107
Figure 96: Maximum DNP error, 2 second transient, normal beta values, high frequency 0.05 second projection operator set. 108
Figure 97: RMS precursor error, 2 second transient, normal beta values, high frequency 0.05 second projection operator set. 108
Figure 98: Maximum DNP error, 120 second transient, normal beta values, high frequency 0.05 second projection operator set. 109
Figure 99: RMS precursor error, 120 second transient, normal beta values, high frequency 0.05 second projection operator set. 109
Figure 100: Normalized flux shape error, 2 second transient, 0.05 lo-fi, rods 1/5 inserted. 110
Figure 101: Normalized flux shape error, 2 second transient, 0.05 lo-fi, rods ½ inserted. 110
Figure 102: Normalized flux shape error, 2 second transient, 0.05 lo-fi, rods fully inserted. 111
Figure 103: Normalized flux shape error, 120 second transient, 0.05 lo-fi, rods 1/5 inserted. 111
Figure 104: Normalized flux shape error, 120 second transient, 0.05 lo-fi, rods ½ inserted. 112
Figure 105: Normalized flux shape error, 120 second transient, 0.05 lo-fi, rods fully inserted. 112
Figure 106: Normalized delayed neutron shape delta, 2 second transient, rods 1/5 inserted. 113
Figure 107: Normalized delayed neutron shape delta, 2 second transient, rods ½ inserted. 113
Figure 108: Normalized delayed neutron shape delta, 2 second transient, rods fully inserted. 114
Figure 109: Normalized delayed neutron shape delta, 120 second transient, rods 1/5 inserted. 114
Figure 110: Normalized delayed neutron shape delta, 120 second transient, rods ½ inserted. 115
Figure 111: Normalized delayed neutron shape delta, 120 second transient, rods fully inserted. 115
Figure 112: Normalized difference in radial flux shape, including non-fueled regions, at various axial heights at 500 seconds versus 1000 seconds.. 116
Figure 113: Normalized difference in radial delayed neutron production distribution, at various axial heights at 0.02 seconds versus 1000 seconds. 116

1. Introduction

Designing the core of a nuclear power reactor is an intricate process. There are many requirements that the reactor core must meet, including safety limits for all probable transients. In order to ensure that the reactor can be operated safely, it is important to be able to predict the behavior of the core. Mathematical models are employed to assist in this process as the mechanisms which affect reactor behavior are challengingly complex. While the solution to some mathematical models of reactor behavior can be approximated, and a very few solved using analytical methods, real reactor behavior is best predicted by computer codes that use numerical methods to solve the mathematical models. Due to the significant variance in relevant timescales, physical dimension, and other properties involved in modeling the behavior of a reactor, the computational cost can be quite high, depending on the desired accuracy and complexity of the model. There are numerous available techniques to reduce the computational burden of reactor modeling, however, there is still opportunity to do more.

1.1 Overview

In an effort to enhance simulation capabilities while at the same time minimizing computational burden, multi-fidelity approaches have been proposed. Often these approaches are used in studies of risk analysis, and consist of many low-fidelity simulations which pinpoint scenarios which require higher accuracy and thus impose a greater computation cost. Another approach sometimes used is an adaptive mesh refinement (AMR) technique, which is used to vary the resolution of numerical schemes used within a simulation model. For most advanced simulations the associated variables will be discretized to allow for solution of complicated equations and relationships. The discretized spatial distribution takes the form of a grid or 'mesh'; varying the grid spacing and thus the number of discrete regions will accordingly affect the computational accuracy and speed. The approach being investigated here, called Adaptive Model Refinement (AMoR), is for any given transient simulation, with the

intention of combining a low-fidelity and a higher-fidelity model in such a way as to take advantage of the benefits of each. This is done by running the low-fidelity simulation until an error criteria is reached and improved accuracy is needed, at which point the simulation switches to high-fidelity simulation, hopefully reducing the error and subsequently returning to the low-fidelity simulation. For the purpose of the analysis here, various direct comparisons of the high-fidelity and low-fidelity solutions are used. They are described in Chapter 2. Ideally, the high-fidelity solution would not need to fully compute, as that would make the method redundant. For this purpose, the eventual goal of the AMoR approach is to use an adjoint based method to perform uncertainty quantification for the error prediction.

1.2 Theoretical basis

Most neutron behavior modeling solutions and codes are based on the neutron transport equation. [4]

$$\begin{aligned}\frac{1}{v(E)}\frac{\partial}{\partial t}\psi(\vec{r},E,\hat{\Omega},t) + \hat{\Omega}\cdot\nabla\psi(\vec{r},E,\hat{\Omega},t) + \Sigma_t(\vec{r},E,t)\psi(\vec{r},E,\hat{\Omega},t) \\ = \int_{4\pi} d\hat{\Omega}' \int_0^\infty dE'\, \Sigma_s(\vec{r},E'\to E,\hat{\Omega}'\cdot\hat{\Omega},t)\psi(\vec{r},E',\hat{\Omega}',t) \\ + \frac{\chi(\vec{r},\mathrm{E},t)}{4\pi}\int_{4\pi} d\hat{\Omega}' \int_0^\infty dE'\, \nu_f(\vec{r},E',t)\Sigma_f(\vec{r},E',t)\psi(\vec{r},E',\hat{\Omega}',t) \\ + Q(\vec{r},E,\hat{\Omega},t)\end{aligned} \tag{1.1}$$

The equation represents changes in neutron concentration, energy, and travel over space and time. Excepting the first term, which is just the time rate of change of neutron flux, each term represents an effect that may occur during the lifetime of a neutron. The angular neutron flux, $\psi(\vec{r},E,\hat{\Omega},t)$, is dependent on position, neutron energy, travel direction, and time. Material properties such as the total cross-section, Σ_t, may vary over space and time as well as with regard to the energy of the interacting neutron. These properties describe the result and probabilities of neutron-material

interactions. The external neutron source term, $Q(\vec{r}, E, \hat{\Omega}, t)$, may also vary with position, neutron energy, travel direction, and time.

The delayed fission neutron source term is not explicitly included in the form of the equation shown here. The neutron transport equation is based on the Boltzmann equation and, while it unambiguously represents the behavior of neutrons in time and space, it is extremely difficult to solve for all but the simplest theoretical situations. There are many different approaches to applying the neutron transport equation; one of the most common is to derive and use approximations of it that are sufficiently accurate for practical applications. A commonly used approximation is the multi-group diffusion equation, a principle tool for modeling nuclear reactors. [4]

$$\begin{aligned}\frac{1}{v(E)}\frac{\partial}{\partial t}\phi(\vec{r},E,t) - \nabla\cdot D(\vec{r},E,t)\nabla\phi(\vec{r},E,t) + \Sigma_t(\vec{r},E,t)\phi(\vec{r},E,t) \\ = \int_0^\infty dE'\,\Sigma_s(\vec{r},E'\to E,t)\phi(\vec{r},E,t) \\ + \chi(\vec{r},E,t)\int_0^\infty dE'\,\nu_f(\vec{r},E',t)\Sigma_f(\vec{r},\mathrm{E}',t)\psi(\vec{r},E',t) + Q(\vec{r},E,t)\end{aligned} \tag{1.2}$$

The diffusion equation can be derived directly from the transport equation, with specific assumptions and approximations. The first step is to remove the angular dependence by introducing the approximation that the angular flux is only weakly dependent on angle, permitting it to be represented by first order spherical harmonic representations. This allows the introduction of Fick's Law, and the use of the diffusion coefficient to approximate the relationship of neutron current and flux. Scattering is assumed to be, at most, linearly anisotropic. Fission and the external source are assumed to be isotropic. The diffusion equation can also be developed empirically, starting with Fick's law for diffusion of neutrons and then introducing terms to account for neutron production and loss in every location [5]. The more rigorous method is, of course, the derivation from the transport equation.

1.3 NESTLE

The high-fidelity code employed here was NESTLE, standing for Nodal Eigenvalue, Steady-state, Transient, Le core Evaluator. NESTLE is a few-group neutron diffusion equation solver utilizing the nodal expansion method. The code was primarily written in FORTRAN 77; code used in this project also employs subroutines written in FORTRAN 90. NESTLE's capabilities include solving the eigenvalue (criticality), eigenvalue adjoint, external fixed-source steady-state, or external fixed-source or eigenvalue initiated transient problems. The code supports utilization of two or four neutron energy groups, though only two groups were employed in this endeavor. It is capable of modeling Cartesian and Hexagonal geometries and three, two, or one spatial dimensions. While the code has thermal-hydraulic feedback capability, it was turned off for the purpose of simplifying the investigations conducted here. NESTLE has many additional features not used in this study [2]. One of NESTLE's features that is utilized is the restart capability. NESTLE can resume a transient simulation after being stopped using saved data from the end of the previous run.

All non-restart transient runs begin with a steady-state initialization, wherein NESTLE numerically solves the multi-group steady-state diffusion equation in eigenvalue form, shown here with spatial dependency suppressed.

$$-\nabla \cdot D_g \nabla \phi_g + \Sigma_{tg} \phi_g = \sum_{g'=1}^{G} \Sigma_{sgg'}\, \phi_{g'} + \frac{\chi_g}{k} \sum_{g'=1}^{G} \nu_{g'}\, \Sigma_{fg'} \phi_{g'} \tag{1.3}$$

Spatial discretization is achieved using the finite difference method. Nodal Expansion Method (NEM) is used to modify the diffusion coupling coefficients in order to correct the errors introduced by the finite difference method and material homogenization. Transient runs are treated similarly, with the addition of time and delayed neutrons as shown in Eq. (1.4) and (1.5), with time and spatial dependencies depressed.

$$\frac{1}{v_g}\frac{\partial \phi_g}{\partial t} = \nabla \cdot D_g \nabla \phi_g - \Sigma_{tg} \phi_g + \sum_{g'=1}^{G} \Sigma_{sgg'}\, \phi_{g'} + (1-\beta)\chi_g^{(P)} \sum_{g'=1}^{G} \nu_{g'}\, \Sigma_{fg'} \phi_{g'} + \sum_{i=1}^{I^{(D)}} \chi_{gi}^{(D)}\, \lambda_i C_i + Q_{ext_g} \tag{1.4}$$

and

$$\frac{\partial C_i}{\partial t} = \beta_i \sum_{g=1}^{G} \nu_g \Sigma_{fg} \phi_{g'} - \lambda_i C_i \; for \; i = 1, \dots, I^{(D)} \tag{1.5}$$

C_i is the concentration of delayed neutron precursor (DNP) group i, λ_i is the DNP group decay constant, and β_i is the fraction of all fission neutrons emitted per fission in a DNP group while β is the fraction of all fission neutrons that are born delayed, or the sum of β_i.

1.4 Point Kinetics and Quasi-static Method

A further simplification of the diffusion equation, the point reactor kinetics model assumes that the spatial flux shape does not change with time. Assuming one neutron energy group, the flux and precursor distributions can be factorized, or treated as having independent amplitude and spatial dependence:

$$\begin{aligned} \phi(\vec{r}, t) &= vn(t)\psi(\vec{r}) \\ C_i(\vec{r}, t) &= C_i(t)\psi(\vec{r}) \end{aligned} \tag{1.6}$$

Substituting these expressions into the one-group diffusion equation along with an expression for the prompt neutron lifetime l provides the point reactor kinetics equations (PKE) shown here with six delayed neutron precursor groups:

$$\begin{aligned} \frac{dn(t)}{dt} &= \frac{k(1-\beta)-1}{l} n(t) + \sum_{i=1}^{6} \lambda_i C_i(t) \\ \frac{\partial C_i(t)}{\partial t} &= \beta_i \frac{k}{l} n(t) - \lambda_i C_i \; for \; i = 1, \dots, 6 \end{aligned} \tag{1.7}$$

Most often, reactivity is used in place of the multiplication factor,

$$\rho \equiv \frac{k-1}{k}. \tag{1.8}$$

This model is typically used to simulate average behavior of a reactor during a transient [4]. Even though the assumption of non-variant flux shape may be incorrect,

the core average values determined by the point kinetics model can be quite accurate, due in part to improvements from the quasi-static approach.

The quasi-static approach of reactor kinetics was introduced in 1958 by Allan Henry as a modification of the original point kinetics method. He proposed that, rather than treating the spatial dependence or 'shape' of neutron flux as constant, it would instead change gradually with time.

$$\phi(\vec{r},t) = vn(t)\psi(\vec{r},t) \tag{1.9}$$

The purpose of the quasi-static method was to improve the point kinetics parameters (k,l), which do vary with flux shape and thus time [3]. The method assumes that the timescale over which flux shape changes and perceptibly affects the point kinetic parameters (PKP) is relatively long, thus it permits recalculating them at longer time intervals than the amplitude time-step intervals. Two main techniques were developed for improving the PKP, called the 'Improved Quasi-static Method' (IQM), and the 'Predictor-Corrector Quasi-static Method' (PCQM) [3].

1.5 PKE-solver

A point kinetics equation solver is used as the basis of the low-fidelity method. It solves equation (1.7) for core average neutron density using reactivity and other point kinetic parameters calculated beforehand using a point kinetics parameters routine that was added to NESTLE. The defining equations for the PKP have been derived using a variational technique. Using forward and adjoint steady state flux calculated by NESTLE, a perturbation in reactivity is calculated as

$$\Delta\rho \cong -\frac{\langle \phi^{\dagger}, \delta\Sigma_a \phi \rangle}{\langle \phi^{\dagger}, \mathrm{F}\phi \rangle}, \tag{1.10}$$

where $\phi^{\dagger}$ is the adjoint flux, $\delta\Sigma_a$ is the source of the perturbation, $\mathrm{F}\phi$ represents the fission source term, and the forward flux is ϕ. Note that the unperturbed flux is used rather than the perturbed flux based on the assumption that the perturbation in the flux is relatively small [4]. The details of the method used are further described in the

RAMBO User's Manual [6]. It is significant to note that the parameters calculated in this method differ from straight volume-averaged values as they are adjoint-weighted. The point kinetic parameters are calculated at multiple representative 'times', or rod heights, to capture the effect of changing flux shape on the parameters. They only have to be recalculated if changes are made to basic core data or a different source of reactivity change were to be modeled.

1.6 Adaptive Model Refinement

The low-fidelity model for AMoR uses the improved point kinetics results and includes a separate prediction of the flux shape over time to produce a three dimensional solution that can be directly compared to a full high-fidelity solution. AMoR takes the average neutron density produced by PKE and projects it to three dimensions via multiplication by projection operators which, in combination, relate the mono-energetic core average neutron density to energy group and spatially dependent flux. The original AMoR method used additional projection operators to predict the delayed neutron precursor distribution. This has since been replaced by direct calculation of precursors from the low-fidelity flux for more accuracy with little added computational burden. The specifics of the method will be discussed in greater detail in Chapter 2. Primary development of the AMoR method and initial testing were performed by Sterling Satterfield as part of his Master's thesis [1]. In the current work completion of some aspects and supplementary testing was undertaken in order to assure the success and flexibility of the method. Further, additional transient modeling capability was added and tested as well.

2. Methodology

The reactor core being simulated for this research was a quarter core slice of a Westinghouse 4-loop, 3,311 MWt, PWR. The geometric and material inputs, as well as the cross-section data were from a sample data set representing Cycle 13 of McGuire Nuclear Station, Unit 1. It was modeled using two neutron energy groups and six delayed neutron precursor groups. Xenon and Samarium were suppressed and thermal-hydraulic feedback was turned off in order to reduce simulation complexity and allow clearer results.

2.1 Projection Operator Production

In order to produce a three-dimensional model using the PKE-solver, a prediction of the flux shape and energy distribution is needed. The factors used to transform the mono-energetic, average neutron density into a three-dimensional, two-group flux are called projection operators. The projection operators are generated by NESTLE prior to running the low-fidelity solution and can be produced in different manners, discussed further in Chapter 3. In all variations the method of calculating the projection operators is the same. Primary values NESTLE calculates include scalar flux,

$$\phi(\vec{r}, E, t) \rightarrow \phi_{g,m}(t), \tag{2.1}$$

precursor group concentration,

$$C_i(\vec{r}, t) \rightarrow C_{i,m}(t), \tag{2.2}$$

and neutron velocity,

$$v(\vec{r}, E, t) \rightarrow v_{g,m}(t), \tag{2.3}$$

where g is the index of neutron energy group, i is the precursor group, and m is the spatial node. The AMoR routines added to NESTLE allow calculation of various

projection operators from these primary values. Following are the equations used to calculate the projection operators, starting with the neutron density distribution,

$$n_{g,m}(t) = \frac{\phi_{g,m}(t)}{v_{g,m}(t)}, \tag{2.4}$$

from which the volume averaged neutron density is calculated,

$$\langle n(t) \rangle = \frac{\int_V dV \int_0^\infty dE\, n(\vec{r}, E, t)}{\int_V dV} = \frac{\sum_{m=1}^{M} \sum_{g=1}^{2} n_{g,m}(t)\, V_m}{\sum_{m=1}^{M} V_m}. \tag{2.5}$$

Two more intermediaries in developing the projection operators are the energy dependent volume averaged scalar flux,

$$\langle \phi_g(t) \rangle = \frac{\int_V dV \int_{E_{g-1}}^{E_g} dE\, \phi(\vec{r}, E, t)}{\int_V dV} = \frac{\sum_{m=1}^{M} \phi_{g,m}(t)\, V_m}{\sum_{m=1}^{M} V_m}, \tag{2.6}$$

and the volume averaged scalar flux,

$$\langle \phi(t) \rangle = \frac{\int_V dV \int_0^\infty dE\, \phi(\vec{r}, E, t)}{\int_V dV} = \frac{\sum_{m=1}^{M} \sum_{g=1}^{2} \phi_{g,m}(t)\, V_m}{\sum_{m=1}^{M} V_m}, \tag{2.7}$$

from which the flux energy partition function is calculated:

$$\langle f_g^{(\phi)}(t) \rangle = \frac{\langle \phi_g(t) \rangle}{\langle \phi(t) \rangle}. \tag{2.8}$$

The volume averaged neutron velocity is calculated as,

$$\langle v(t) \rangle = \frac{\langle \phi(t) \rangle}{\langle n(t) \rangle}. \tag{2.9}$$

The output of the PKE-solver is actually the factor by which the average neutron density changes with time, $\langle \bar{\tilde{n}}(t) \rangle$. This is equivalent to the average neutron density normalized to its initial value,

$$\langle \bar{n}(t) \rangle = \frac{\langle n(t) \rangle}{\langle n(0) \rangle}. \tag{2.10}$$

Initial volume averaged neutron density, $\langle n(0) \rangle$, is therefore a critical parameter for employing the projection operators. All volume averaged values are only averaged over the fueled nodes, rather than the entirety of the geometric core, as the PKE-Solver is only capable of approximating the region of the core containing fuel.

Once the energy dependence of the projection is set, the average-normalized spatial distribution, or shape-factors can be calculated. The scalar flux shape-factor is calculated as,

$$S_{g,m}^{(\phi)}(t) = \frac{\phi_{g,m}(t)}{\langle \phi_g(t) \rangle}. \tag{2.11}$$

Through these calculations the flux is factorized from a 3-D form into an amplitude-shape form, represented as,

$$\phi_{g,m}(t) = S_{g,m}^{(\phi)}(t) \, \langle f_g^{(\phi)}(t) \rangle \, \langle v(t) \rangle \langle \bar{n}(t) \rangle \langle n(0) \rangle \, . \tag{2.12}$$

In the original form of the AMoR method, the low-fidelity delayed neutron precursor concentration distribution was predicted using projection operators as well. The precursor related projection factors are still calculated, although they are no longer used for that purpose. Volume averaged precursor group concentration is calculated as,

$$\langle C_i(t) \rangle = \frac{\int_V \; C_i(\vec{r}, t) dV}{\int_V \; dV} = \frac{\sum_{m=1}^{M} C_{i,m}(t) \, V_m}{\sum_{m=1}^{M} V_m}, \tag{2.13}$$

from which the precursor group concentration shape-factor is calculated,

$$S_{i,m}^{(C)}(t) = \frac{C_{i,m}(t)}{\langle C_i(t) \rangle}. \tag{2.14}$$

2.2 Low-Fidelity Projection and Precursor prediction

The 3-D, energy dependent low-fidelity projected flux approximation is calculated as,

$$\tilde{\phi}_{g,m}(t) = S_{g,m}^{(\phi)}(t)\,\langle f_g^{(\phi)}(t)\rangle\,\langle v(t)\rangle\langle\bar{\tilde{n}}(t)\rangle\langle n(0)\rangle\,, \tag{2.15}$$

where the normalized volume averaged neutron density from the NESTLE projection-operator producing run is replaced by the approximate normalized volume averaged neutron density calculated by the PKE-solver. The projection operators are matched up to the appropriate low-fidelity neutron density corresponding to the concurrent rod position; for this reason all projection operator related files are indexed by rod position. When the current rod position of the low-fidelity simulation does not directly correspond to a set of files, the projection operator values are approximated using linear interpolation. This linear interpolation impacts the accuracy of the low-fidelity model; the specifics of this will be discussed in results section 3.3.4.

In the original method, a low-fidelity precursor concentration was calculated using an analogous projection,

$$\tilde{C}_{i,m}(t) = S_{i,m}^{(C)}(t)\,\langle\bar{\tilde{C}}_i(t)\rangle\,\langle C_i(0)\rangle\,. \tag{2.16}$$

In order to improve model accuracy, the projection method was replaced in the low-fidelity solution with a direct calculation of a delayed neutron precursor concentration from the low-fidelity projected flux. This set of equations is precisely the same as those used in the high-fidelity NESTLE diffusion model, however they are not significantly more computationally burdensome than the projection method, as they do not involve the solution of coupled algebraic equations. The precursor equation, Eq. (1.5), is solved utilizing the Integrating Factor method, giving,

$$C_i(t_n) = C_i(t_{n-1})e^{-\lambda_i \Delta t_n} + \beta_i \int_{t_{n-1}}^{t_n} \sum_{g=1}^{G} \nu_g\, \Sigma_{fg}\phi_g(t')\, e^{-\lambda_i(t_n - t')} dt', \tag{2.17}$$

where the current time-step's precursors depend on the previous precursor concentration and the fission rate over the last time step. Assuming a linearly varying

fission source between time-steps, this equation is approximated for numerical solution as,

$$C_i(t_n) = C_i(t_{n-1})e^{-\lambda_i \Delta t_n} + F_{i_n}^0 \sum_{g=1}^{G} \nu_g \, \Sigma_{fg} \phi_g(t_{n-1}) + F_{i_n}^1 \sum_{g=1}^{G} \nu_g \, \Sigma_{fg} \phi_g(t_n), \tag{2.18}$$

where

$$F_{i_n}^1 = \frac{\beta_i}{\lambda_i \Delta t_n} \left[\Delta t_n - \frac{1}{\lambda_i} \left(1 - e^{-\lambda_i \Delta t_n} \right) \right] \tag{2.19}$$

and

$$F_{i_n}^0 = -F_{i_n}^1 + \frac{\beta_i}{\lambda_i} \left[\left(1 - e^{-\lambda_i \Delta t_n} \right) \right]. \tag{2.20}$$

[2]. The relative accuracy of directly calculated and projected precursor concentrations is discussed in section 3.2. This calculation of the delayed neutron precursor concentration is not fed back in to the low-fidelity solution as the PKE-solver already has a similarly solved core-average delayed neutron precursor concentration it uses, which is calibrated to work with the adjoint-weighted PKP values.

2.3 Hereditary AMoR Setup

While NESTLE has a significant array of simulation capabilities, PKE-solver and AMoR are much more limited. At the beginning of this project segment the AMoR capabilities exclusively included modeling the flux and precursor concentrations during the insertion of a group of control rods. Within the scope of modeling a rod insertion transient, there were certain variables that could be easily adjusted. The time-frame of the rod-insertion, and some of the specifications of producing the projection operators, were the primary variables previously examined.

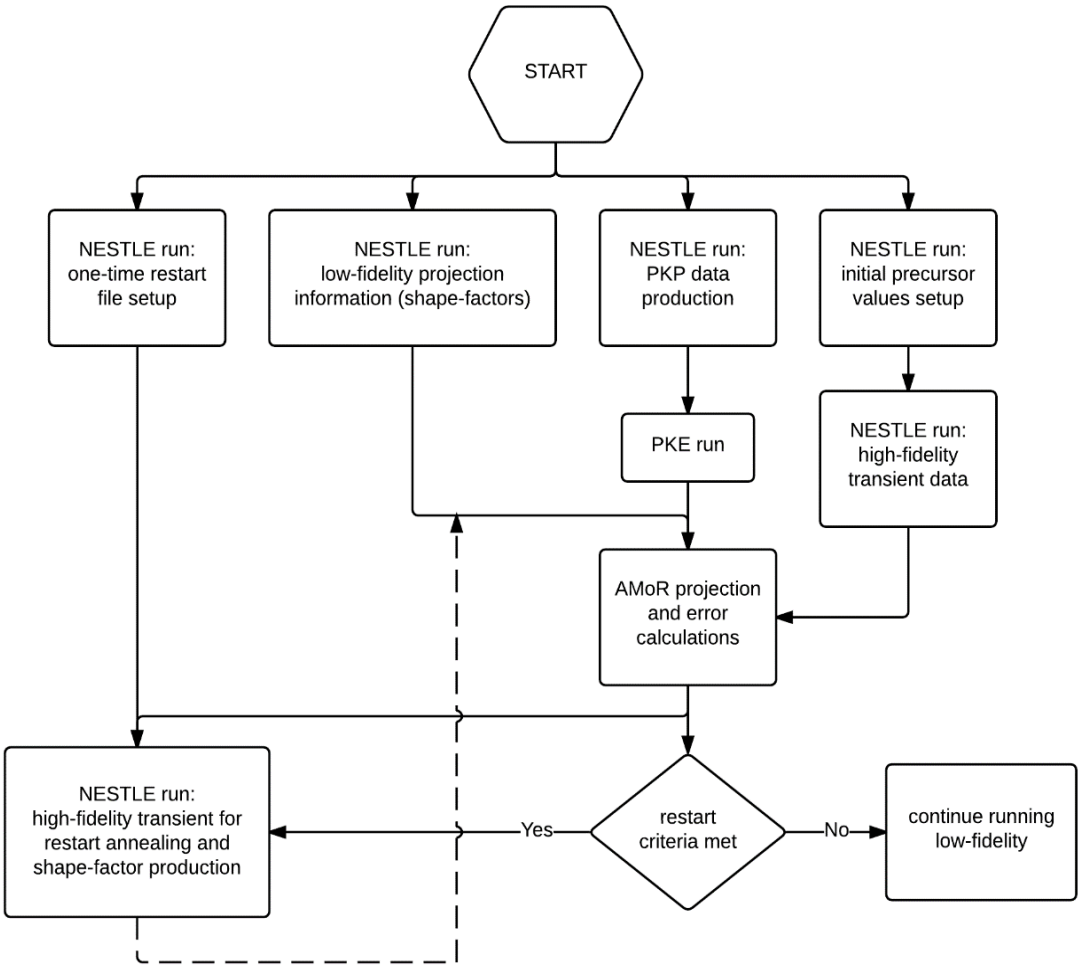

Figure 1: Required runs in NESTLE and PKE-solver to produce a full high-fidelity vs. low-fidelity comparison in the original and current AMoR setups.

In the original AMoR setup, all NESTLE and PKE-solver simulations were run separately. Figure 1 shows the runs required for initial setup of a new sample transient. Subsequent transients will reuse the saved data unless essential parameters are altered.

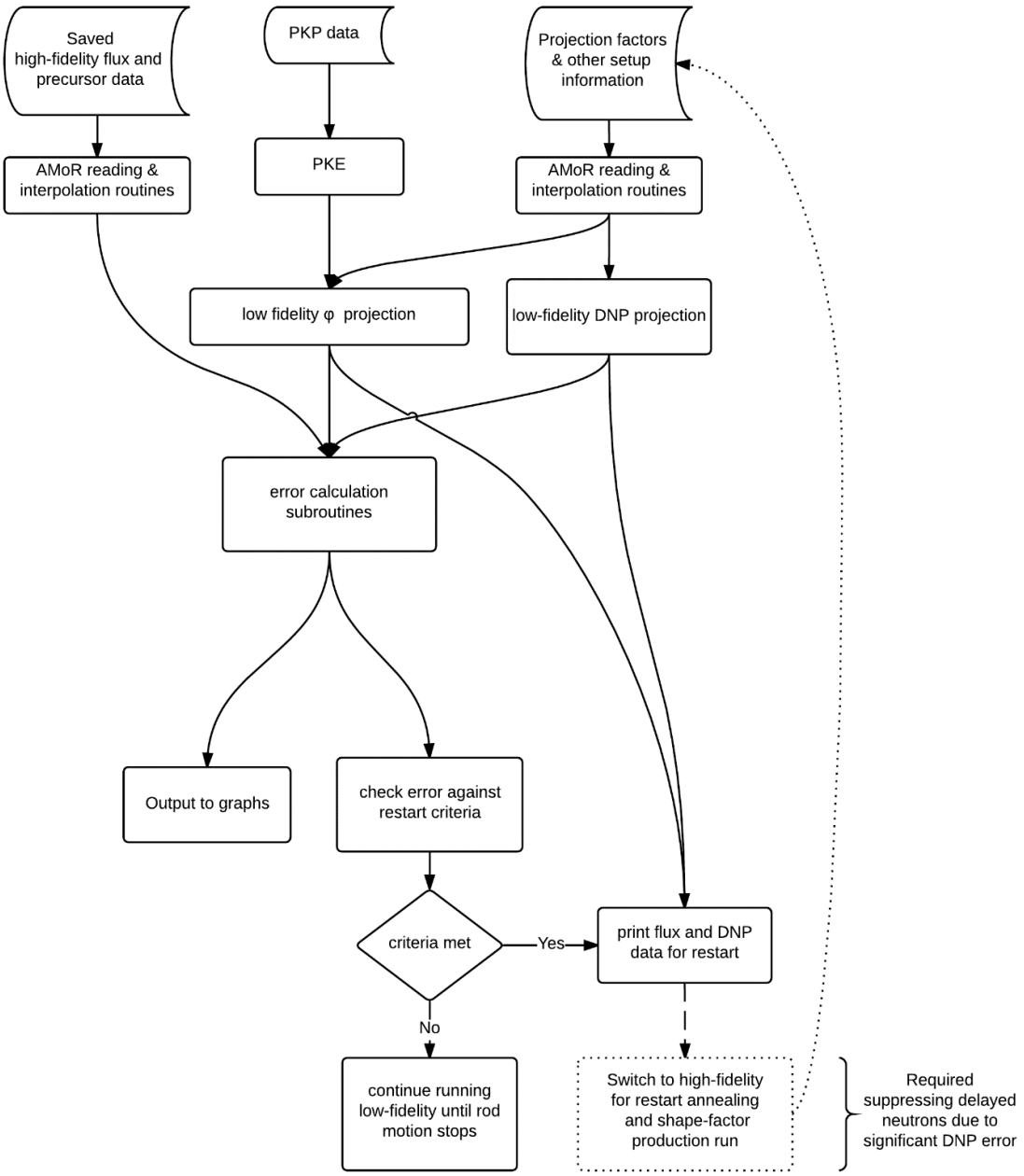

Figure 2: Original low-fidelity AMoR setup.

Following a NESTLE run, pertinent data which had been saved by AMoR routines during the transient could be transferred to and read in by the AMoR routines associated with producing the low-fidelity solution, as well as error computations, as illustrated in Figure 2.

One limitation of this code setup is that it requires saving information from the high-fidelity NESTLE solution to be used for comparison to the low-fidelity solution. Using saved data requires either recording information for every relevant time step, a significant amount of data, or interpolating between a set of saved points. Interpolating between saved points corresponding to rod position, as in the low-fidelity interpolation scheme, was selected to minimize the amount of data that had to be stored and transferred. While this scheme gives sufficient accuracy for most situations, it exhibits a minor flaw relating to subsequent DNP concentration calculations as discussed further in results section 3.2.2.

In the current system, the projection operators used in the low-fidelity solution must be produced by a NESTLE run and indexed by rod position. There are several choices available for NESTLE runs that will provide a reasonably accurate low-fidelity solution to a given rod insertion transient. One such option is to produce a library of steady state based projection operators corresponding to a pre-selected number of different rod positions. The accuracy and appropriateness of the steady state library was explored as part of Sterling Satterfield's work [1]. Another option is to use a rapid rod insertion to model the prompt neutron behavior during a longer rod insertion transient, as it is the shorter transient will have a commensurately shorter run-time. This method was initially explored as part of Satterfield's work [1], and the one selected for further evaluation here.

In the current setup, as well, the AMoR routines that save the projection operators are run parallel to those that save the flux and DNP concentration of the high-fidelity solution. This allows the corresponding shape-factor and energy dependence information to be available for direct comparison to the projection operators used in the low-fidelity solution.

2.4 Active Switching Concept & Methodology

Depending on preset error criteria, at some point during a given transient there will be a need to switch from the low-fidelity model to the high fidelity model in order to reduce the error. Once the error of the low-fidelity model grows too large, the flux and precursor information from preceding time steps are fed, along with rod position, back into the high-fidelity model. This is done by printing out the relevant low-fidelity data, pausing the low-fidelity run, and performing a high-fidelity NESTLE restart which uses the low-fidelity flux and precursor data as initial conditions with the expectation that the restarted high-fidelity run will "anneal" out the error. This is immediately followed by a simulation of a rapid transient which models the remainder of the rod motion transient, producing updated projection operators. The low-fidelity run is resumed and the new projection operators are used for the remainder of the low-fidelity run, or until the error again grows too large. The "annealing" process relies on the use of low-fidelity data from a prior time-step rather than the one which triggers the restart. The historical low-fidelity data are input into the NESTLE code as initial conditions from which a transient using small time increments is executed up to the current time-step, reducing the error each time the flux and precursor data are fed through the high-fidelity diffusion calculations. This is possible due to the constant relationship between production and loss terms. A mathematical argument for this is contained in Sterling Satterfield's work [1].

Initial verification of concept and method was performed by Sterling Satterfield and reported on in his thesis [1]. Results relevant to the current work are replicated in Chapter 3 of this document. The primary functionality of switching between high-fidelity and low-fidelity solutions had been completed as part of Sterling Satterfield's work. It was determined, however, that the delayed neutron precursor errors produced using the projection method, shown in section 3.2, were unacceptably large. This hindered the annealing process during the NESTLE restarts. In order to address this problem, and permit testing of the active switching method, the delayed neutrons were originally artificially suppressed by applying a constant 0.0001 β_i value across all delayed neutron precursor groups. As part of the project continuation and progression

the need for this makeshift fix was removed by changing the method by which the low-fidelity DNP concentration was determined. The projection method of DNP calculation, represented by Eq. (2.16) was replaced by direct calculation from low-fidelity flux as previously shown in Eqs. (2.18), (2.19), and (2.20). As will be discussed further in section 3.2, this significantly increased the accuracy of the low-fidelity DNP concentration prediction, thus permanently removing that hindrance to the active switching.

2.5 Hereditary Error Metrics

Many of the error analysis tools used in this report were developed by Sterling Satterfield [1] as part of the initial technique verification. Following is a brief summary of the error metrics utilized again here. Key error metrics of interest were ones that tended to demonstrate the largest magnitude of error, and those that most directly exhibited the success or failure of an attempted method modification. The error metric which consistently showed the largest error, which would trigger switching criteria, and excluding precursors calculated using the original projection method, was locally normalized flux error,

$$\varepsilon_{flux.local,g} = \frac{\phi_{g,m^*}(t) - \tilde{\phi}_{g,m^*}(t)}{\phi_{g,m^*}(t)}, \tag{2.21}$$

at the maximum flux error position:

$$m^* = \arg\max_{m} \frac{\left|\phi_{g,m}(t) - \tilde{\phi}_{g,m}(t)\right|}{\phi_{g,m}(t)}. \tag{2.22}$$

The largest flux errors in a transient are found near the rod tip as it moves through the core. As the largest relative flux error in the core is likely to not properly represent an overall picture of the core flux error or locations of particular interest such as hot spots, a better metric for that purpose is the average normalized flux error,

$$\varepsilon_{flux.avg,g} = \frac{\phi_{g,m^*}(t) - \tilde{\phi}_{g,m^*}(t)}{\langle \phi_g(t) \rangle}, \tag{2.23}$$

at the maximum flux position:

$$m^* = \arg\max_m \left|\phi_{g,m}(t)\right| . \tag{2.24}$$

The metrics for precursor concentration error are formulated in the same manner.

In several instances it was desired to examine the error of the shape-factors specifically, as these were determined to be the largest contributor to the overall error; this is discussed in Section 3.3. Recalling the formulation of the projected flux in section 2.2, removing the other projection operators allows calculation of locally or average normalized flux-shape errors,

$$\varepsilon_{flux\cdot shape.local,g} = \frac{S_{g,m^*}^{(\phi)}(t) - \tilde{S}_{g,m^*}^{(\phi)}(t)}{S_{g,m^*}^{(\phi)}(t)}, \tag{2.25}$$

$$\varepsilon_{flux\cdot shape.avg,g} = \frac{S_{g,m^*}^{(\phi)}(t) - \tilde{S}_{g,m^*}^{(\phi)}(t)}{\langle S_g^{(\phi)}(t)\rangle}, \tag{2.26}$$

at the maximum flux or maximum flux error positions as described in equations (2.22) and (2.24).

The best representation of the overall core-wide flux error is the volume weighted L-2 norm or RMS error of the flux,

$$\varepsilon_{2,flux.total} = \sqrt{\frac{\sum_{m=1}^{M}\left[\left(\phi_m(t) - \tilde{\phi}_m(t)\right)^2 \Delta z_m\right]}{M_{xy}Z}}\frac{1}{\langle\phi(t)\rangle}, \tag{2.27}$$

where

$$Z = \frac{1}{M_{xy}}\sum_{m=1}^{M}\Delta z_m , \tag{2.28}$$

and

$$M_{xy} = \frac{M}{M_z}. \tag{2.29}$$

Z, total height of the core, and Δz_m, height of the mth node, are used in place of core volume and node volumes as the nodes in a given XY-plane are uniform, though the

height of Z-planes varies. M_{xy} is the number of nodes in a single XY-plane, M_z is the number of Z-planes, and M is still the total number of nodes.

Normalized volume averaged neutron density,

$$\langle \bar{n}(t) \rangle = \frac{\langle n(t) \rangle}{\langle n(0) \rangle}, \tag{2.30}$$

and normalized volume averaged precursor group concentration,

$$\langle \bar{C}_i(t) \rangle = \frac{\langle C_i(t) \rangle}{\langle C_i(0) \rangle}, \tag{2.31}$$

were used as measures of method stability in specific instances.

2.6 Additional Error Metrics

In addition to the error metrics originally developed and used by Satterfield [1], two new error analysis techniques were introduced. The first was to look at the Root Mean Square (RMS) error in the flux shape, which was formulated as,

$$\varepsilon_{RMS,flux\cdot shape,g} = \sqrt{\frac{\sum_{m=1}^{M}\left[\left(S_{g,m}^{(\phi)}(t) - \tilde{S}_{g,m}^{(\phi)}(t)\right)^2 \Delta z_m\right]}{M_{xy}Z}}. \tag{2.32}$$

This metric was added to assist in evaluating the overall core-wide errors, as a representation of the shape-factor specific average error. In general, the RMS flux shape error and the local flux-shape errors behave similarly.

The second new error analysis technique is a 3-D graph for investigative visualization, produced in MATLAB. A short routine was written that can read in the NESTLE saved flux, flux shape, or precursor value information, and plot multiple horizontal slices of it. This allows direct visual inspection of the flux or precursor distribution, at a given time or rod height, from a given set of data. This routine was also used to visualize disparities between various sets of data by plotting the difference, or normalized difference, between any two sets of flux or precursor data.

The third additional error metric is intended to eventually be used to bypass the need to calculate a full high-fidelity solution. For this metric, the low-fidelity flux is employed in combination with generalized perturbation theory (GPT) adjoint flux to produce error responses which indicate the relative error in a given core location at a given point in time. The time and core location of interest are predefined using a response function, f. Starting with the high-fidelity flux, ϕ, with A being the high fidelity operator, and the low-fidelity flux, $\tilde{\phi}$, with $\tilde{A}$ being the low-fidelity operator, then

$$A\phi = 0, \qquad \tilde{A}\tilde{\phi} = 0, \qquad \& \quad \Delta\phi = \tilde{\phi} - \phi. \tag{2.33}$$

The residual is calculated as

$$r = A\tilde{\phi}. \tag{2.34}$$

The error response is defined as

$$R = \langle f, \Delta\phi \rangle. \tag{2.35}$$

The adjoint solution, Ψ^*, measures the importance of neutrons in regards to the response function [7]. When combined with the adjoint operator, A^*, it reproduces the response function.

$$A^*\Psi^* = f. \tag{2.36}$$

The adjoint operator is defined as

$$\langle \phi^*, A\phi \rangle = \langle A^*\phi^*, \phi \rangle. \tag{2.37}$$

The error response measured by eq. (2.35) can also be produced as

$$R = \langle \Psi^*, r \rangle, \tag{2.38}$$

since,

$$R = \langle \Psi^*, r \rangle = \langle \Psi^*, A\tilde{\phi} \rangle = \langle \Psi^*, A\left(\tilde{\phi} - \phi\right) \rangle = \langle A^*\Psi^*, \tilde{\phi} - \phi \rangle = \langle f, \Delta\phi \rangle. \tag{2.39}$$

The error response calculated using the adjoint method would hopefully permit measuring the relative error in the low-fidelity solution without requiring the high-fidelity forward solution for comparison. At this time the method is not fully implemented as it still requires solving the forward solution to obtain the adjoint solution. Figure 3 shows the current process for the error responses.

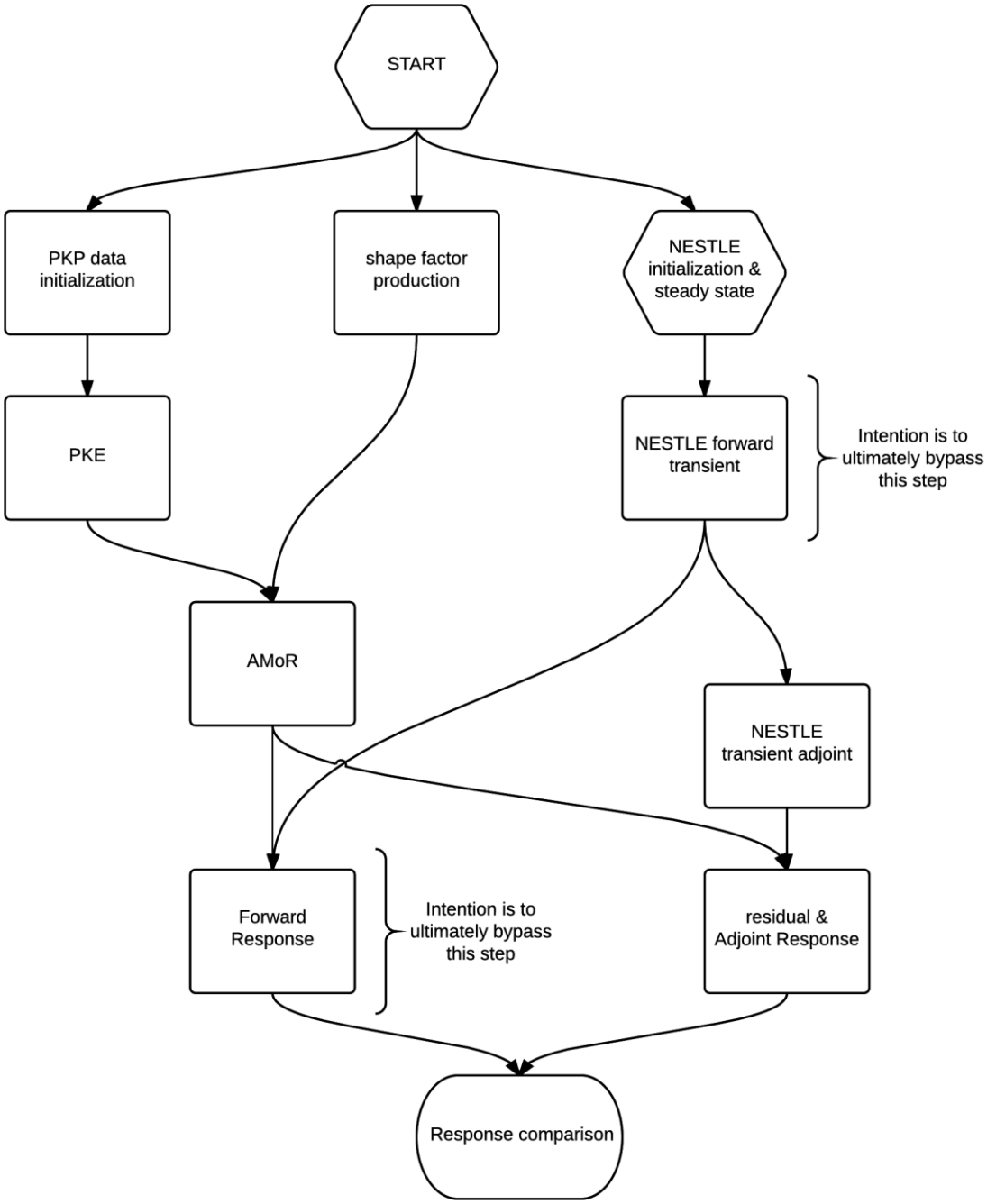

Figure 3: AMoR input to GPT responses.

3. Results

This project phase was focused on two main activities. The first was to finish the development and evaluation of the AMoR method and begin the process of combining all aspects of AMoR into one code. A copy of NESTLE was modified to have the PKE-Solver encoded within it prior to the initiation of this work. Further work to include production of the low-fidelity solution and error analysis was performed as part of this research, based on AMoR routines developed by Sterling Satterfield. In addition, the modeling capabilities of the PKE-Solver and AMoR were expanded. Satterfield demonstrated that the AMoR model was essentially functional [1]. Section 3.2 of this work describes tasks that were performed to complete the implementation of the low-fidelity model, and the added functionalities in more detail.

The second goal of this research was to find ways to improve the low-fidelity model by reducing the inherent error. This required identifying the specific sources which were contributing to the error. Section 3.3 covers the various efforts to find improvements.

3.1 Test Setup

The simulations were performed on a standard desktop computer running Windows 7 64-bit. The base codes used are NESTLE v5.2.1 [2] and a PKE-Solver. Both codes were modified prior to this project, and further modified in the course of this work, as described in section 3.2. The codes were compiled, debugged and executed with Microsoft Visual Studios 2012 using the Intel FORTRAN compiler.

The reactor core being simulated for this research was a Westinghouse 4-loop, 3,311 MWt, PWR. The geometric and material inputs, as well as the cross-section data were from a sample data set representing Cycle 13 of McGuire Nuclear Station, Unit 1. It was modeled using two neutron energy groups and six delayed neutron precursor groups. The simulation used quarter-core, Cartesian geometry with a cyclic radial interior boundary condition and zero flux boundary conditions on the radial exterior, Z-plane top, and Z-plane bottom. The core is discretized into 28 Z-planes with the XY-

planes being represented with 18x18 nodes. The approximately cylindrical core requires that not all nodes contain core material. The fueled region consists of the inner 26 Z-planes and a specific portion of the XY nodes. Xenon and Samarium were suppressed and thermal-hydraulic feedback was turned off. The simulation employed a constant coolant inlet temperature of 555.50°F and a constant coolant mass flow rate of 1,439,284.5 lb/(ft^{2}sec).

In the majority of the test cases the transients began at the ARO position and ended with a single rod bundle fully inserted over varying transient durations. For these transients a soluble boron level of 1899.83ppm was used. The two fundamental cases consisted of a fast rod insertion transient with a duration of 2 seconds and a slow rod insertion transient with a duration of 120 seconds. These transients were selected as they induce a substantial change in both the core average and radially integrated relative power (flux) distributions, implying a severe test for the AMoR method examples [1].

3.2 The Hybrid Low-Fidelity Model

In previous work by Satterfield [1], it was determined that if steady state projection operators were used, for a 2 second rod insertion the largest flux error was near 30%, as seen in Figure 4. The flux error at the maximum flux location reached approximately 10%, as shown by Figure 5. In all of the cases discussed here, the projected solution is being compared to a high-fidelity solution that is calculated by NESTLE, saved in 40 equidistant snapshots, and interpolated for intermediate values.

For the "active model switching" method the projection operators were generated at 20 equidistant points during a rapid insertion transient occurring over 0.002 seconds. Representative flux errors are shown in Figure 6 and Figure 7. While the original rapid-insertion projection operators yielded larger maximum errors, the steady state projection operators yielded larger flux errors at hot-spot locations, which is undesirable.

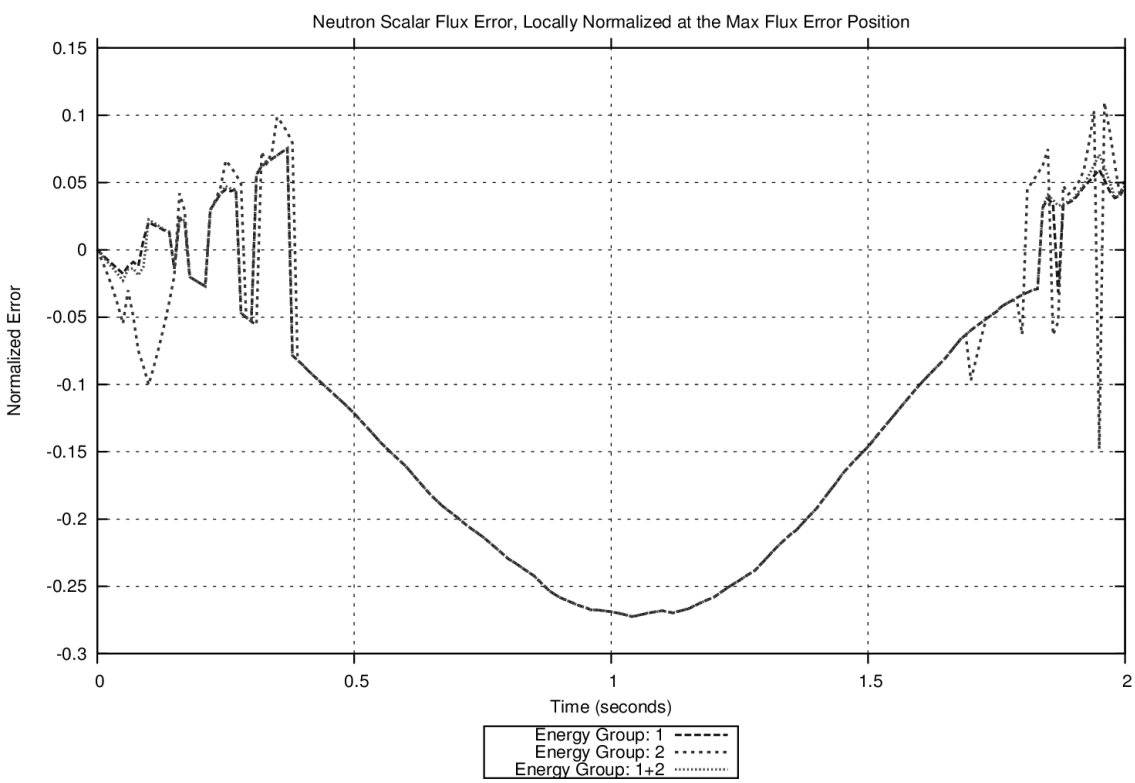

Figure 4: Maximum flux error for 25 steady-state projection operator sets.

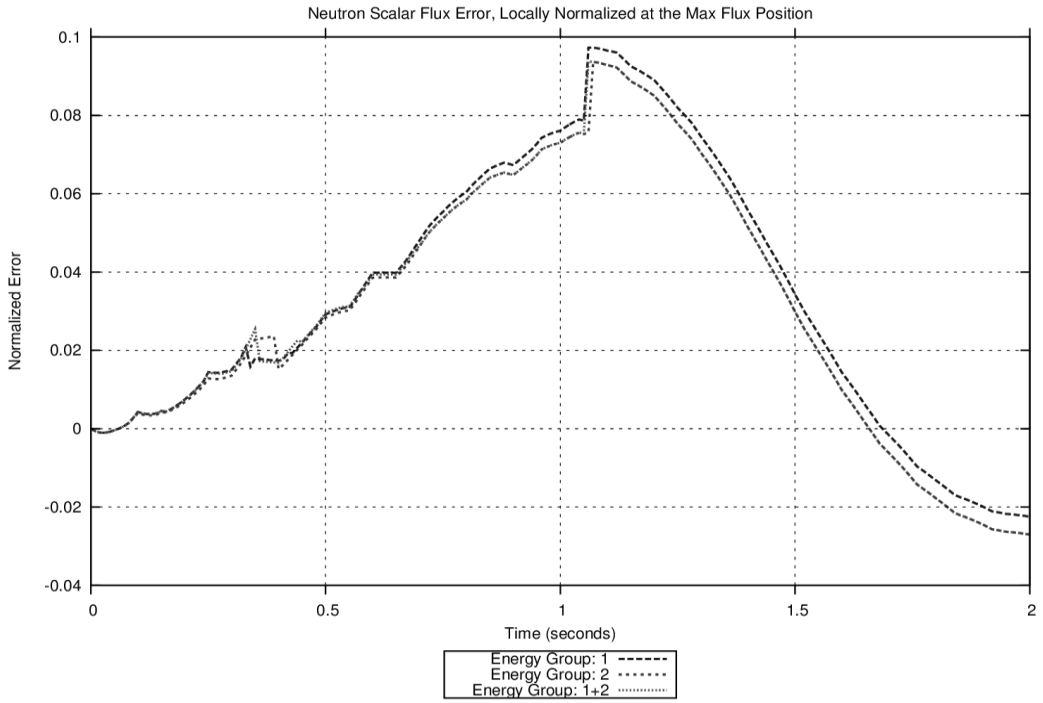

Figure 5: Hot-spot flux error for 25 steady-state projection operator sets.

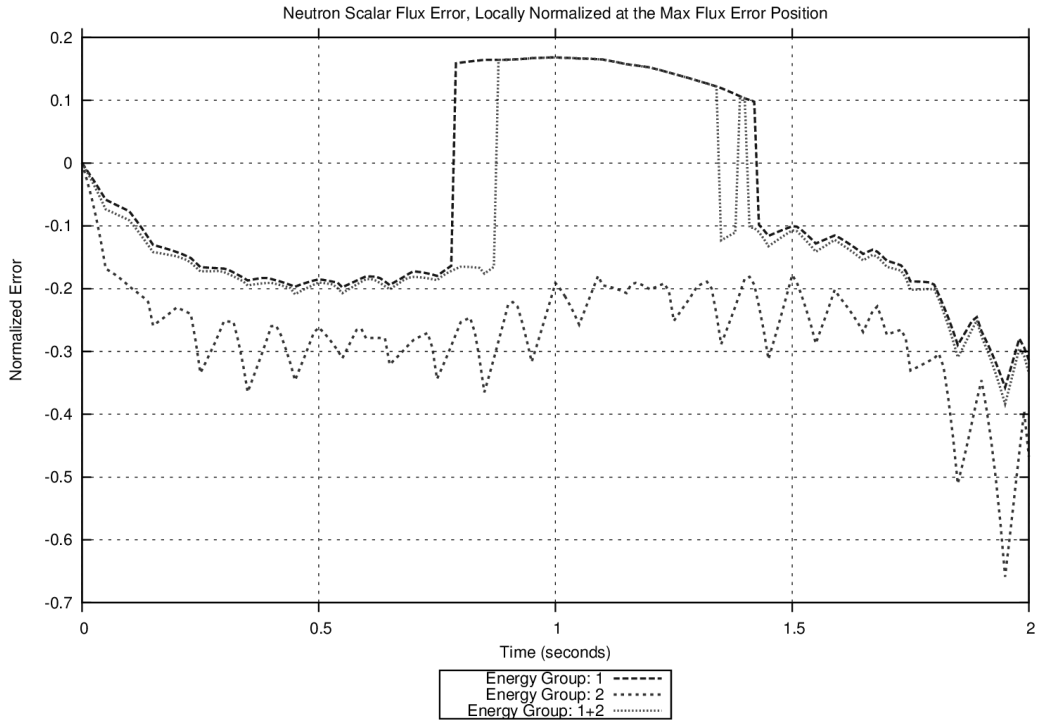

Figure 6: Maximum flux error for 0.002 second rapid-insertion projection operator sets.

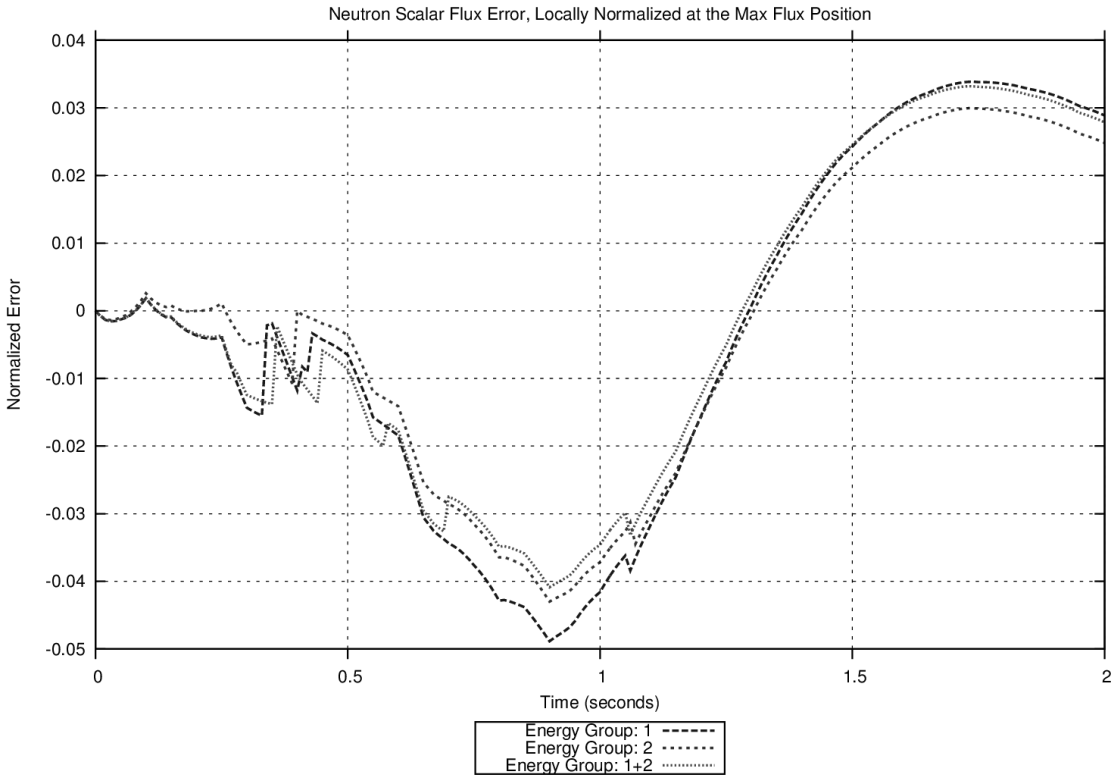

Figure 7: Hot-spot flux error for 0.002 second rapid-insertion projection operator sets.

3.2.1 Original Precursor Error

Both sets of projection operators yielded substantial local DNP concentration errors throughout the core with the original method of generating low-fidelity precursor values. For the steady-state projection operators, DNP concentration error reached nearly 70% at its maximum value, as seen in Figure 8. The RMS precursor error, representing core-wide average precursor error, reached over 30% and is shown in Figure 9. For the 0.002 second rapid-insertion projection operator set, DNP concentration error reached nearly 120% at its absolute maximum value, as seen in Figure 10. The RMS precursor error reached approximately 16%, as shown in Figure 11. The general relationship of the flux and precursor errors for the 120 second rod insertion are comparable to those discussed here for the 2 second rod insertion.

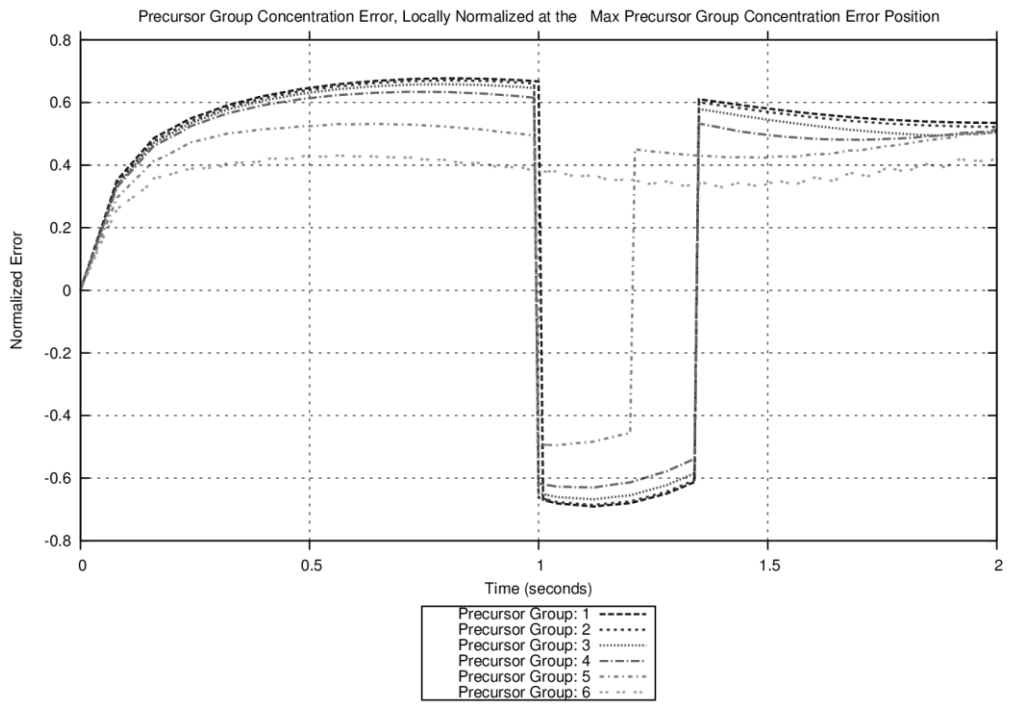

Figure 8: Maximum precursor error for 25 steady-state projection operator sets.

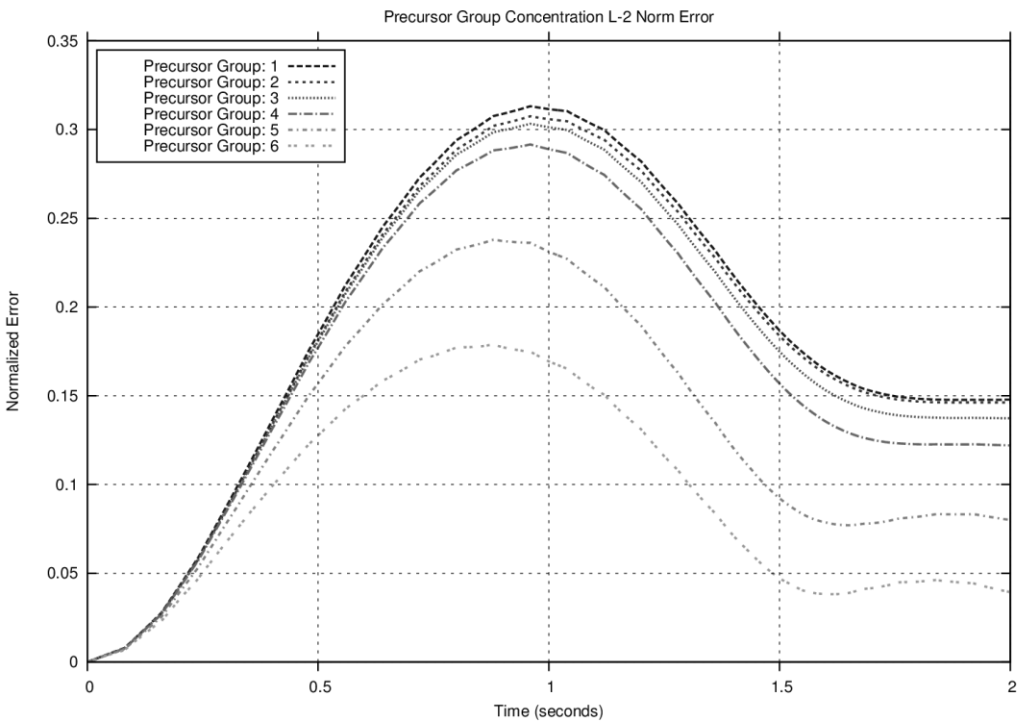

Figure 9: RMS precursor error for 25 steady-state projection operator sets.

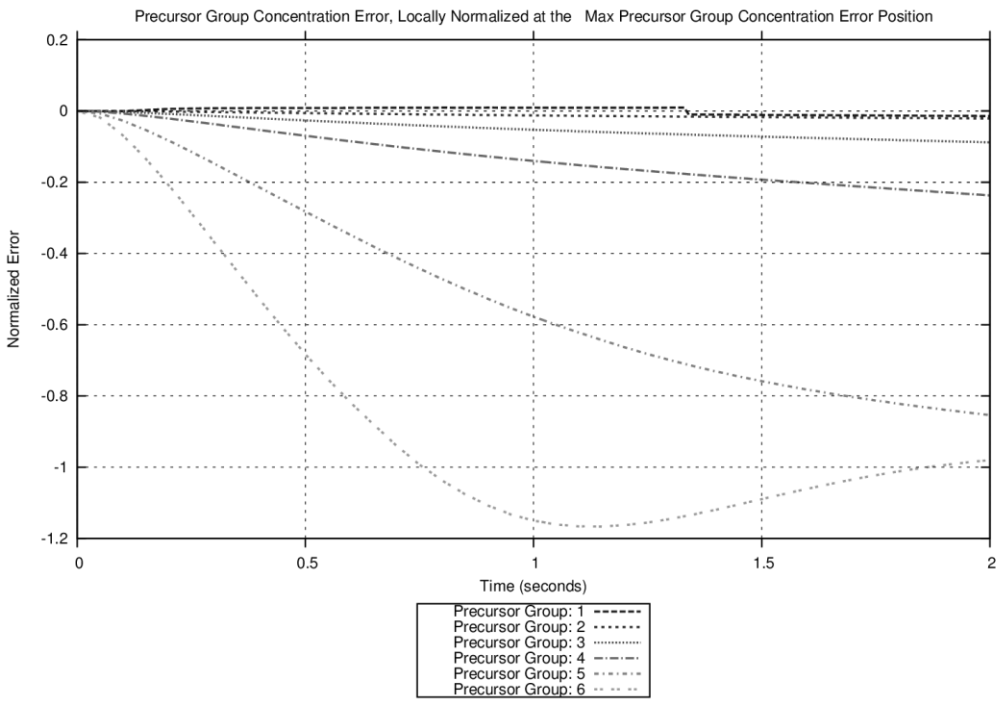

Figure 10: Maximum precursor error for 0.002 second rapid-insertion projection operator sets.

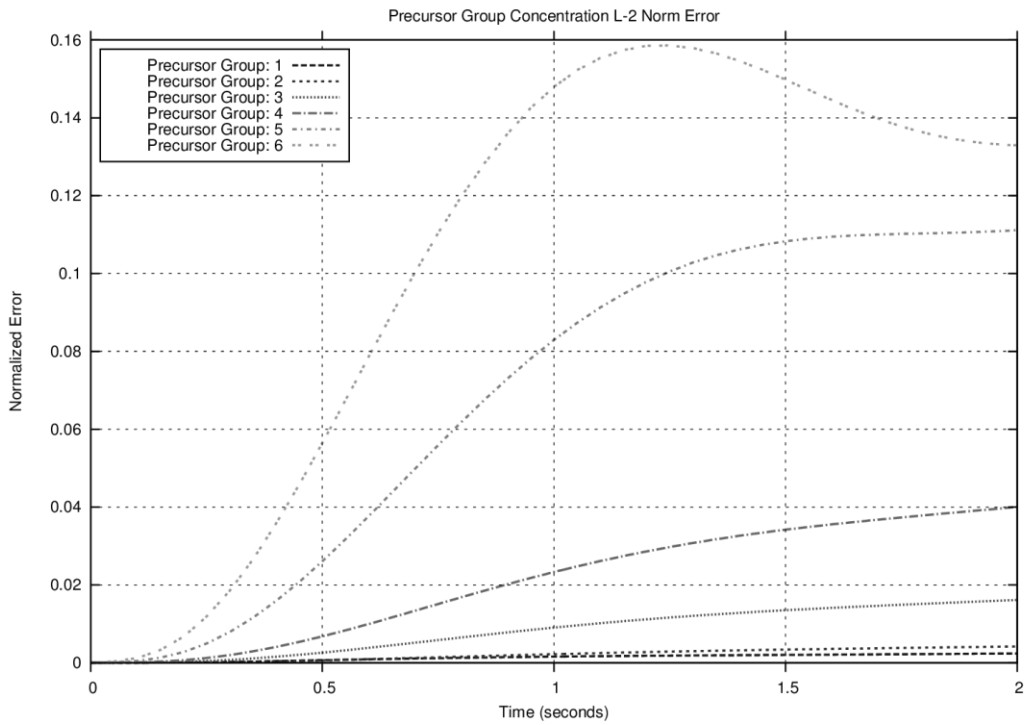

Figure 11: RMS precursor error for 0.002 second rapid-insertion projection operator sets.

3.2.2 Reducing Precursor Error

The AMoR method is designed to allow transition from a low-fidelity to a high-fidelity simulation and back again. In order for this to work correctly, the low fidelity solution must have sufficient accuracy for the high fidelity portion to render properly. The original low-fidelity projection method did not provide sufficient accuracy in the DNP concentration to allow for the restarts to function properly. In order to test the active switching the previous efforts had included a workaround of artificially suppressing the DNP concentration via setting all beta values to 0.0001. This succeeded as it made the relatively large DNP error mostly irrelevant. In order to enable use of AMoR active switching on a real simulation, the restart capability necessitated improving the accuracy of the low-fidelity DNP concentration. This was done by adding internal calculation of low-fidelity delayed neutron precursor concentration using the projected flux in place of using the original direct projection method for the DNP concentration. This newer approach was designated as a hybrid precursor model as it uses the 3-D precursor equations from NESTLE as described in Section 2. These calculations are straightforward and computationally efficient; they do not significantly impact the overall computational cost of the low-fidelity solution.

Once the precursor calculations were in place, for the set of 0.002 second rapid-insertion projection operators used for a 2 second transient, the maximum DNP concentration error was reduced to 15% as seen in Figure 12. The RMS precursor error was reduced to less than 9%, as shown in Figure 13. While the flux and flux errors for the 0.002 second rapid-insertion projection operator set were unaffected by the changed precursor method, they do differ from those presented in previous work [1], which were based on suppressed DNP values. The improvement for the 120 second rod insertion transient is comparable to that of the 2 second rod insertion.

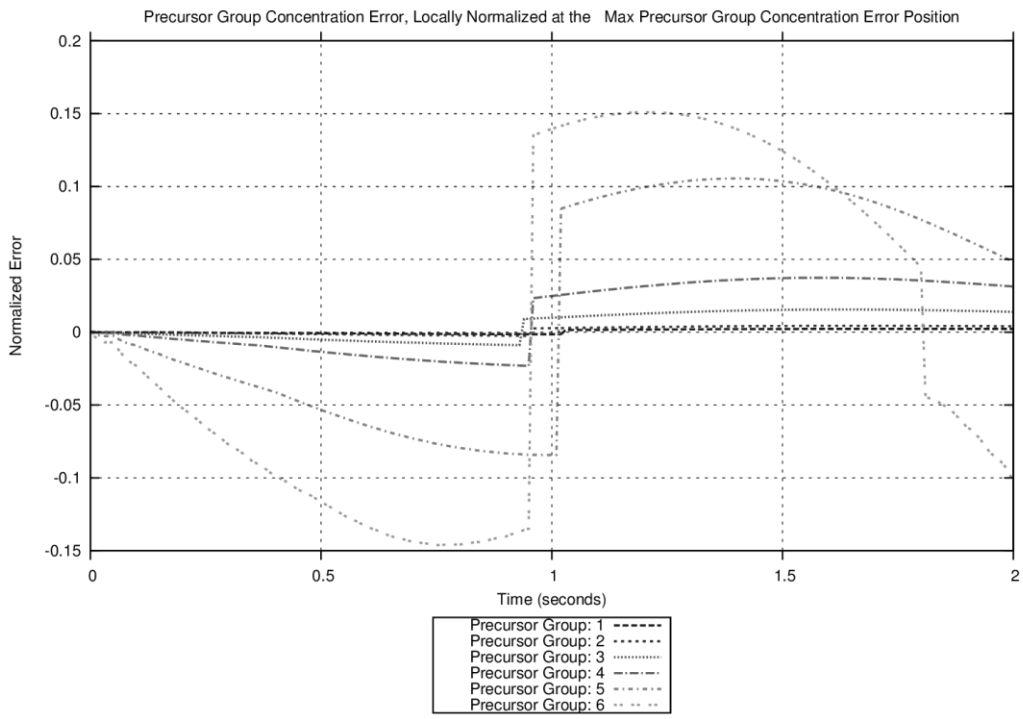

Figure 12: Maximum precursor error for rapid-insertion projection operators hybrid method.

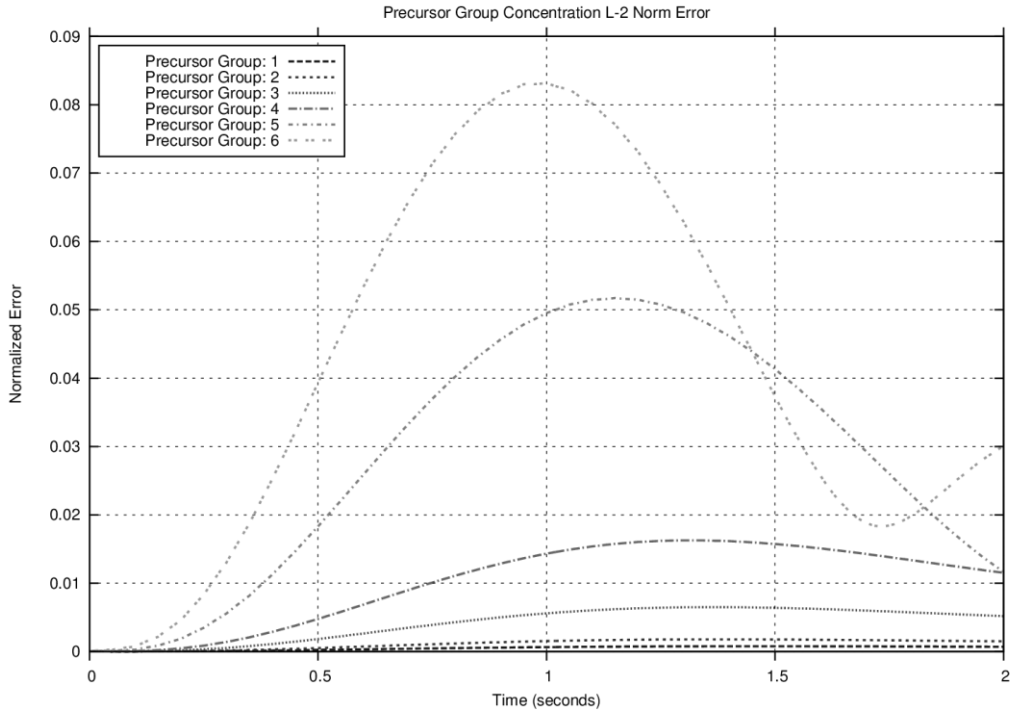

Figure 13: RMS precursor error for rapid-insertion projection operators hybrid method.

At this point the major contribution to DNP concentration errors should be due to errors in the low-fidelity flux. The precursor errors are now sufficiently small that when the projected flux and precursor information are fed back into the high-fidelity model for a shape-factor update, the resulting updated shape-factors lead to significant overall error reduction as seen in Figure 14. These results show similar error behavior to those produced in active switching when delayed neutrons were suppressed, shown in Figure 15. Since there is still some error in the precursors, it is to be expected that the update on the hybrid solution does not result in quite the same magnitude improvement as compared to when the precursor values were artificially made insignificant. The updates were done using restart parameters identical to the original settings used by Satterfield [1]; they are examined more in Section 3.3.5.

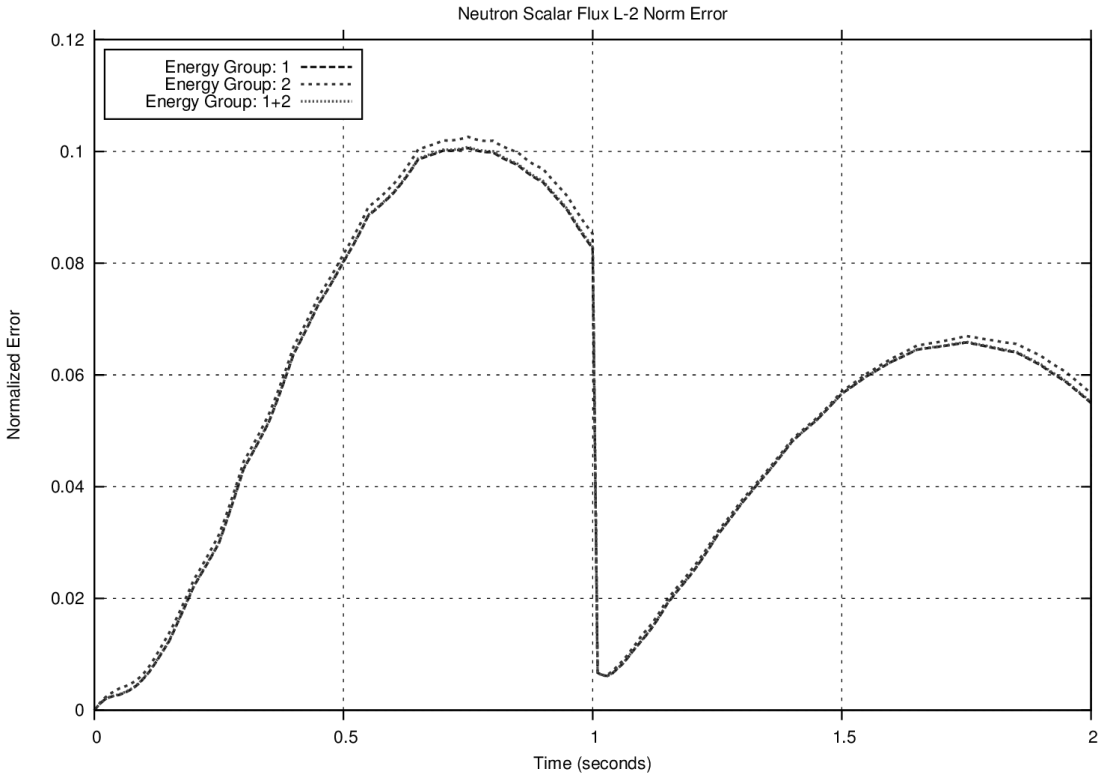

Figure 14: RMS flux error for 0.002 second rapid-insertion projection operators hybrid method, with one switch halfway through the 2 second transient.

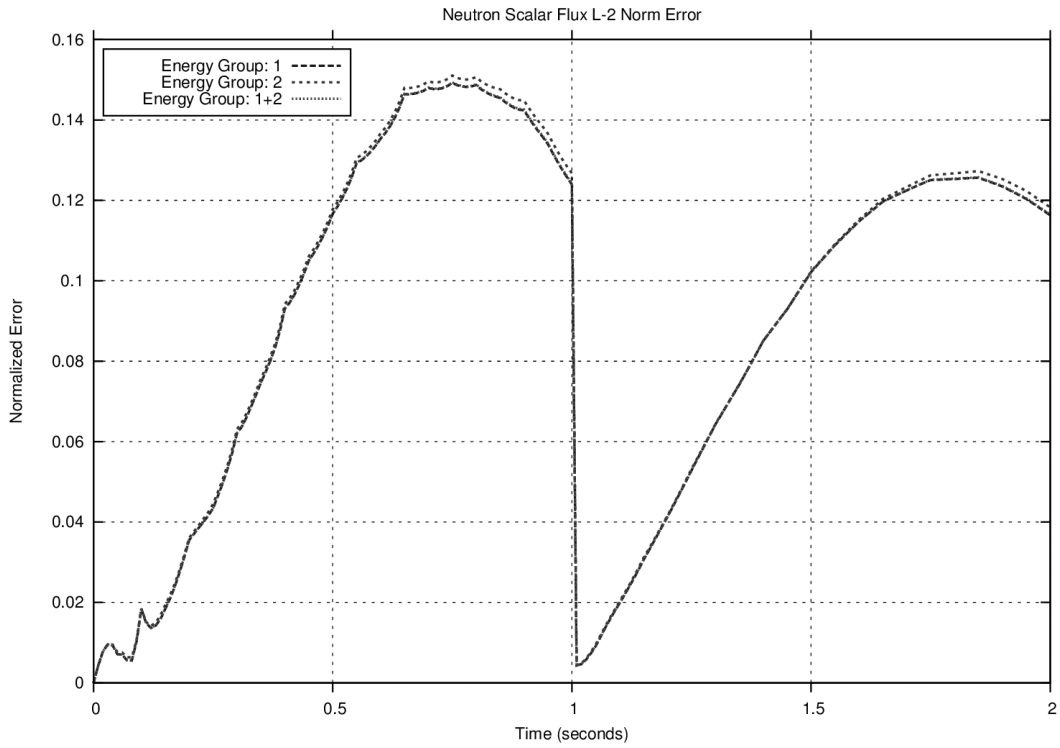

Figure 15: RMS flux error for rapid-insertion projection operators with suppressed DNPs and projected precursors method, with one switch halfway through the 2 second transient.

Testing to verify that the precursor values were being calculated correctly revealed a non-zero (greater than machine error) minimum precursor error level, even when using flux values imported from the high-fidelity solution. This was determined to be due to regular minor fluctuations (appearing as bumps) in the neutron density calculated within NESTLE over the transient, which cannot be entirely captured by interpolation even with reasonably increased number of data points. Minor differences in flux history between the interpolated high-fidelity flux and the true high-fidelity flux lead to small, but accumulating, differences over time in the precursor values derived from those fluxes. These small fluctuations in neutron density are most likely due to limitations within NESTLE in modeling flux at the node containing the rod-tip.

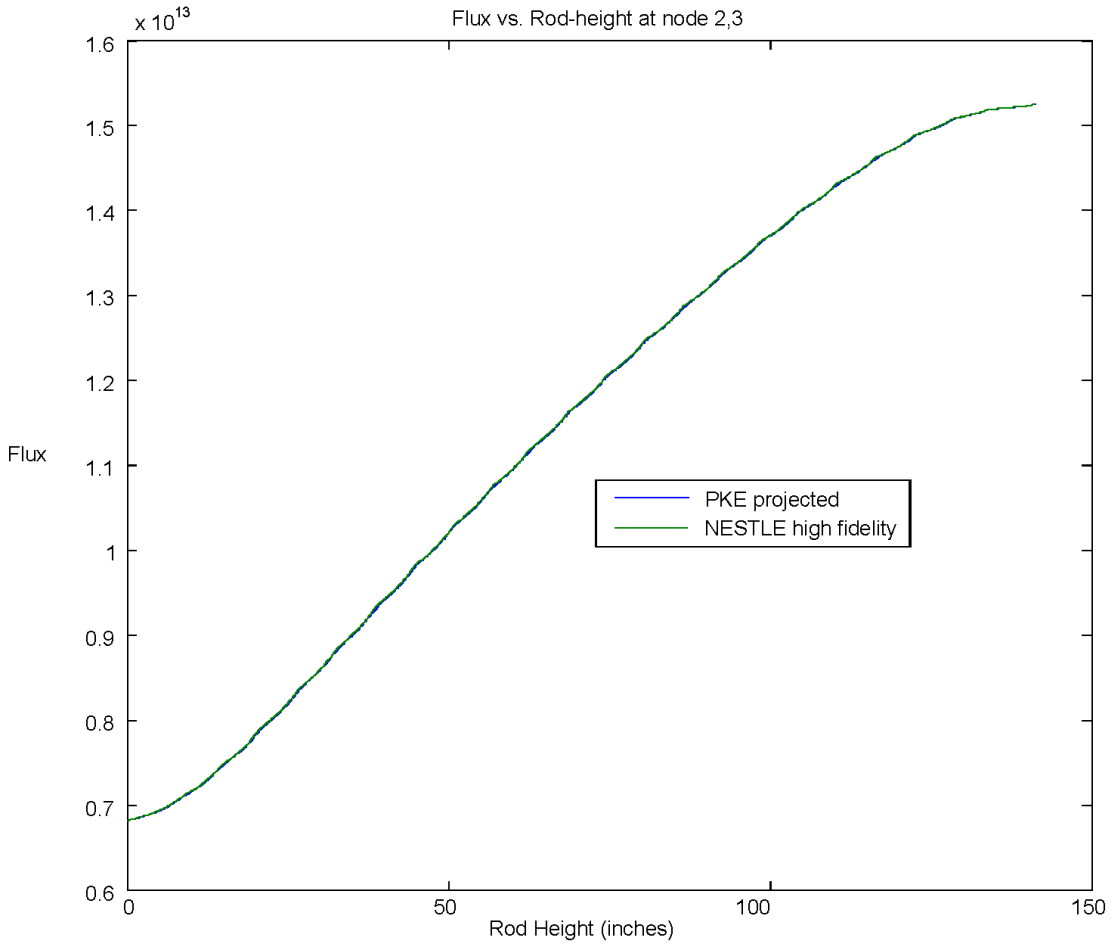

Figure 16: Neutron flux vs. Rod Height at a non-rodded location.

To clearly see the fluctuations, the difference between a PKE projected flux using high-fidelity data values for the projection, and the true NESTLE flux are plotted against rod position in a representative non-rodded location in Figure 16 and Figure 17.

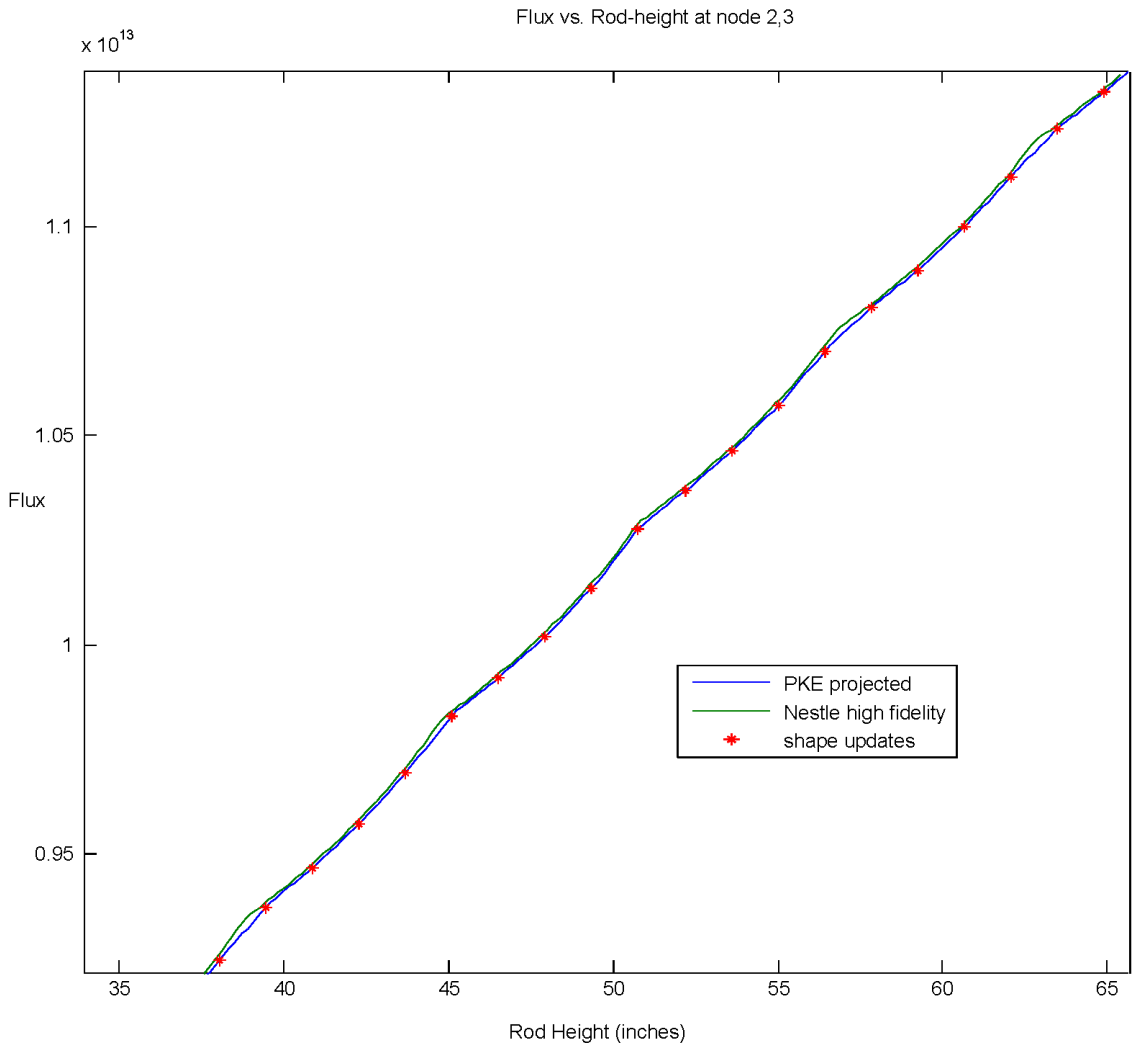

Figure 17: Neutron flux vs. Rod Height, zoomed in, at a non-rodded location.

The tests were repeated in the combined code discussed in section 3.2.3, with continuous transfer of flux values from the high-fidelity solution to the precursor calculations. Delayed neutron precursor calculation results were then found to be off by less than machine error.

3.2.3 New AMoR Layout

As part of continuing work on potential future publication/release of the code as a fully functional package, further modifications were performed to streamline and simplify the code for Adaptive Model Refinement in order to include it as a side capability within NESTLE. A significant portion of the original AMoR code had been set up to handle transfer of data between the separate PKE and NESTLE programs. With PKE and the AMoR functions running within the NESTLE environment, much of this data transfer became unnecessary and the associated subroutines were pared down or removed. After import, the AMoR functions and calls were structured as shown in Figure 18.

The user now has the option of comparing the low-fidelity solution to interpolated data from a pre-solved high-fidelity solution as in the original AMoR setup, or using data directly imported from a concurrently running high-fidelity solution. If the saved high-fidelity option is selected, only the portions of the NESTLE transient routine that regulate rod height and transient time are configured to run, as these data also govern the PKE transient and AMoR routines. Using saved transient data is significantly faster than concurrent data. Currently, all runs still begin with a high-fidelity steady-state initialization, which does add computation time. An additional feature in the version of NESTLE used for this project is that if PKP data are not available the program will automatically produce it prior to re-initializing steady-state and running the transient. PKP data production is computationally significant as it involves several steady state forward and adjoint calculations. Fortunately the PKP data do not require recalculation unless the method of reactivity change or core data are modified. At this stage, the subroutines which control shape-factor creation and updating have not been transferred and are still contained in a separate version of NESTLE. Subsequent to unification into a single code, updates will still require running a separate instance of the program to use the NESTLE restart capability.

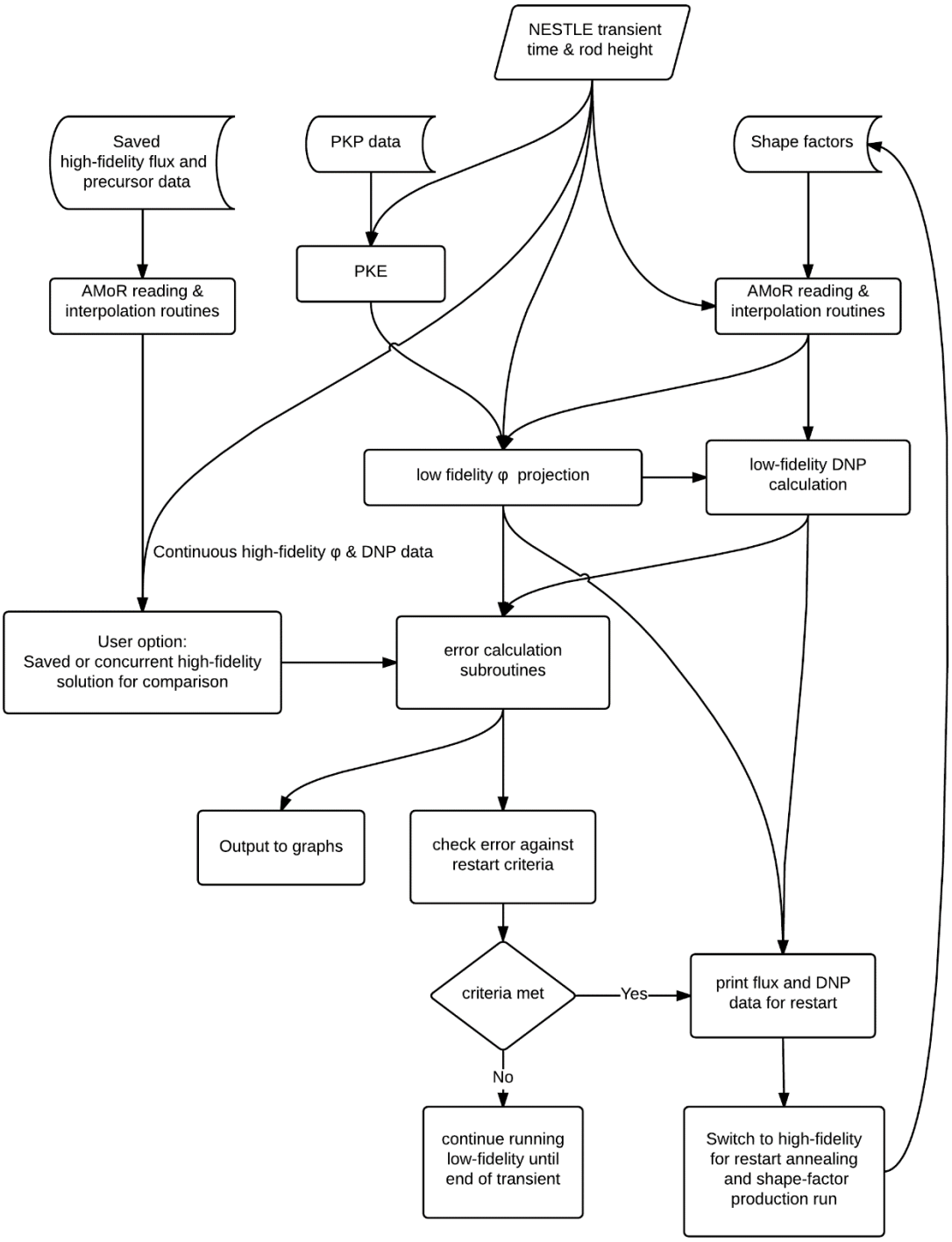

Figure 18: Current AMoR setup

3.2.4 Additional Modifications

The original scope of AMoR was to investigate the accuracy of modeling flux and precursors during a rod insertion transient. In order to provide low-fidelity modeling capabilities for a wider variety of transients, the codes and subroutines required modifications. Capabilities added thus far include modeling a rod withdrawal transient and extending modeling of the low fidelity transient to include times after rod motion has stopped. The low-fidelity solution can also now be used as input to calculate error responses, as described in Section 2.6.

Test results of the rod withdrawal transient appeared to be reasonable. Figure 19 shows the PKE calculated vs. NESTLE calculated average neutron density for a 2 second rod withdrawal transient with 0.5 seconds of subsequent transient shown. Figure 20 and Figure 21 show the maximum and RMS flux errors while Figure 22 and Figure 23 show the corresponding precursor errors. To be consistent with the original rod-insertion tests, a 0.002 second rapid rod withdrawal was used to produce the low-fidelity projection operators for this test.

The rod-withdrawal capability is clearly functional, however, the accuracy of the low-fidelity model is challenged by the rate at which power and average neutron density change. It is clear that there is significant error present in the flux, and especially the DNP concentration. Examining the increasing separation of the high-fidelity and low-fidelity neutron densities as the transient progresses, it is certain that this contributes greatly to the flux error in the latter portions of the transient. Additionally, the growing DNP error should be expected considering the rather large error in the low-fidelity neutron flux. There is, however, an additional source of error in the neutron flux. This additional error has been identified and will be discussed in Section 3.3.

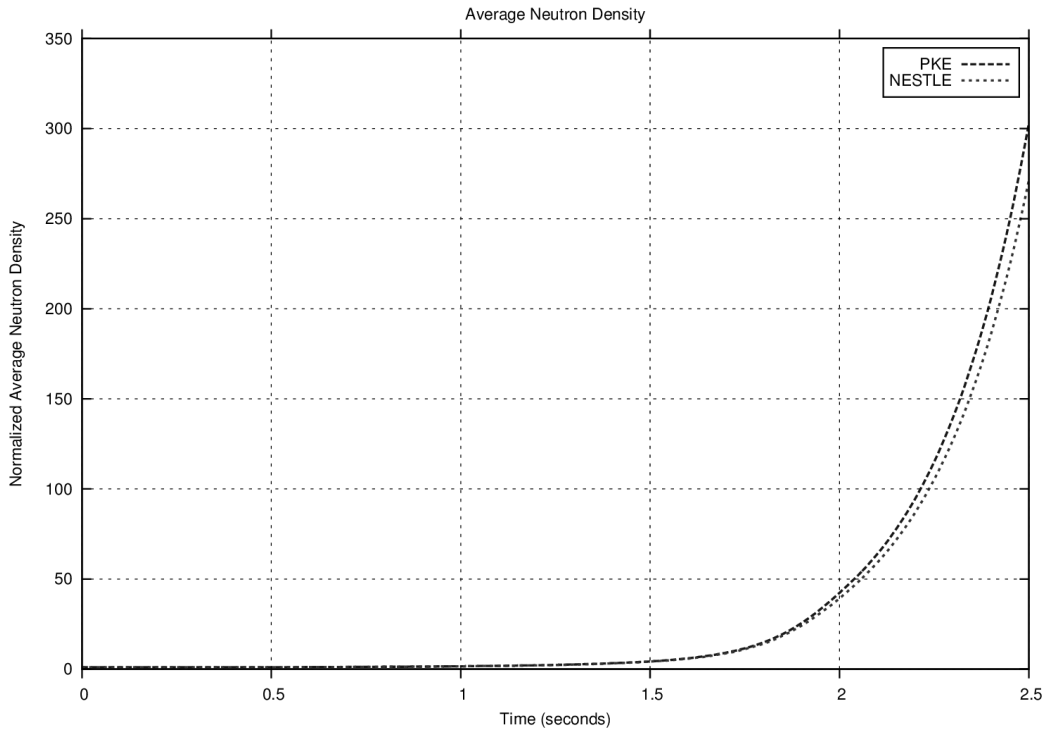

Figure 19: 2 second rod withdrawal transient average neutron density.

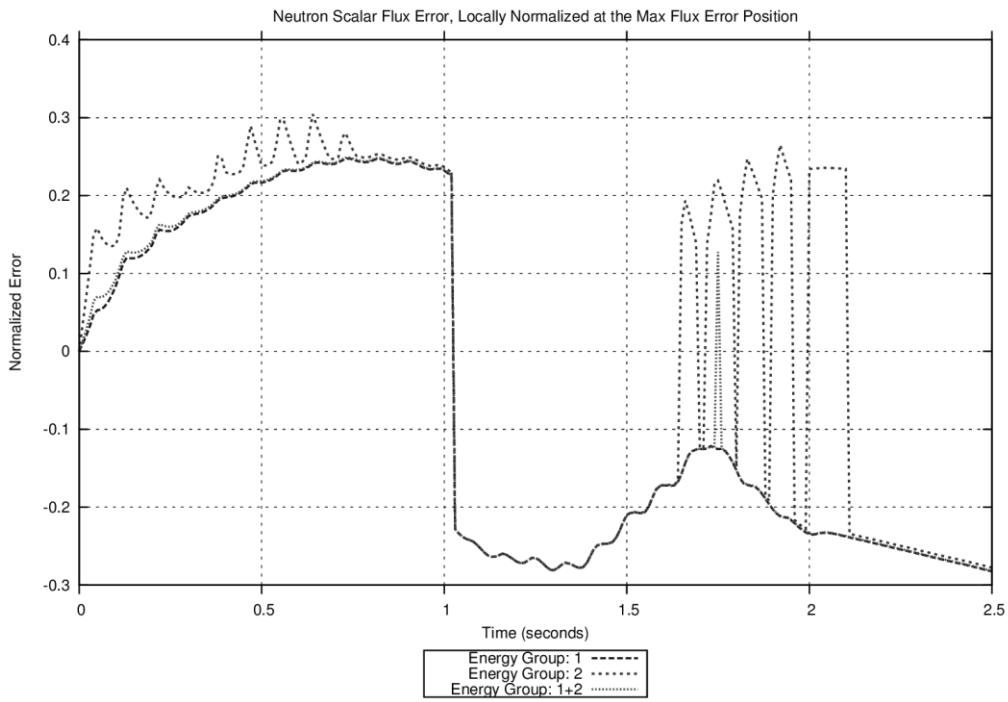

Figure 20: 2 second rod withdrawal transient maximum flux error.

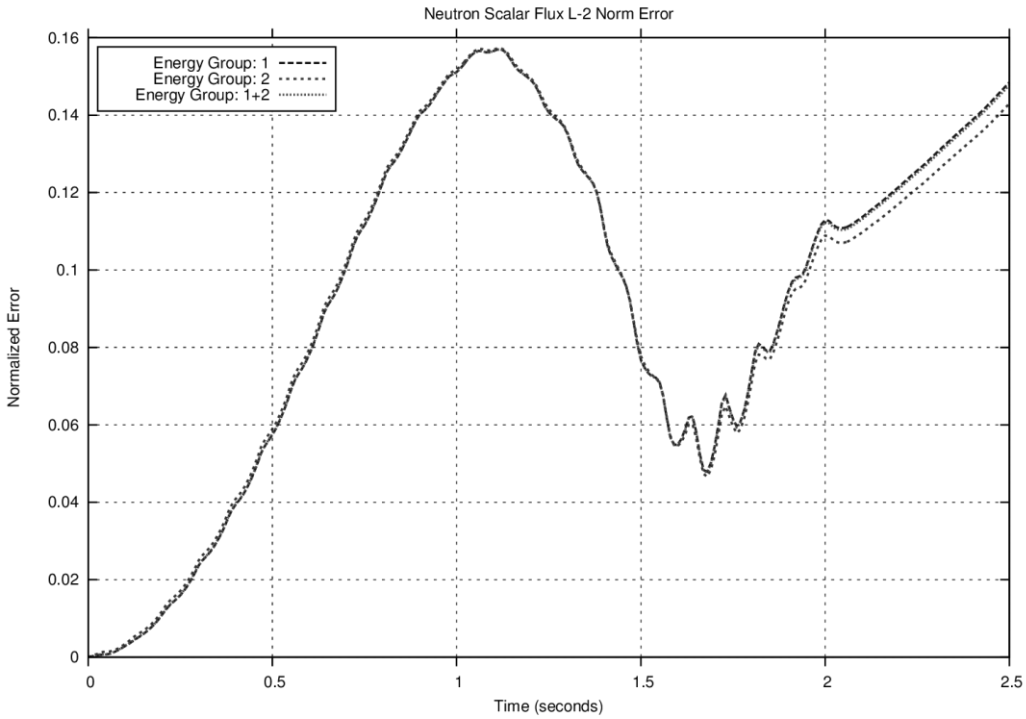

Figure 21: 2 second rod withdrawal transient RMS flux error.

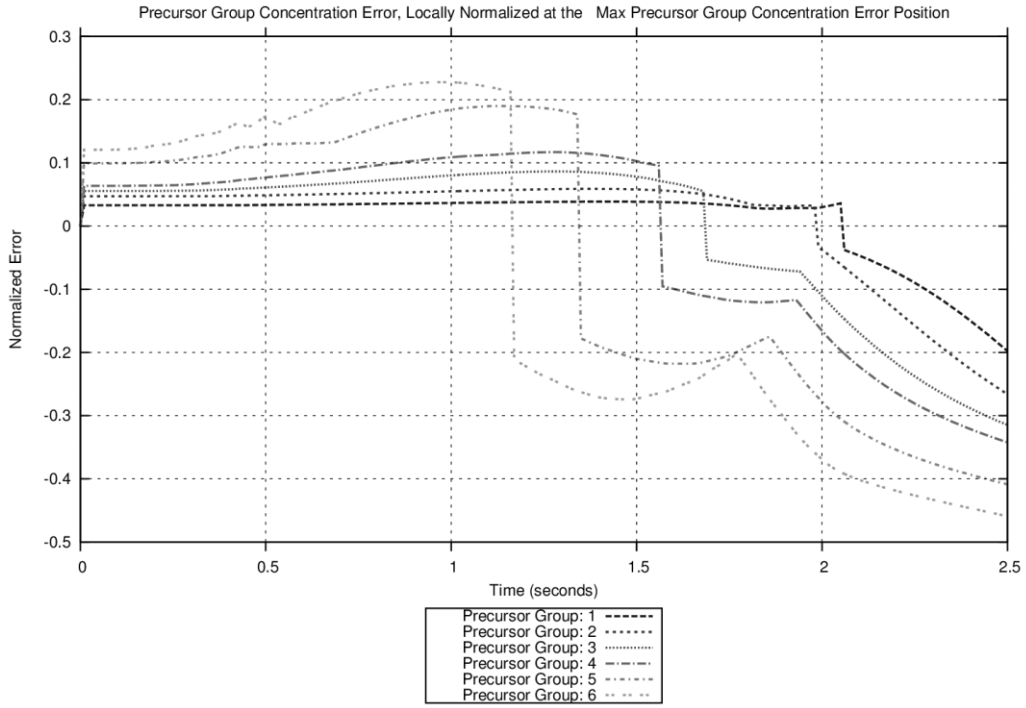

Figure 22: 2 second rod withdrawal transient maximum precursor error.

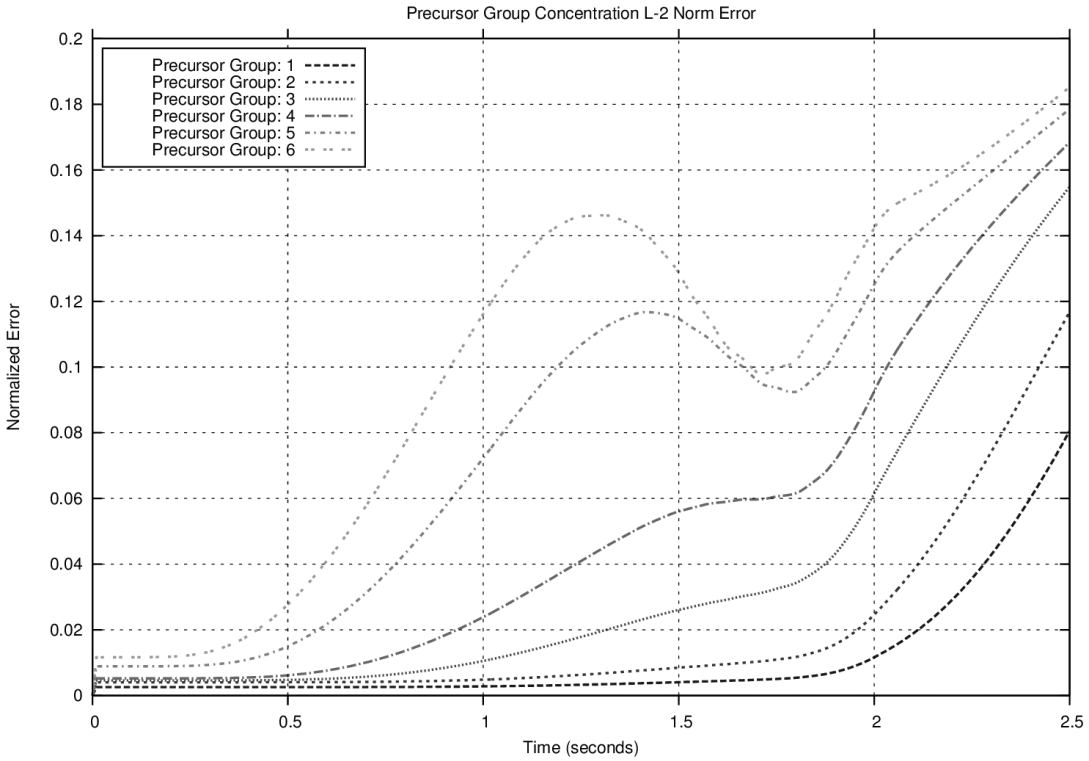

Figure 23: 2 second rod withdrawal transient RMS precursor error.

During rod motion, the low-fidelity projection operators and high-fidelity solution are read in and interpolated based on rod position. After rod motion ends, the data are switched to a time-based input for the high-fidelity solution. The low-fidelity solution after this point uses the last set of projection operators, as flux shape changes after rod motion ends are expected to be relatively subtle.

When modeling very long transients it was determined that attempts to reduce the frequency of the high-fidelity snapshots lead to significant interpolation errors that overpower all other error sources. Maintaining the original frequency for long follow-up times would be very resource-intensive. For this reason the evaluation of the success for the extended transient modeling was done using the most error significant projection operators, specifically the flux shape-factors. In the extended transient the projection operators at the end of rod motion are used for the remainder of the

transient, thus all changes in error after that point arise from changes in the "true" solution. As seen in Figure 24, there is a continuing variance in the flux shape following the end of rod motion, doubtless due to delayed neutrons.

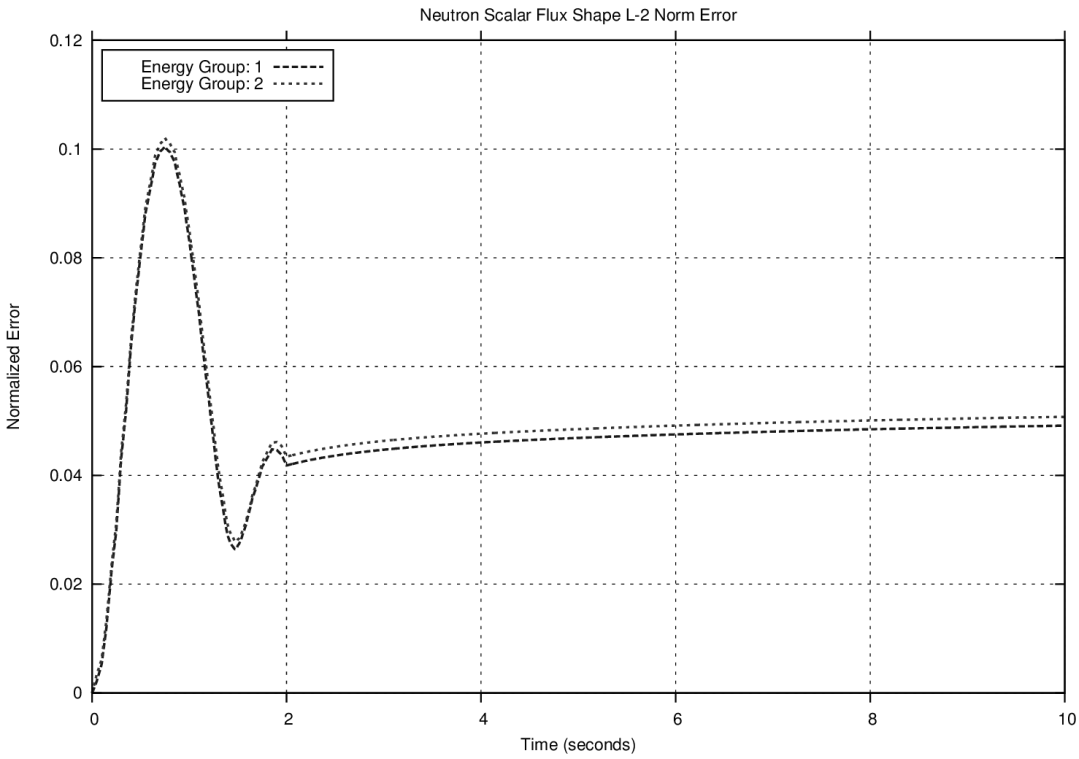

Figure 24: 2 second rod insertion, RMS flux-shape error extended

After rod motion ends there is a residual error in the flux shape leftover from the rod motion transient. The flux shape can be permanently improved with a single update after the motion stops. As Figure 25 shows, there will still be some subsequent error growth due to flux shape changes arising from delayed neutrons.

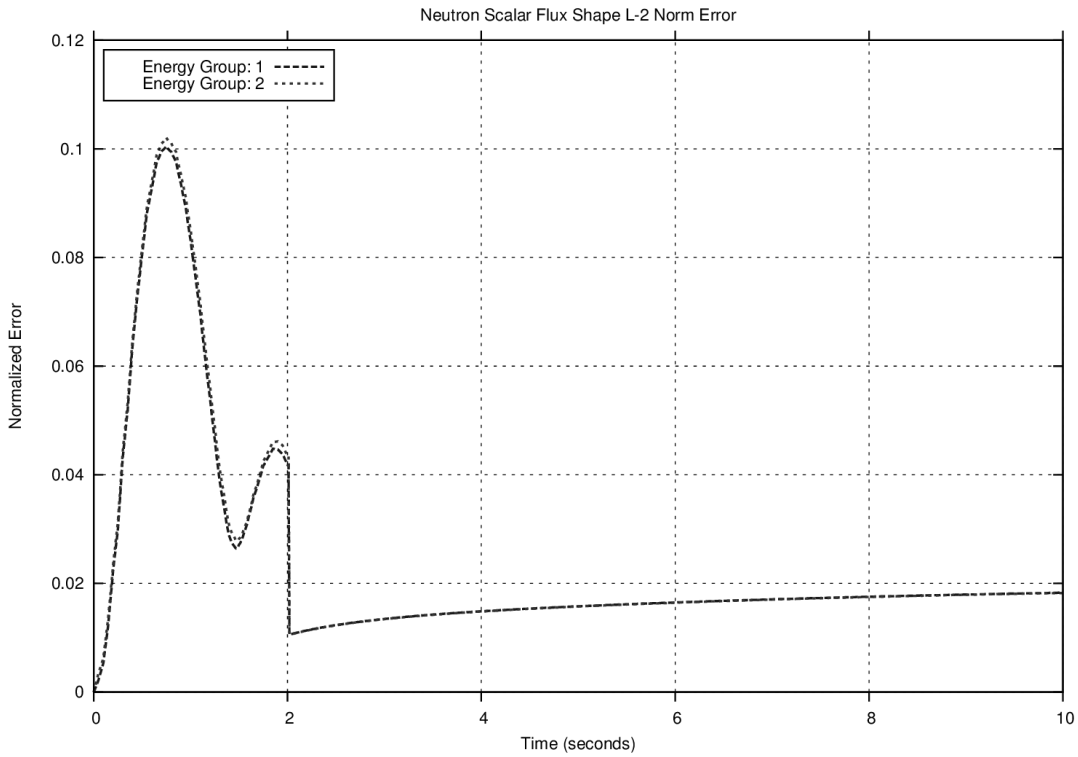

Figure 25: 2 second rod insertion, maximum flux-shape error extended, with restart.

In support of the subsequent employment of an adjoint method for error prediction, the low-fidelity solution can be used to produce a residual, which is used to calculate an error response, as described in Section 2.6. The adjoint error response can be compared to the forward error response to demonstrate that the response calculations are valid. A sample output was produced from a 2 second rod withdrawal, preceded by 0.5 seconds of null transient and followed by 0.5 seconds of settling time. The low-fidelity solution was produced using the 0.002 second rapid insertion transient projection operators. The sample error response output is contained in the appendix.

3.3 Improving the Low-Fidelity Model

Previous work by Sterling Satterfield [1] revealed that the primary source of error in the low-fidelity solution is specifically the shape-factors, as shown in Figure 26. There is clearly a very strong correlation between the flux shape-factor error and the flux error. This relationship holds true for all locations and neutron energy groups. Since the other components of the projection contributed relatively little to the magnitude of the flux error, and the DNP concentration is directly dependent on the flux, it was decided that efforts to reduce the error of the low-fidelity model would be focused on improving the flux shape-factors.

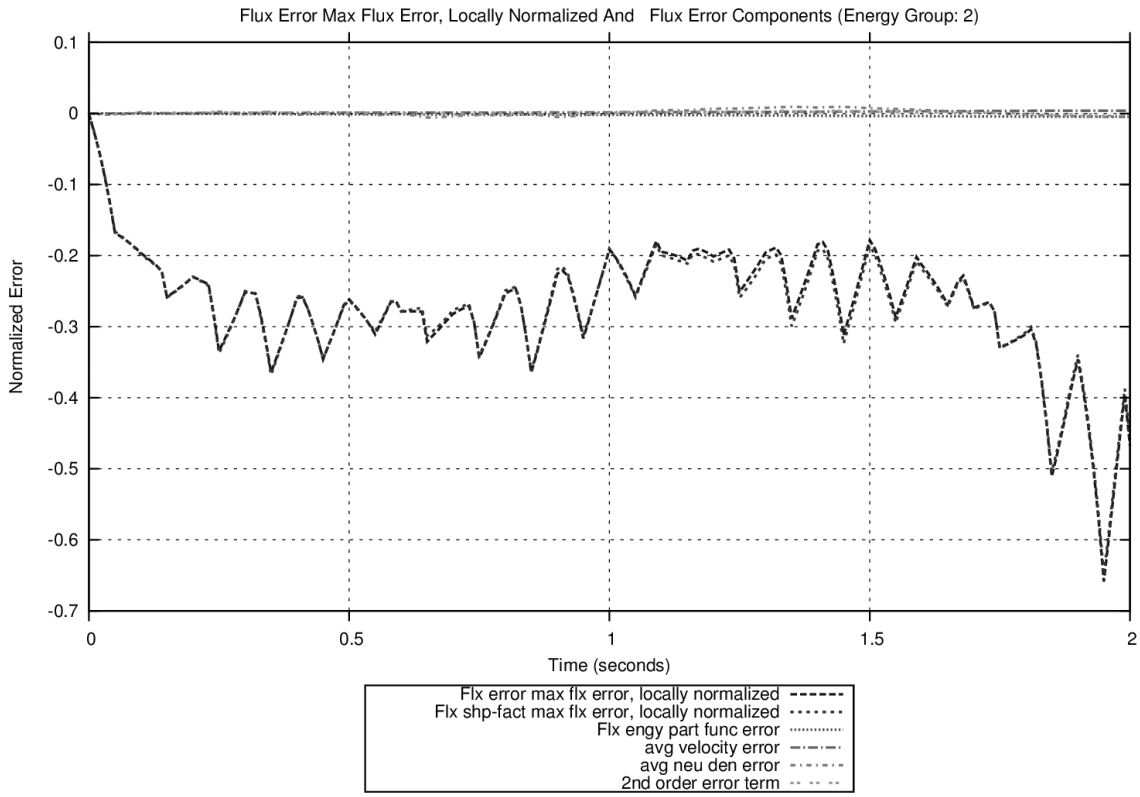

Figure 26: 2 second transient flux error components.

3.3.1 Flux-shape Error Source

It seems reasonable to assume that the error in the shape-factors should be due to the difference in delayed neutron behavior between the 0.002 second rapid insertion used to produce the shape-factors, and the full transient of interest. Therefore, if the delayed neutron error contribution is minimized, there should be a reduction in error. This was tested by revisiting the artificial suppression of delayed neutron precursors by setting all beta values to 0.0001 for the two second transient. This beta value was selected for the test due to being less than half the smallest values and significantly lower than the largest. Additionally, further reductions to the beta values had little effect on the RMS flux shape error, but added noticeable error to the low-fidelity PKE calculation of average neutron density versus the NESTLE calculated average neutron density, most likely due to the greater speed of the associated power drop, shown for each tested set of beta values in Figure 27 - Figure 29.

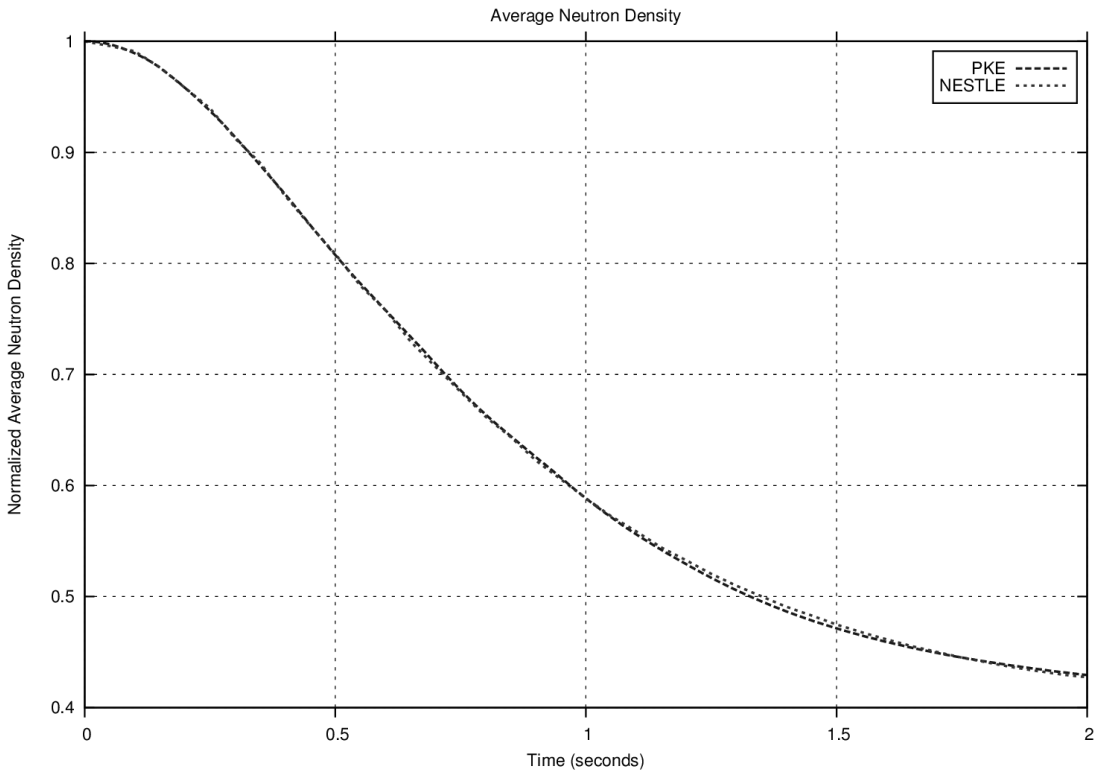

Figure 27: Average neutron density, 2 second rod insertion, normal beta values.

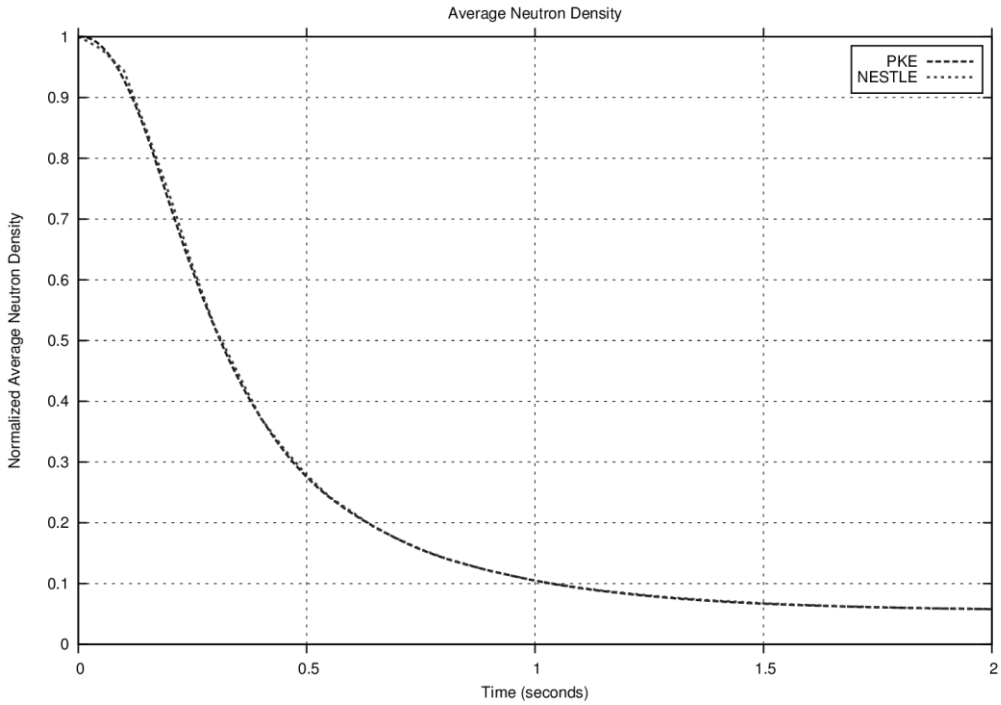

Figure 28: Average neutron density, 2 second rod insertion, 0.0001 beta values.

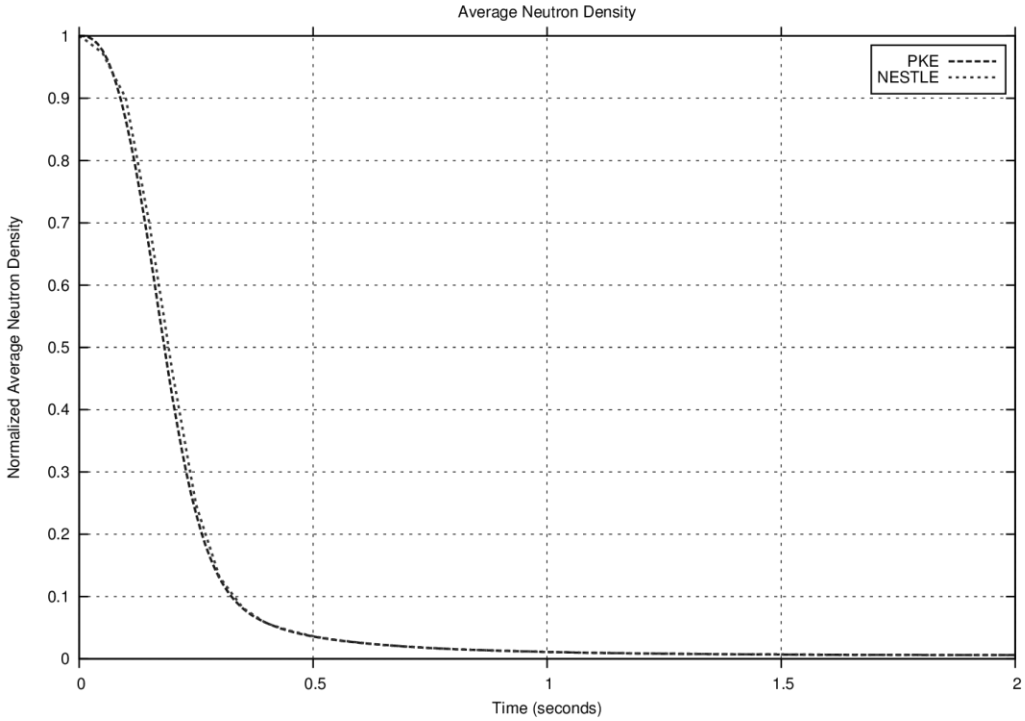

Figure 29: Average neutron density, 2 second rod insertion, 0.00001 beta values.

Since with suppressed DNP concentration the average neutron density does contribute noticeably to the RMS flux error, the analysis was performed primarily on RMS flux-shape error. Figure 30 and Figure 31 show the close relationship between RMS flux and RMS flux shape errors when the high-fidelity and low-fidelity average neutron density agree closely.

Interestingly, for the 2 second transient, the reduction of the delayed neutron term actually caused a 40-50% increase in the RMS flux-shape error, without changing the general behavior over time, as shown in Figure 31 - Figure 33. This suggests that the errors present in these shape-factors are *not* directly attributable to delayed neutrons. Tests where the information from the full transient was used for the shape-factors consistently produced no flux shape error and RMS flux error that closely resembled the average neutron density error. This provides confidence that the RMS flux error results are not an artifice of coding error.

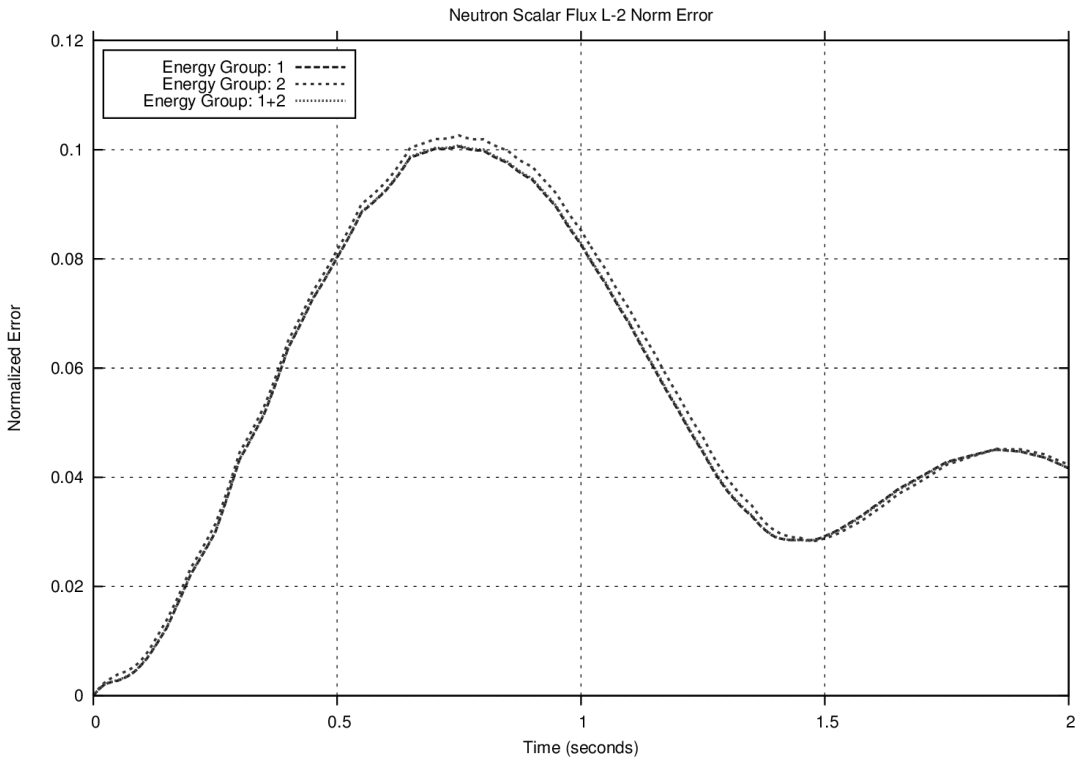

Figure 30: RMS flux error, 2 second transient, normal beta values, 0.002 second projection operator set.

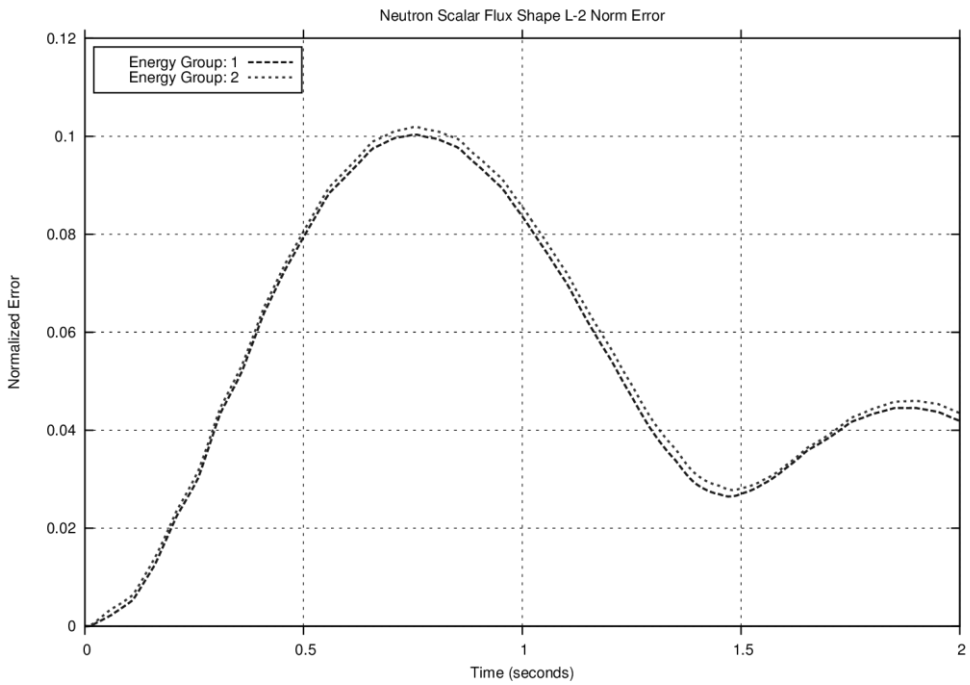

Figure 31: RMS flux shape error, 2 second transient, normal beta values, 0.002 second projection operator set.

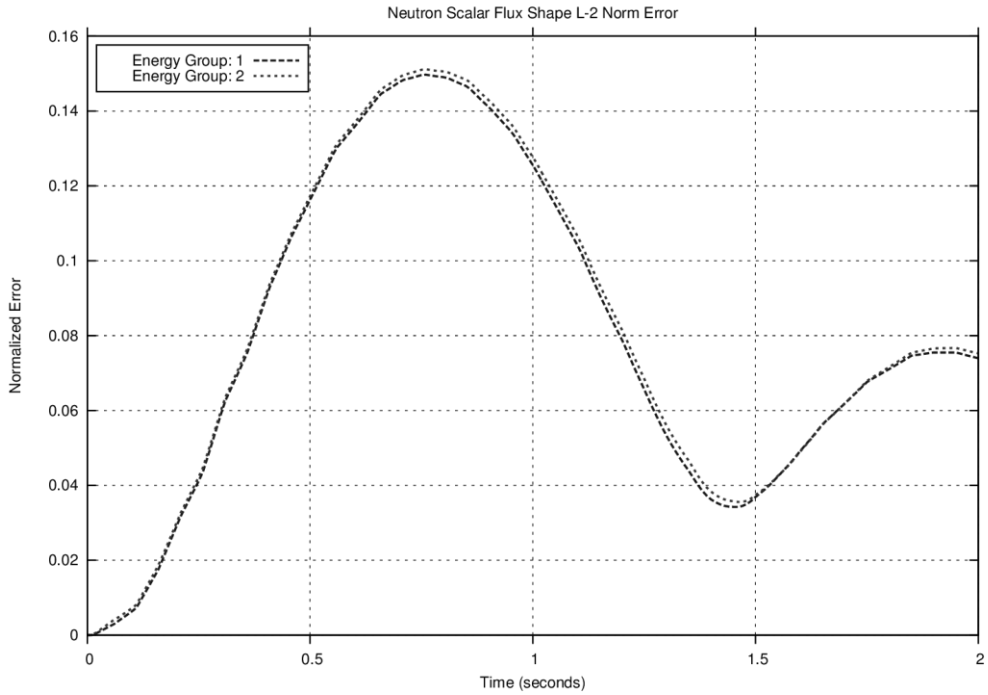

Figure 32: RMS flux shape error, 2 second transient, 0.0001 beta values, 0.002 second projection operator set.

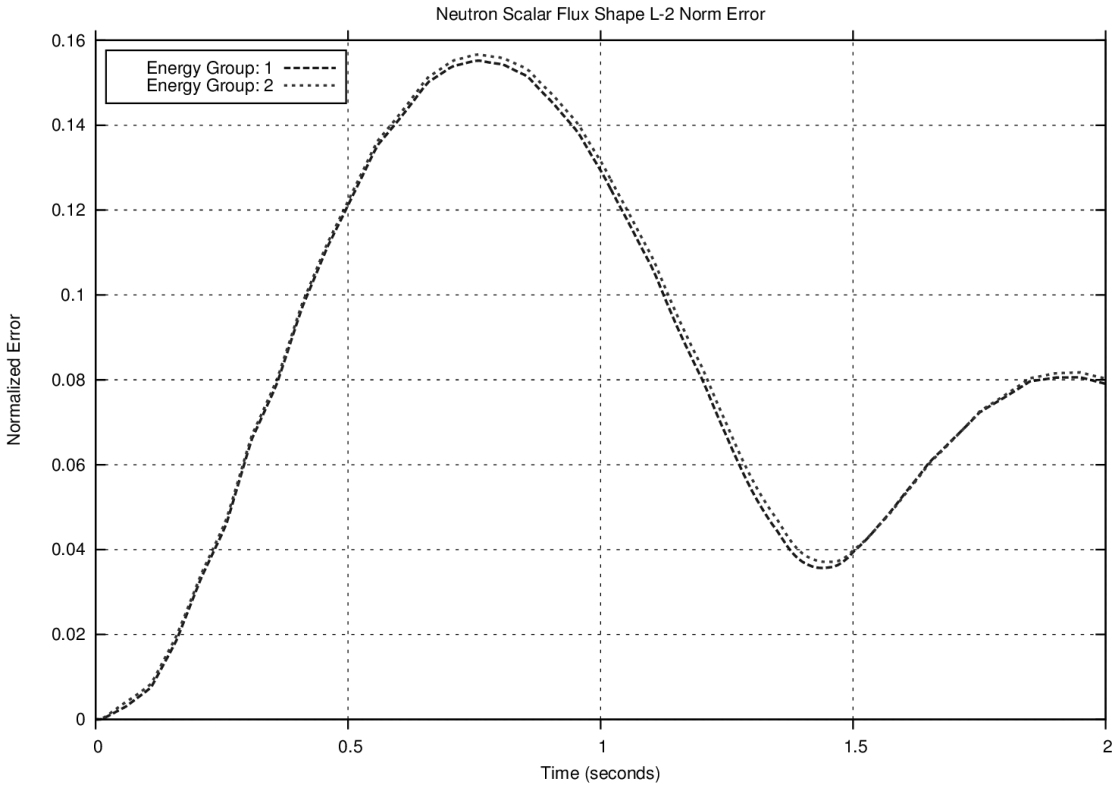

Figure 33: RMS flux shape error, 2 second transient, 0.00001 beta values, 0.002 second projection operator set.

3.3.2 Prompt Neutron Induced Error Tests

A test, with suppressed betas, to examine whether the timeframe of the rapid insertion for producing the projection operators might be contributing to the error, showed significant change in magnitude and behavior when the timeframe of the rapid insertion was changed from 0.002 seconds, as seen in Figure 32, to 0.01 seconds, shown in Figure 34. This promotes the idea that the 0.002 rod insertion might be fast enough to be affected by prompt neutron transient behavior. This comparison was also performed for the 120 second transient, with similar results, as demonstrated by comparing Figure 36 to Figure 37. Further tests included comparing the flux shape of the 2 second transient to the 120 second transient by using the saved high-fidelity 2 second transient data as the projection operators for the 120 second low-fidelity transient with suppressed betas; see Figure 38. The error was drastically smaller in this case, even though there is a significant difference in delayed neutron behavior between the two transients. This supports the conclusion that the majority of the error in the original set of rapid insertion shape-factors is not due to delayed neutrons.

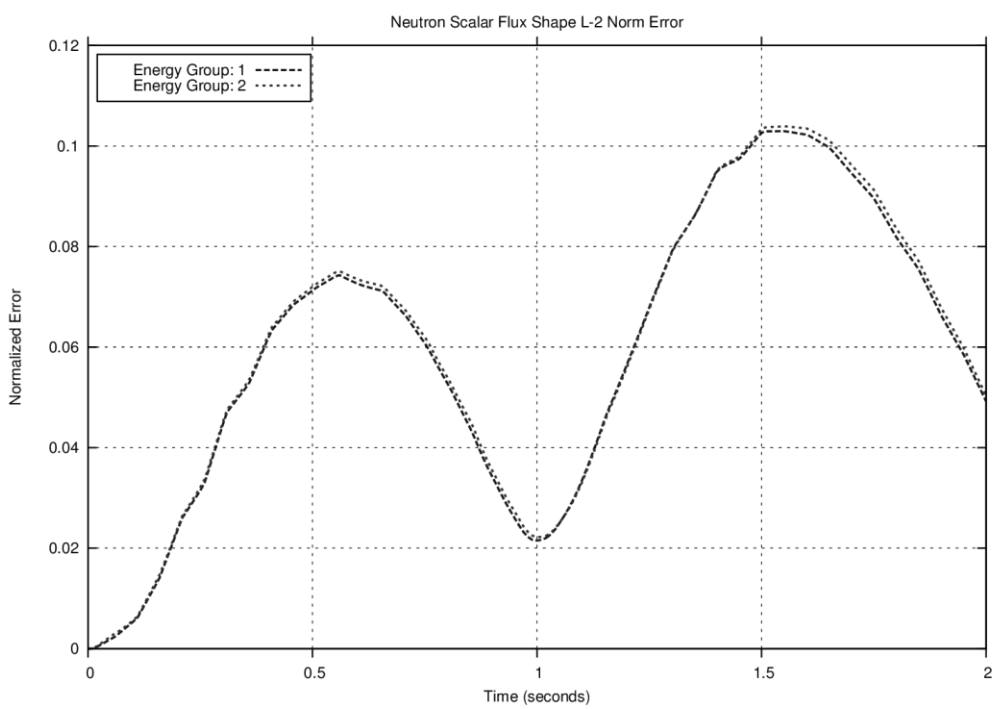

Figure 34: RMS flux shape error, 2 second transient, 0.0001 beta values, 0.01 second projection operator set.

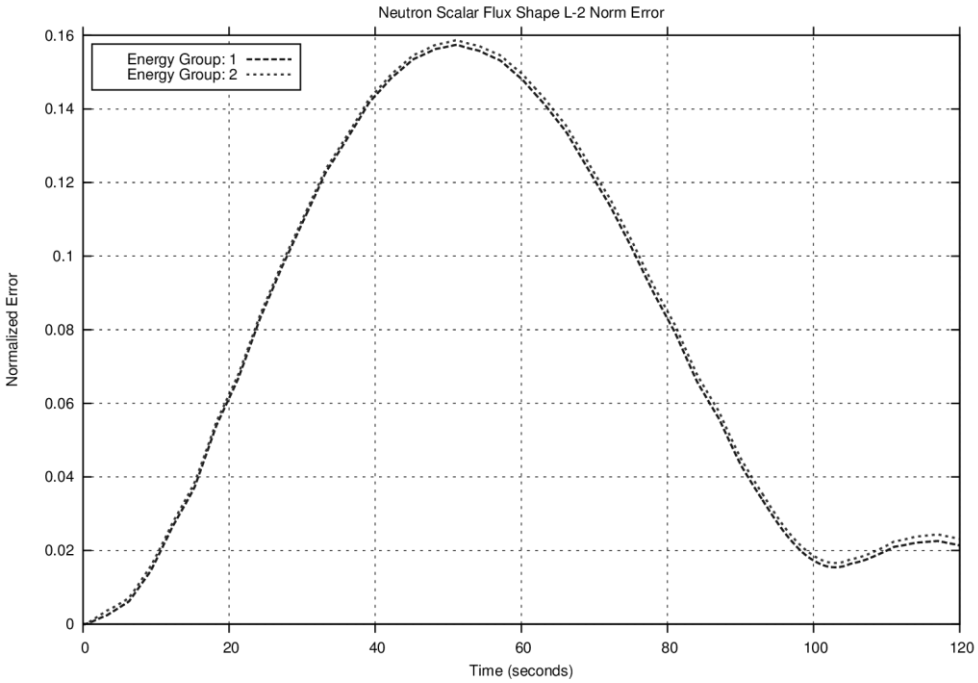

Figure 35: RMS flux shape error, 120 second transient, normal beta values, 0.002 second projection operator set.

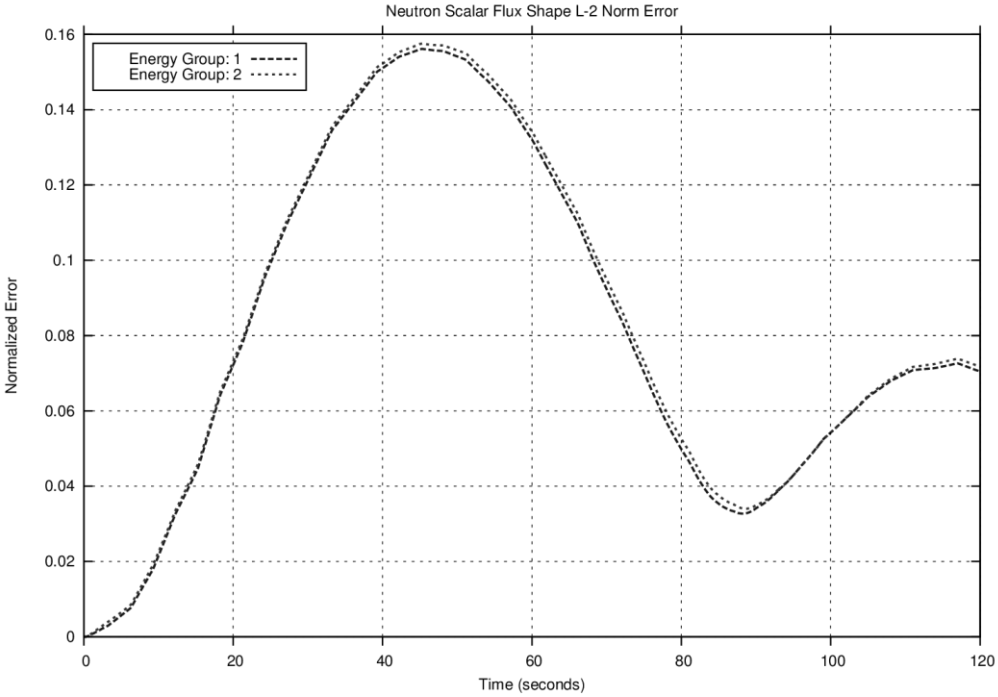

Figure 36: RMS flux shape error, 120 second transient, 0.0001 beta values, 0.002 second projection operator set.

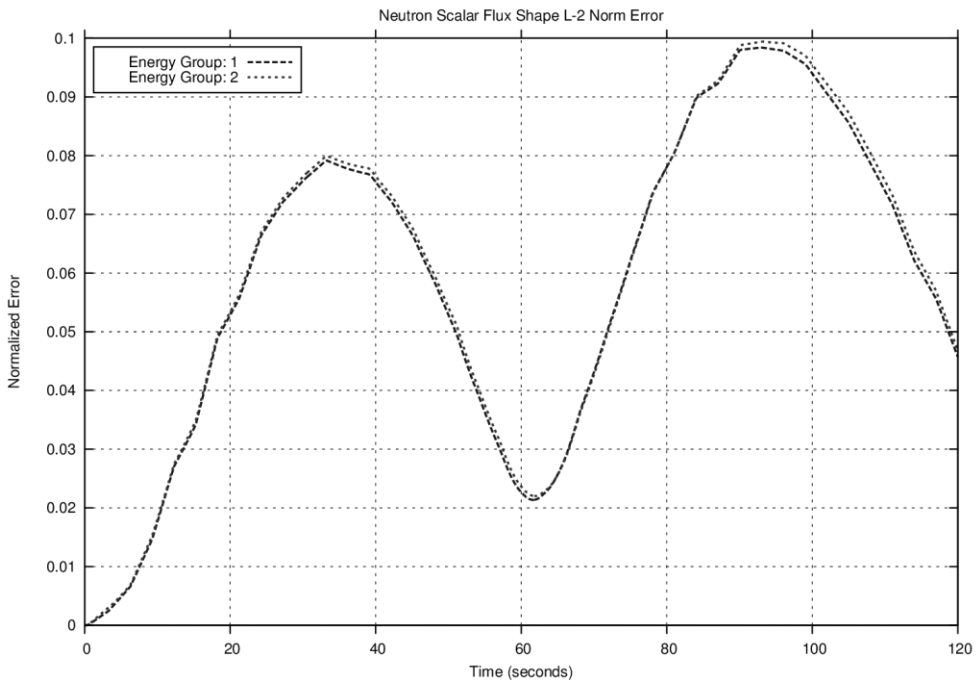

Figure 37: RMS flux shape error, 120 second transient, 0.0001 beta values, 0.01 second projection operator set.

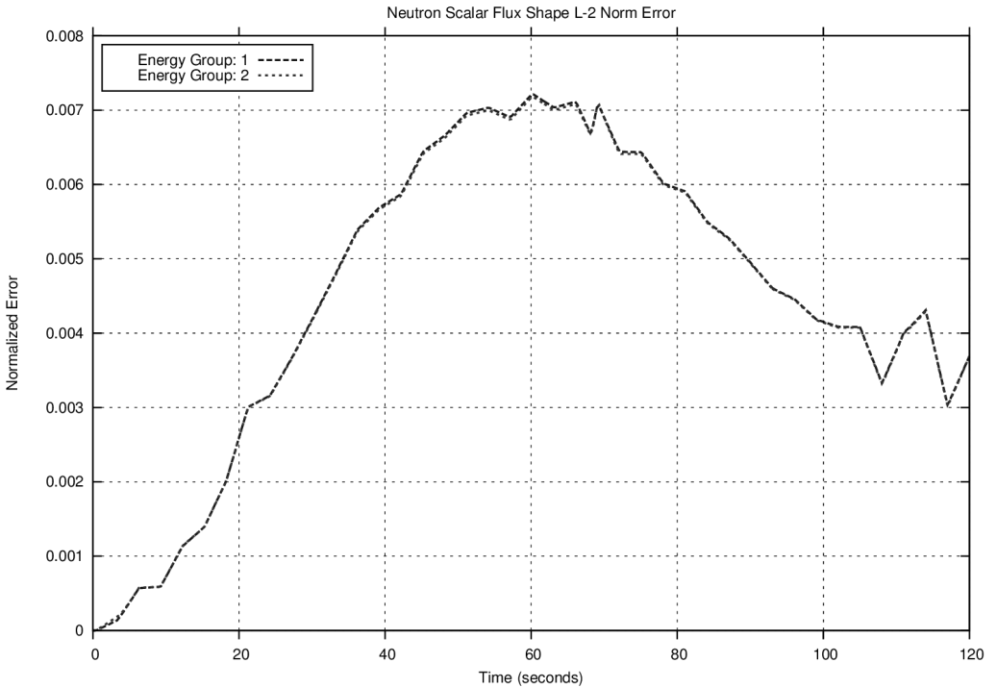

Figure 38: RMS flux shape error, 120 second transient, 0.0001 beta values, 2 second projection operator set.

To examine the extent of prompt neutron induced variability in the shape-factors, a step-insertion run was performed with normal beta values. The step-insertion was done using standard low-fidelity shape-factors with consistent beta values, but used the concurrently generated high-fidelity flux option, rather than saved, in order to capture the fleeting prompt neutron effects on flux shape. The shape-factors are not expected to minimize error, only provide a constant value for comparison, though without delayed neutron effects, the relative error is minimal after the prompt neutron effects settle out. In Figure 39, with normal beta values, the flux shape takes approximately 0.001 seconds to approach a steady value, and 0.003 seconds to largely settle out. The time for flux shape to roughly settle out after rod motion is on the order of the time of the entirety of the original projection operator production run, at 0.002 seconds. It is clear from these results that more time is needed to allow the initial flux shape variations to die down following rod motion.

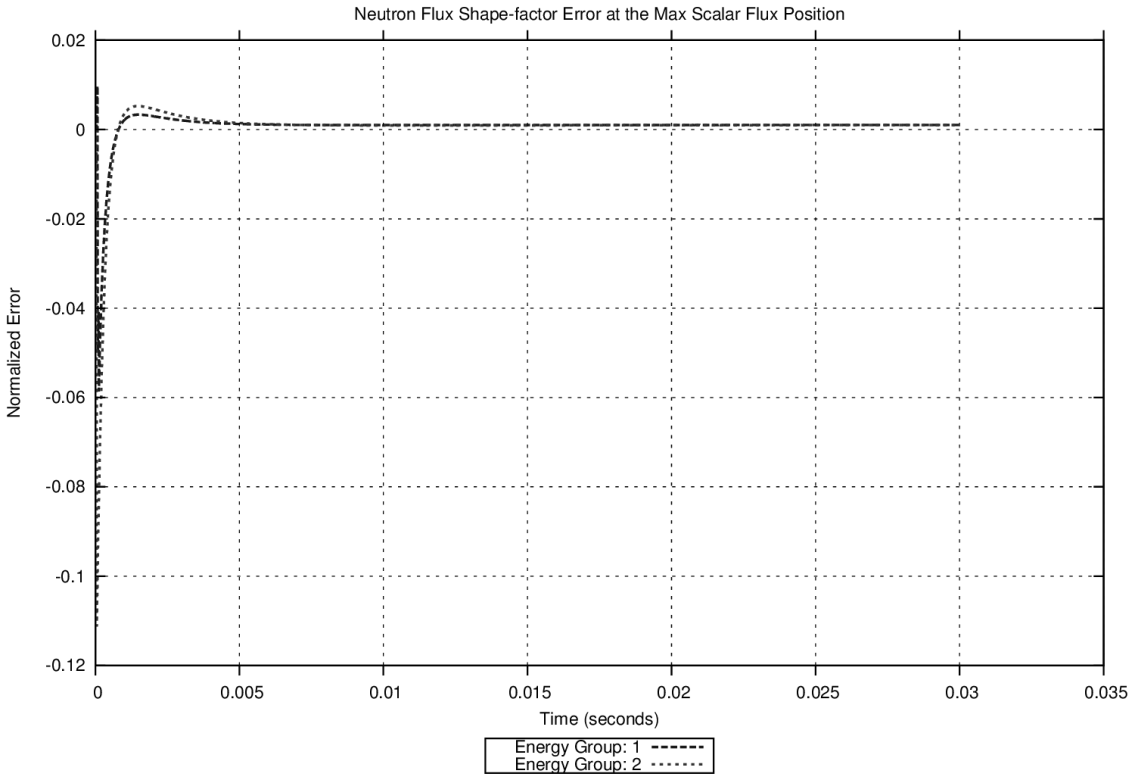

Figure 39: Hot-spot flux shape error, step insertion transient, normal beta values.

In order to further examine the extent to which the accuracy of the projected model is affected by the timescale of the shape-factor production run versus the life-time of the neutrons, the step-insertion run with normal beta values was repeated with varying neutron velocity. When neutron velocity was multiplied by a factor of 1.1, thereby decreasing prompt neutron lifetime, nearly all fluctuation in flux shape finished prior to 0.001 seconds, as shown in Figure 40. When neutron velocity was multiplied by a factor of 0.9, the largest fluctuations in flux shape finished around 0.002 seconds, with continued settling out until ~0.005 seconds, shown in Figure 41. This demonstrates a clear relationship between the energy of neutrons and the time it takes for flux shape to settle out after rod motion. Over the time-frame considered, only the variations in the prompt neutrons could show such an effect on the flux shape.

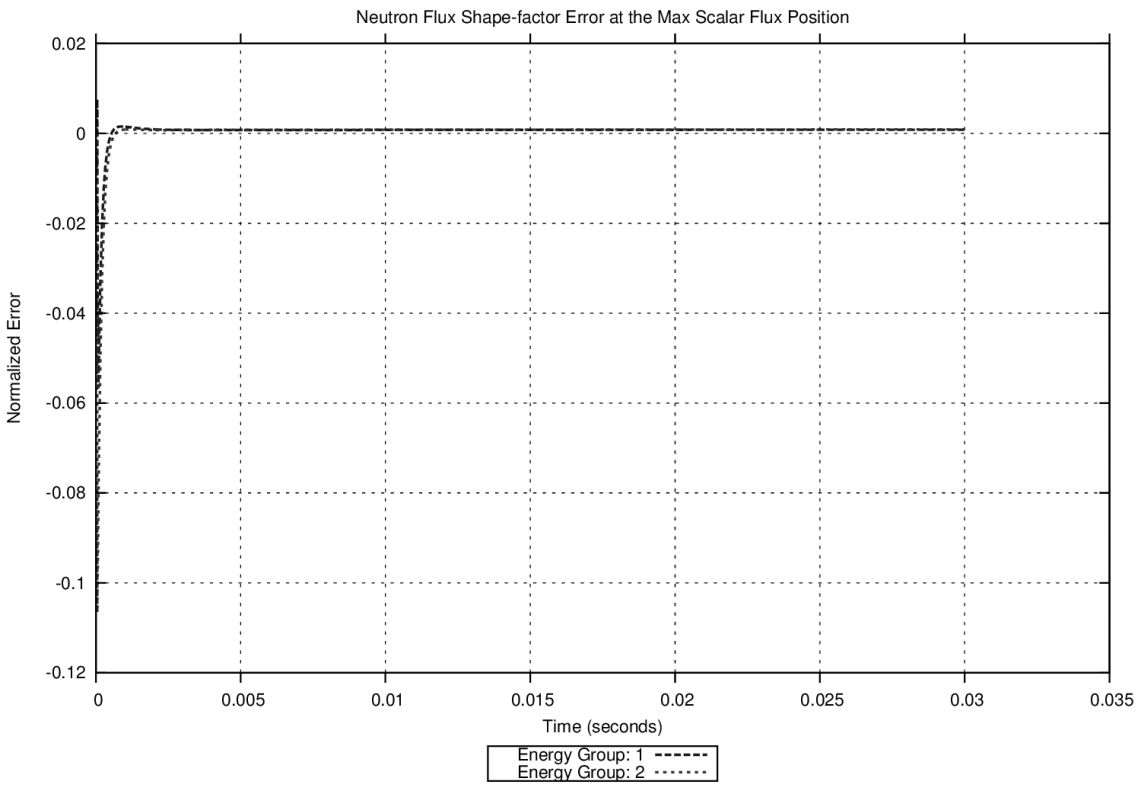

Figure 40: Hot-spot flux shape error, step insertion transient, normal beta values, 1.1 x neutron velocity

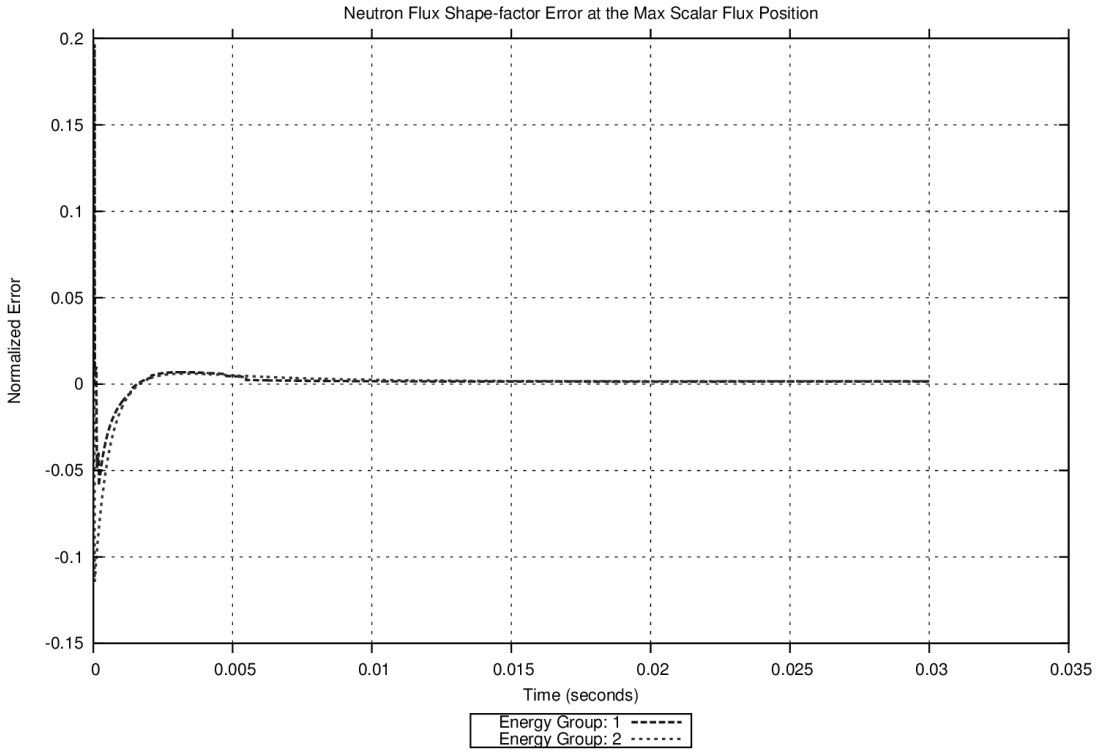

Figure 41: Hot-spot flux shape error, step insertion transient, normal beta values , 0.9 x neutron velocity

3.3.3 Shape-Factor Optimization

Further testing was performed to identify an ideal time period for the rapid insertion shape-factor production run. It was found, with suppressed betas of 0.0001, that a rapid insertion spanning 0.05 seconds with a time-step of 0.0005 was sufficient to reduce the RMS error in flux shape for the 2 second run from ~15% in Figure 32 to ~3% in Figure 42. In the 120 second run with suppressed betas, the RMS flux shape error was reduced from ~16% in Figure 36 to ~3% in Figure 43. The accuracy of the shape factors was found to not be significantly different in the 0.05 second run when the time-step was changed from 0.0001 seconds to 0.0005 seconds. The 0.05 second insertion run was redone with betas at normal values to verify that there was real improvement. It was found, with normal betas, that a rapid insertion spanning 0.05 seconds with a time-step of 0.0005 was sufficient to reduce the RMS error in flux shape for the 2 second run from ~10% in Figure 31 to ~1.2% in Figure 44. In the 120 second run with normal betas, the RMS flux shape error was reduced from ~16% in Figure 35 to ~7.5% in Figure 45. It is expected that the error in the 120 second case should be larger than the 2 second case with delayed neutrons and betas at normal values and effect, due to the increased change in DNP concentration in the longer transient. Figure 44 and Figure 45 demonstrate that this holds true, with a ~6% difference between them. The difference in error between the 2 second and 120 second transients with the 0.002 second rapid insertion set, shown in Figure 31 and Figure 35, was also ~6%. This indicates that roughly 9% of the RMS error when using the 0.002 second rapid insertion set could be attributed to prompt neutron transient effects.

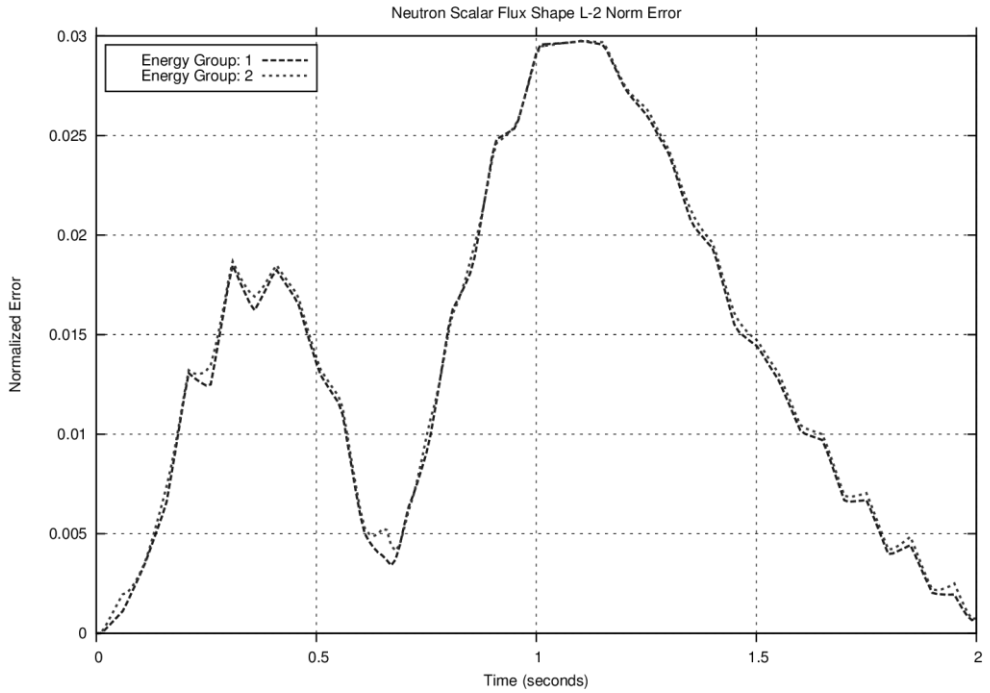

Figure 42: RMS flux shape error, 2 second transient, 0.0001 beta values, 0.05 second projection operator set.

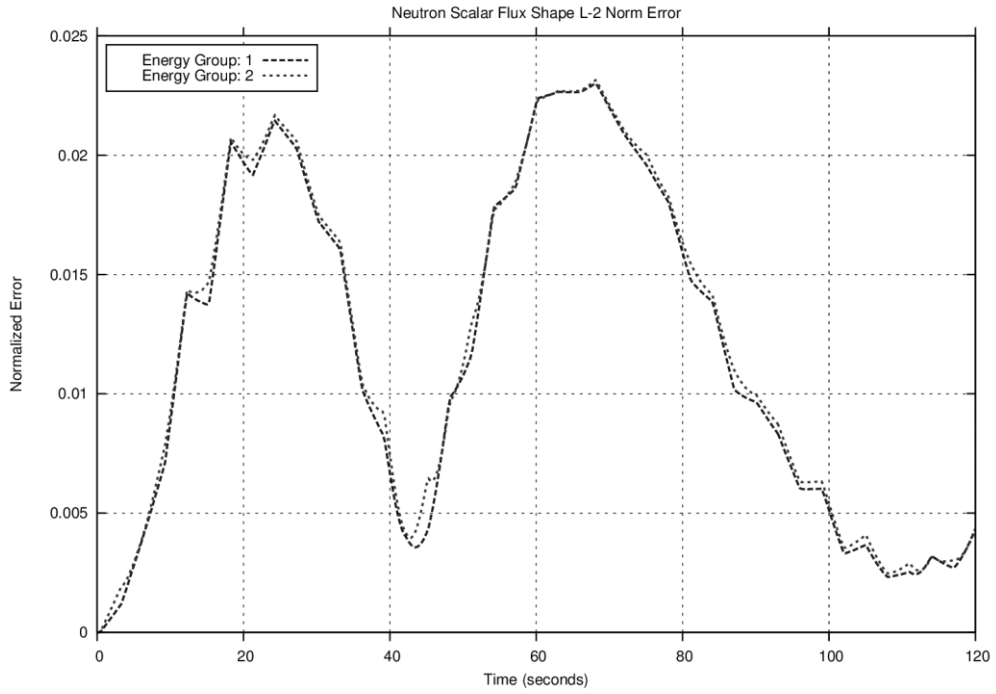

Figure 43: RMS flux shape error, 120 second transient, 0.0001 beta values, 0.05 second projection operator set.

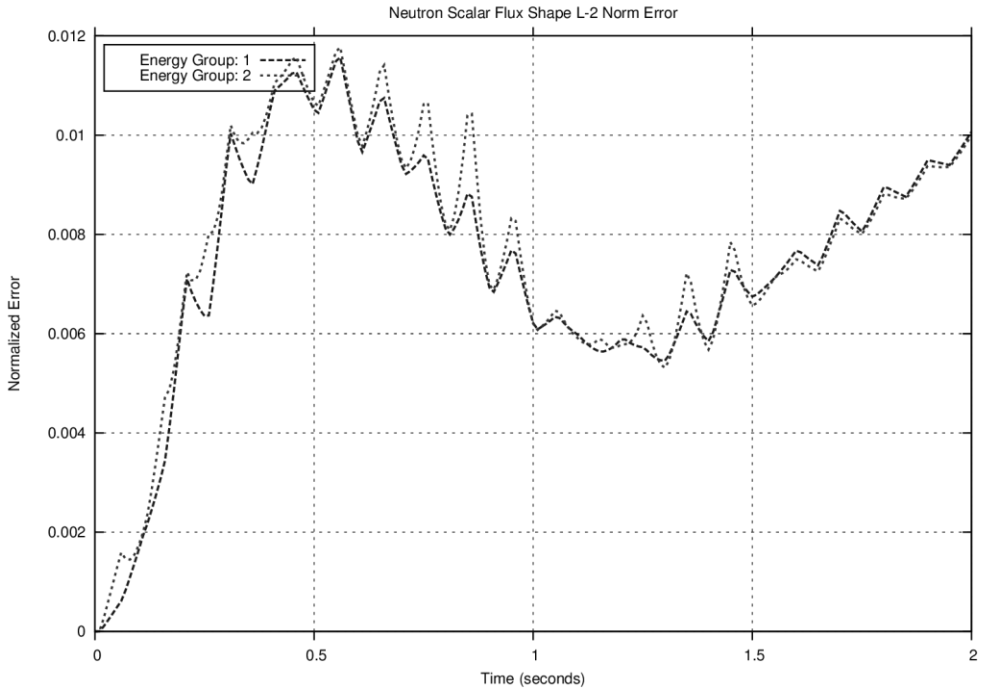

Figure 44: RMS flux shape error, 2 second transient, normal beta values, 0.05 second projection operator set.

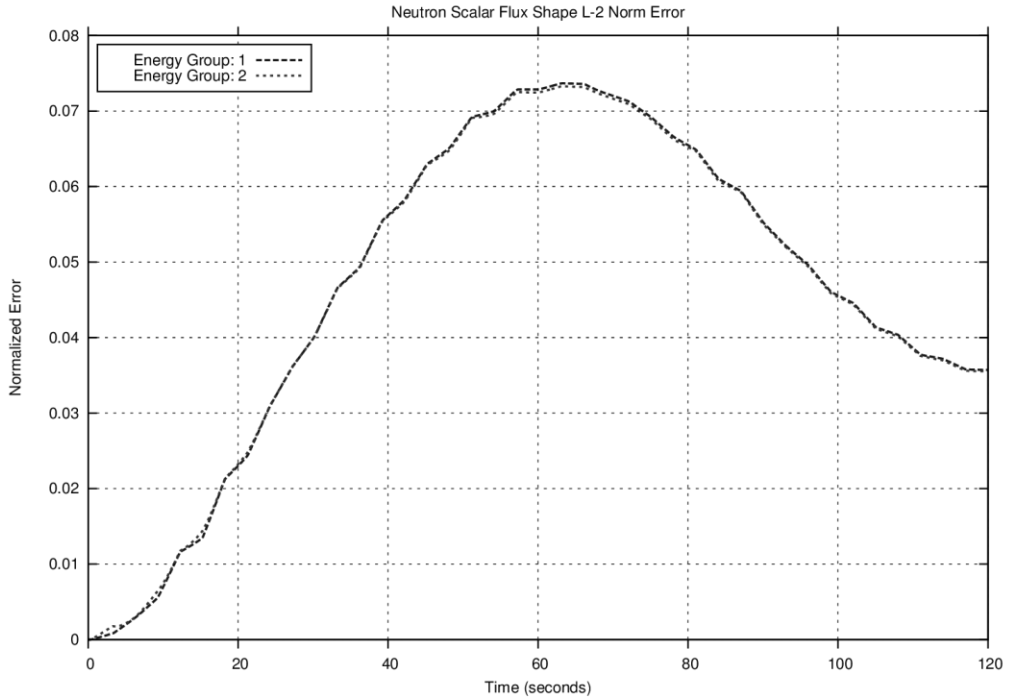

Figure 45: RMS flux shape error, 120 second transient, normal beta values, 0.05 second projection operator set.

With betas at normal values, comparing 2 second high-fidelity flux shape information to 120 second high-fidelity flux shape information, the RMS difference in flux shape is almost 7%, as shown in Figure 46. This suggests that further increases to the time-span of the projection operator set will provide little improvement to the low-fidelity model of any rod-insertion, and that the majority of any remaining error is indeed due to delayed neutrons.

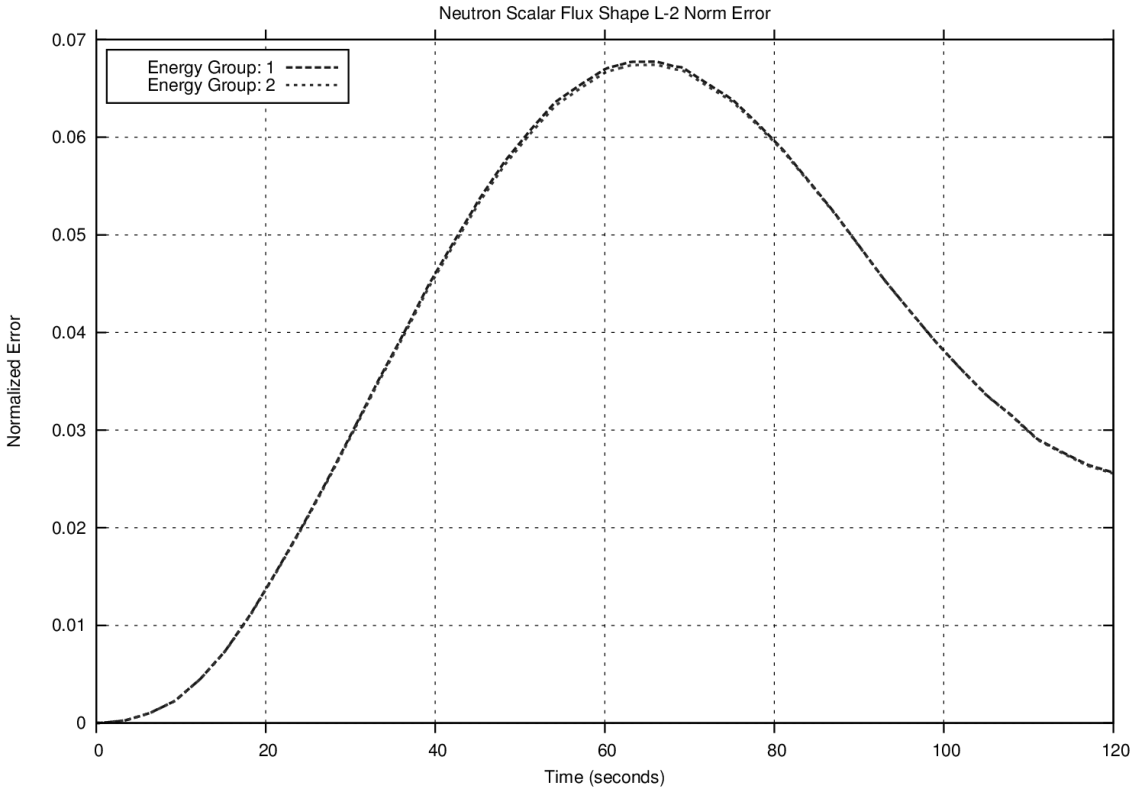

Figure 46: RMS flux shape error, 120 second transient, normal beta values, 2 second projection operator set.

The improvement seen in the shape-factors from changing the run time to 0.05 seconds for generating the projection operators carries over into the projected flux at all locations. For the 2 second transient, the absolute maximum flux error was reduced from ~65% in Figure 6 to ~16% in Figure 47. The absolute hot spot flux error was reduced from ~5% in Figure 7 to ~1.4% in Figure 48. The error in the two second transient is now less than a third of what it was with the original projection operator set, and in most areas the model is improved more than that. For the 120 second transient, the absolute maximum flux error was reduced from ~60% in Figure 49 to ~20% in Figure 50. The absolute hot spot flux error was reduced from ~7% in Figure 51 to ~4% in Figure 52. The error in the 120 second transient has been approximately halved. Once again, it is expected that the longer transient should show proportionately less improvement, due to the greater influence of delayed neutrons.

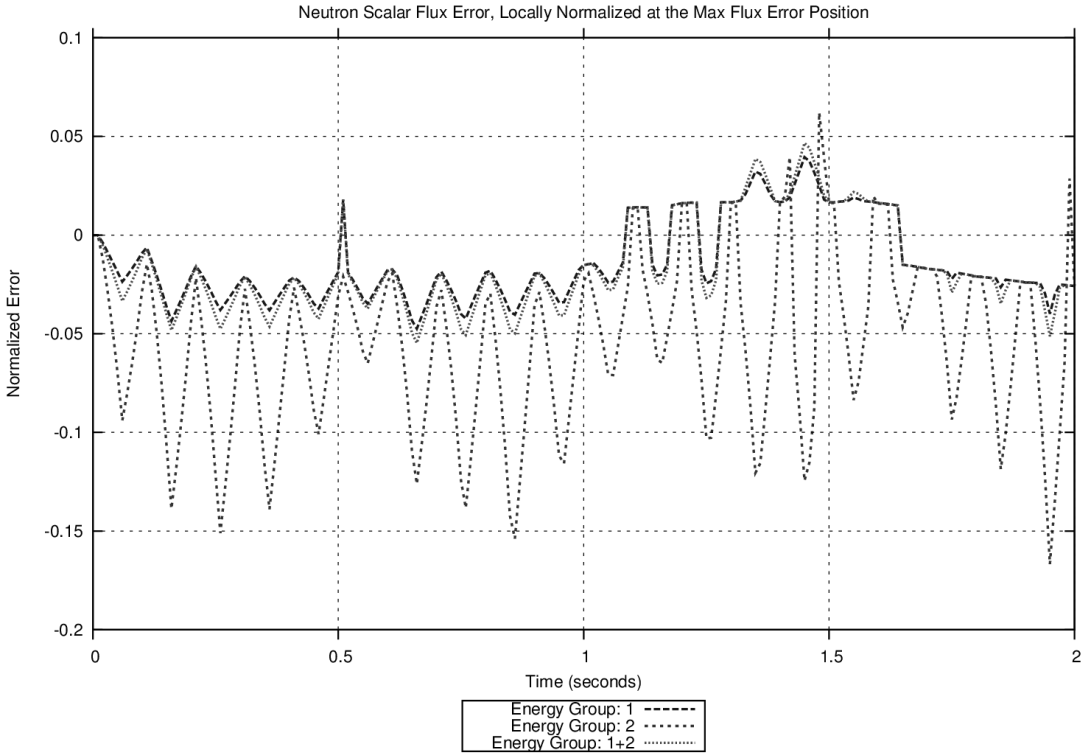

Figure 47: Maximum flux error, 2 second transient, normal beta values, 0.05 second projection operator set.

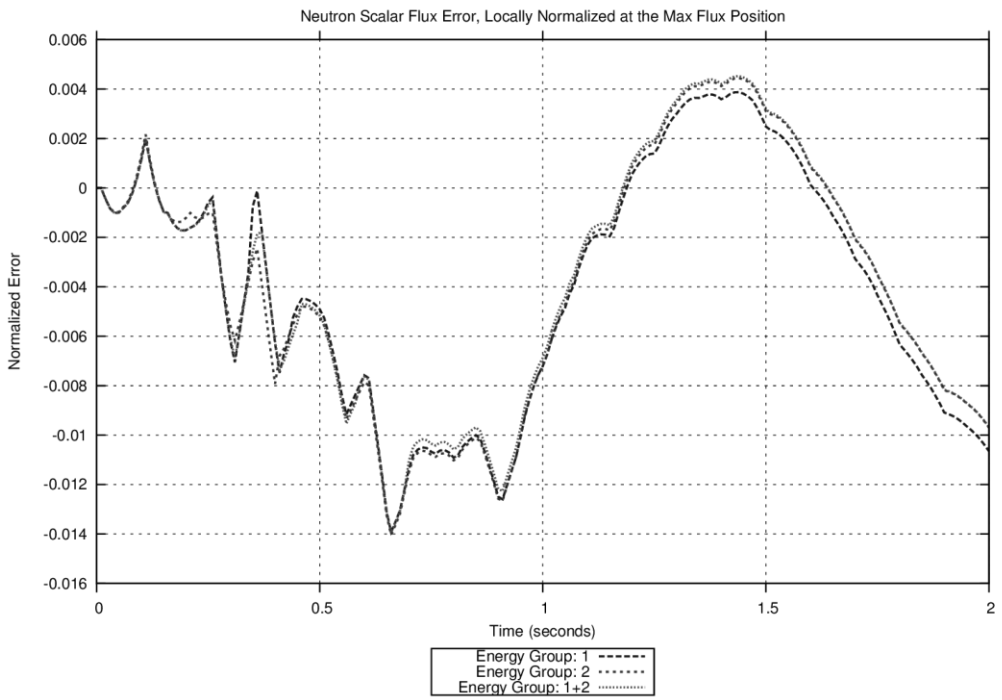

Figure 48: Hot-spot flux error, 2 second transient, normal beta values, 0.05 second projection operator set.

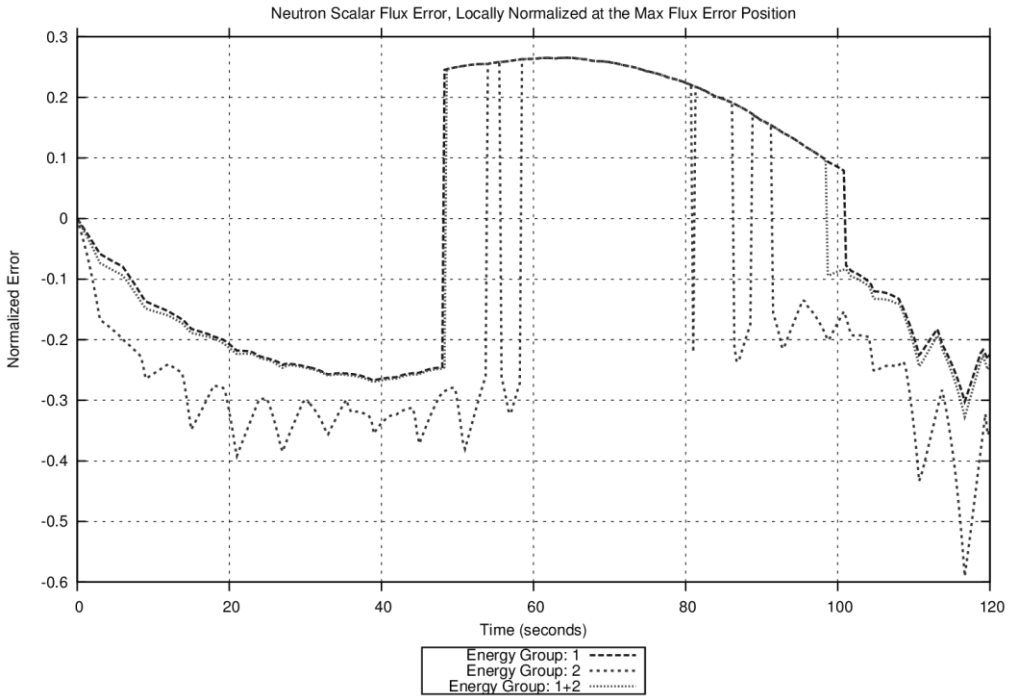

Figure 49: Maximum flux error, 120 second transient, normal beta values, 0.002 second projection operator set.

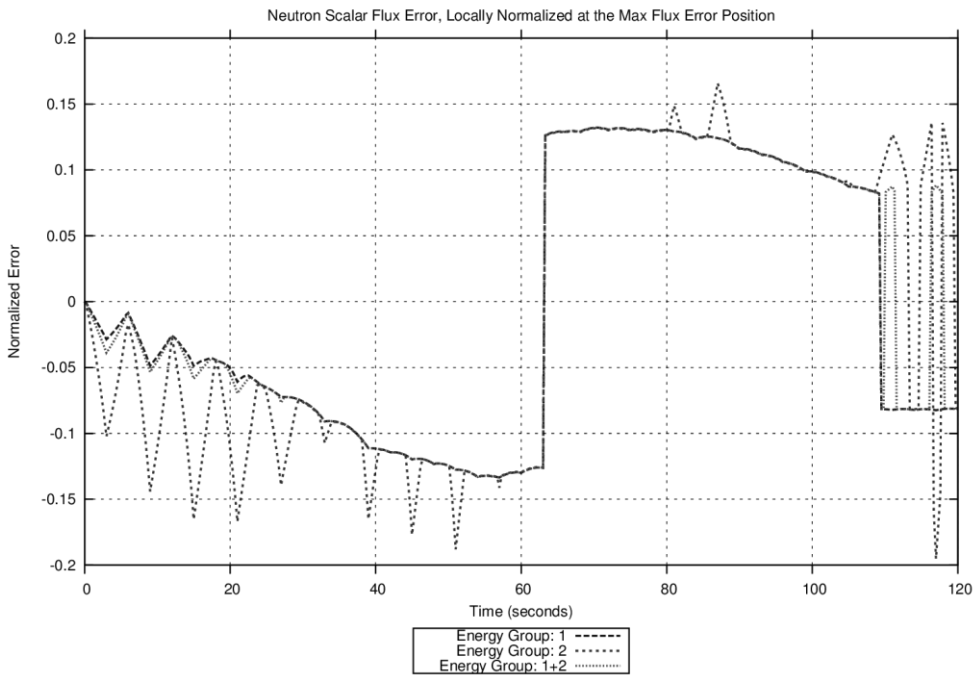

Figure 50: Maximum flux error, 120 second transient, normal beta values, 0.05 second projection operator set.

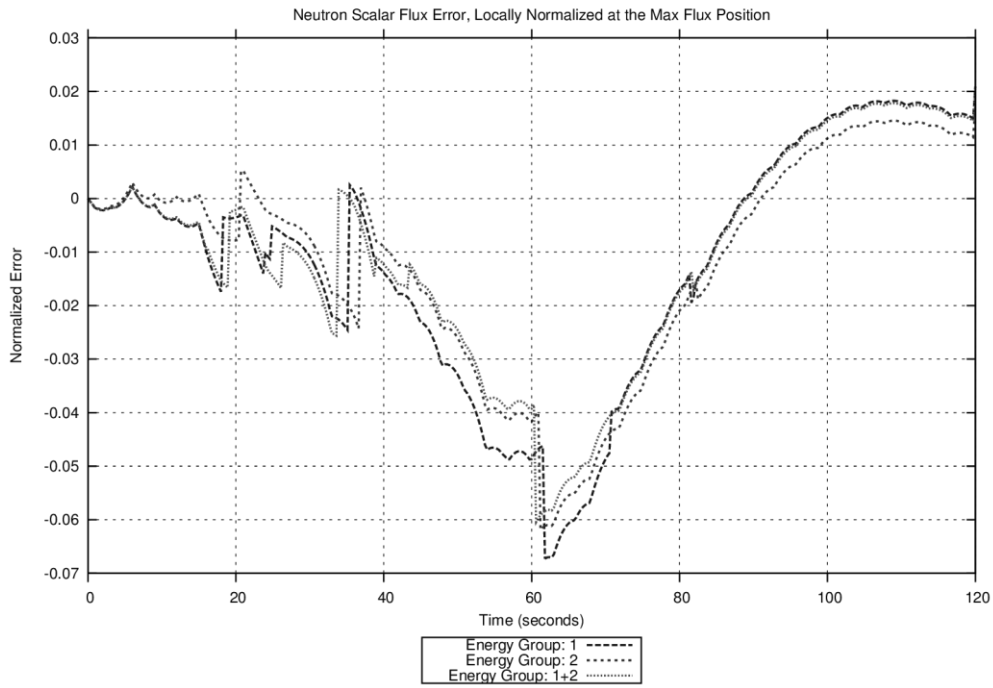

Figure 51: Hot-spot flux error, 120 second transient, normal beta values, 0.002 second projection operator set.

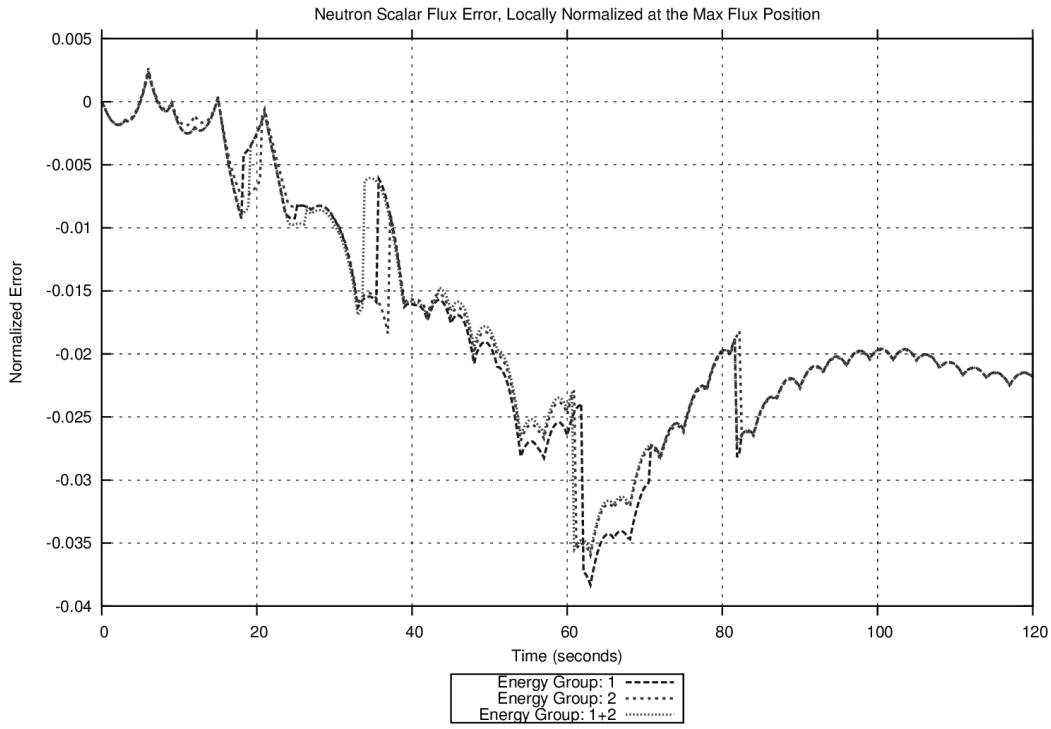

Figure 52: Hot-spot flux error, 120 second transient, normal beta values, 0.05 second projection operator set.

The rod withdrawal transient discussed originally in Section 3.2.4 is similarly improved when the projection operator production run is changed from a duration of 0.002 seconds to 0.05 seconds. Figure 92 - Figure 95 of the Appendix show the improved results.

A significant improvement in the accuracy of the low-fidelity model comes, then, from minimizing prompt neutron induced error in the projection operator set. With the improved rapid-insertion projection operator set, the steady state projection set is no longer comparable in its accuracy. Additionally, it is apparent that the error in the projected solution is very sensitive to changes in shape-factor generation algorithm. This is something to be careful of in any future permutations of the AMoR method.

3.3.4 Projection Operator Frequency

In the two second transient, it was observed that the variability or spikes in the maximum error became much more significant with the 0.05 second projection set than it had been with the 0.002 second projection set, as the size of the spikes largely remained constant while the average error magnitude was greatly reduced. In order to see if these spikes in flux error could be reduced or even removed, a test was run where the frequency of the projection operators was increased for the 0.05 second projection set. Changing the frequency of the projection operators from 20 to 50 equidistant snapshots over the course of the rapid-insertion reduced the maximum flux error from ~16% in Figure 47 to ~9% error in Figure 53 for the 2 second transient, and a reduction from ~20% in Figure 50 to ~14% in Figure 55 for the 120 second transient. This is another notable reduction in the maximum error. The maximum flux location experiences much less variability, however, as the same rapid spiky behavior is not present. As demonstrated by Figure 54 and Figure 56, the accuracy at the hot spot locations is not improved. Likewise, RMS flux error is minimally affected by the operator frequency increase. While the absolute improvement is the approximately the same between the transients, the longer transient shows proportionally less improvement than the 2 second transient. Optimization via increasing projection operator frequency will only be of importance if maximum error is used as a criteria, and is less important for longer transients due to its smaller relative effect. Presumably, after this additional modification to the projection operator set, the majority of all remaining error is in fact due to delayed neutrons effect on flux shape. As the flux solution has been improved, so has the DNP concentration solution. Figure 96 - Figure 99 in the Appendix show the DNP error metrics for the hybrid precursor solution after the projection operators have been optimized. Following the improvements introduced so far, it is expected that projection operator updates will not be needed as soon, if at all, in any given transient using this low-fidelity model, for a given desired accuracy.

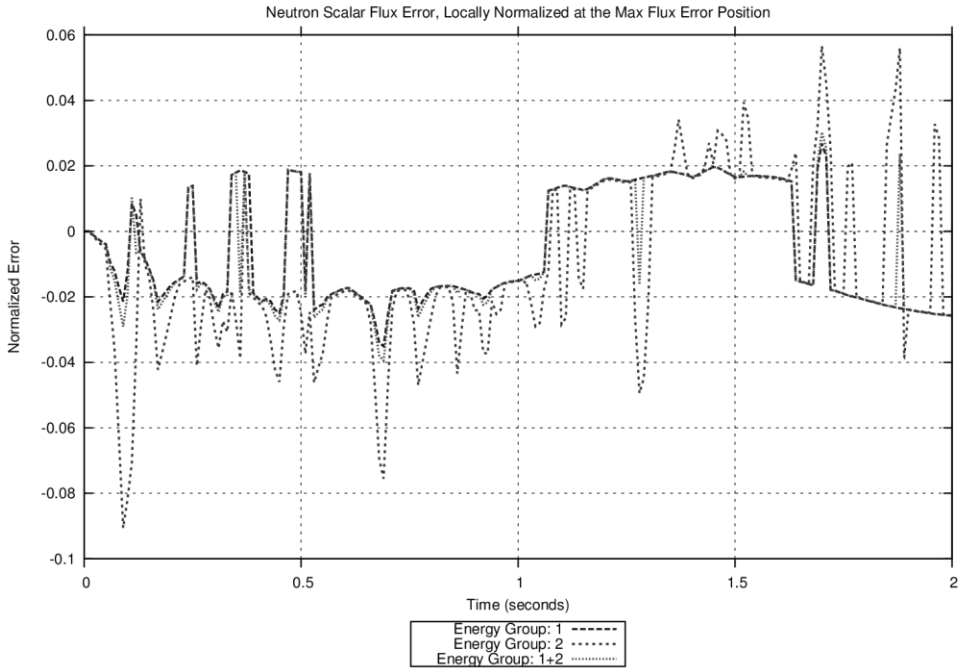

Figure 53: Maximum flux error, 2 second transient, normal beta values, high frequency 0.05 second projection operator set.

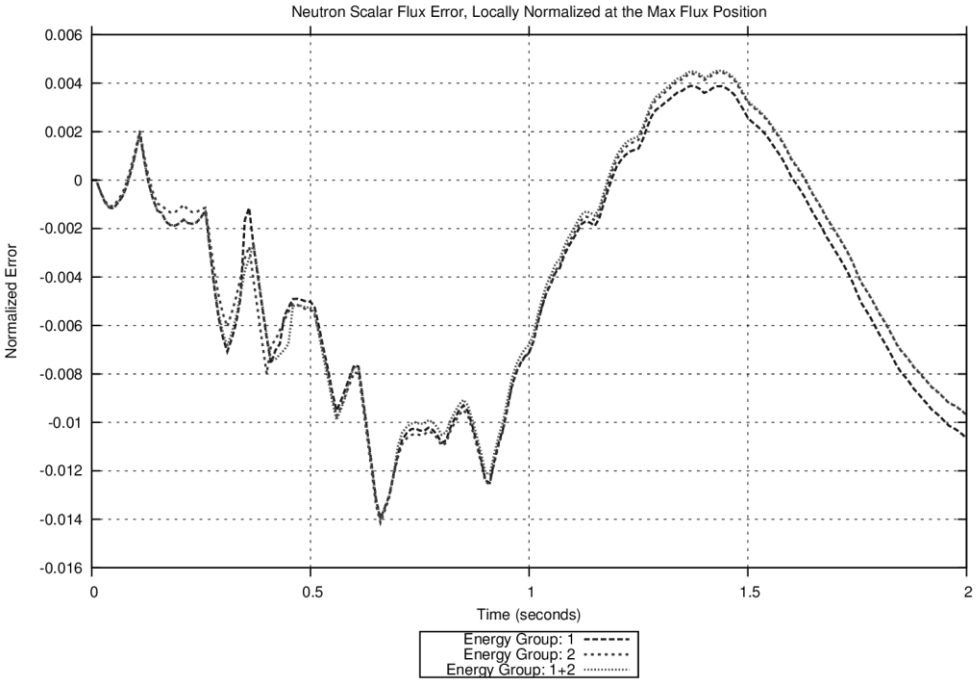

Figure 54: Hot-spot flux error, 2 second transient, normal beta values, high frequency 0.05 second projection operator set.

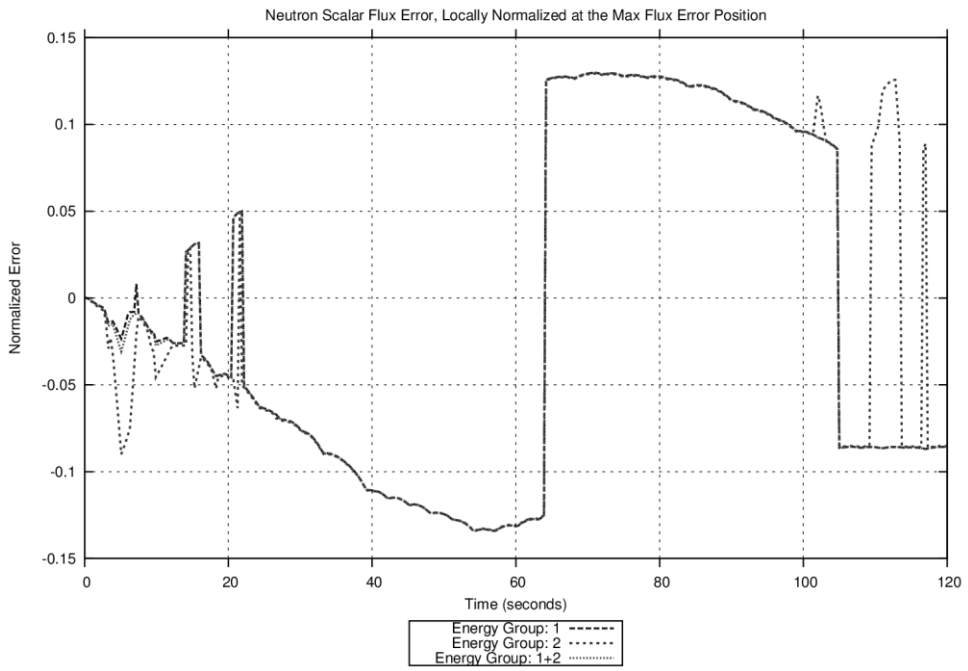

Figure 55: Maximum flux error, 120 second transient, normal beta values, high frequency 0.05 second projection operator set.

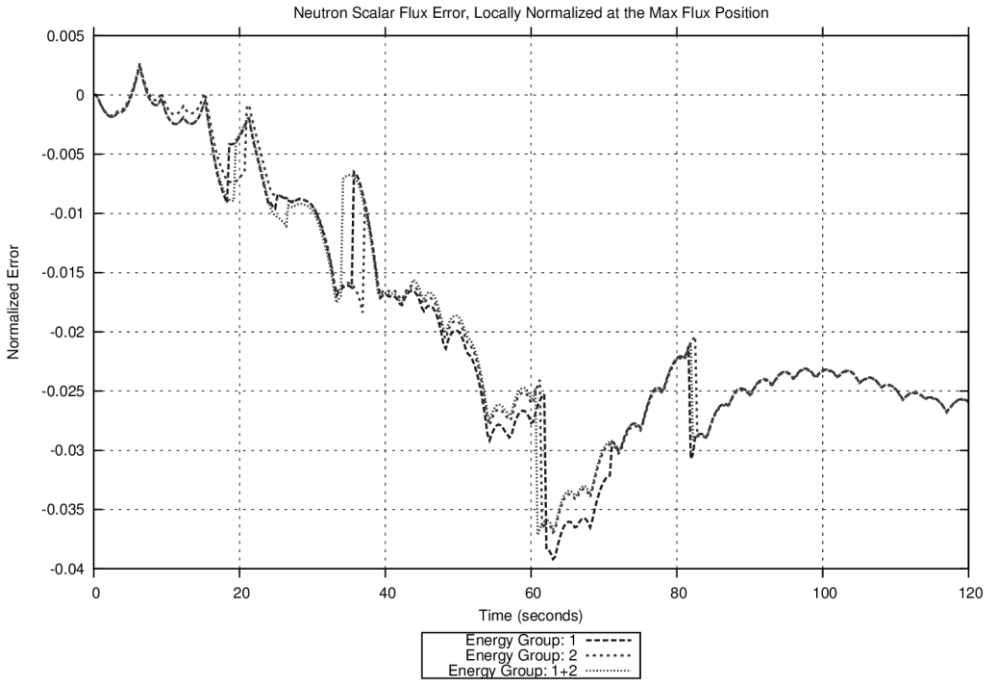

Figure 56: Hot-spot flux error, 120 second transient, normal beta values, high frequency 0.05 second projection operator set.

3.3.5 Active Switching Parameter Tests

With the improved set of projection operators, it was desired to examine the behavior under switching conditions. Representative updates were run for the 120 and 2 second cases with the update occurring halfway through the transient. The first half of the transient used the optimized set of projection operators demonstrated in Section 3.3.4. The initial examination looked at a comparison of RMS flux shape with the first half of the low-fidelity solution being from the 0.002 second projection operators set versus the 0.05 second projection operator set. The 2 second transient update used a time-step of 0.001 seconds for both the annealing and projection operator production portions of the restart. The 120 second transient update had a time-step of 0.01 seconds for both portions. The default setup provides 13 sets of projection operators for the remaining half of the rod insertion. Examining the results shown in Figure 57 - Figure 60, it is clear that the 2 second update did not have ideal restart parameters.

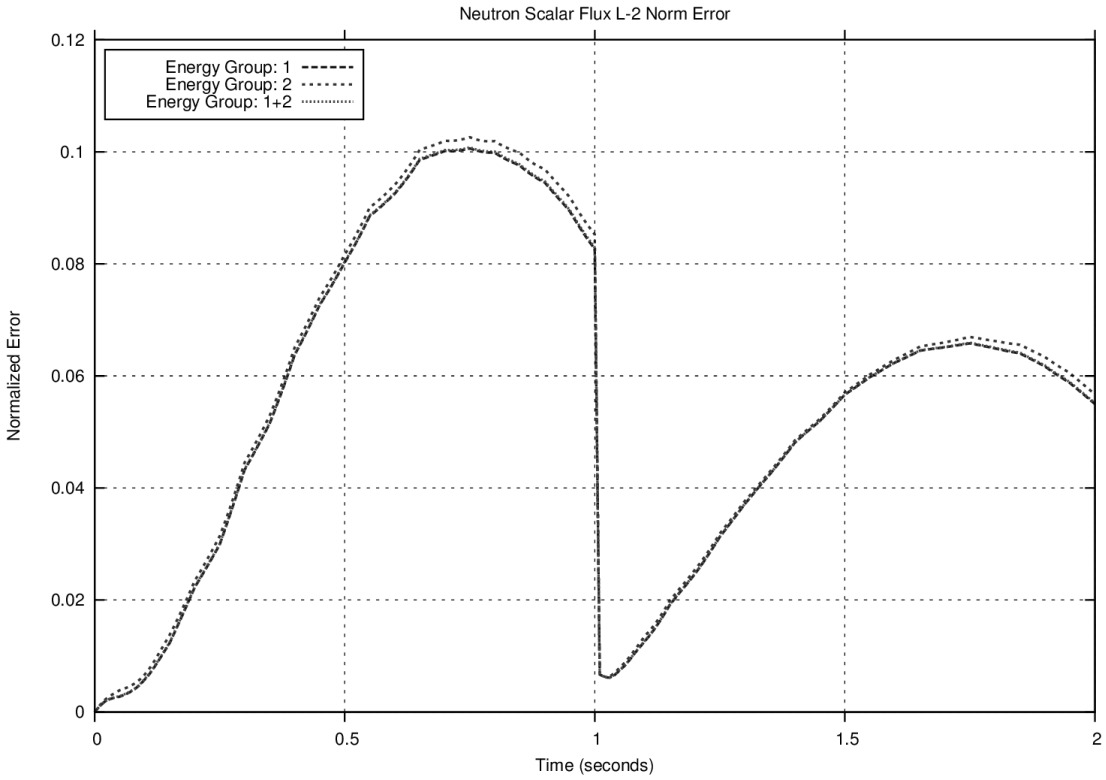

Figure 57: RMS flux error, 2 second transient, 0.002 second projection operator set, update at 1 second, original restart parameters: (0.001 second time-steps).

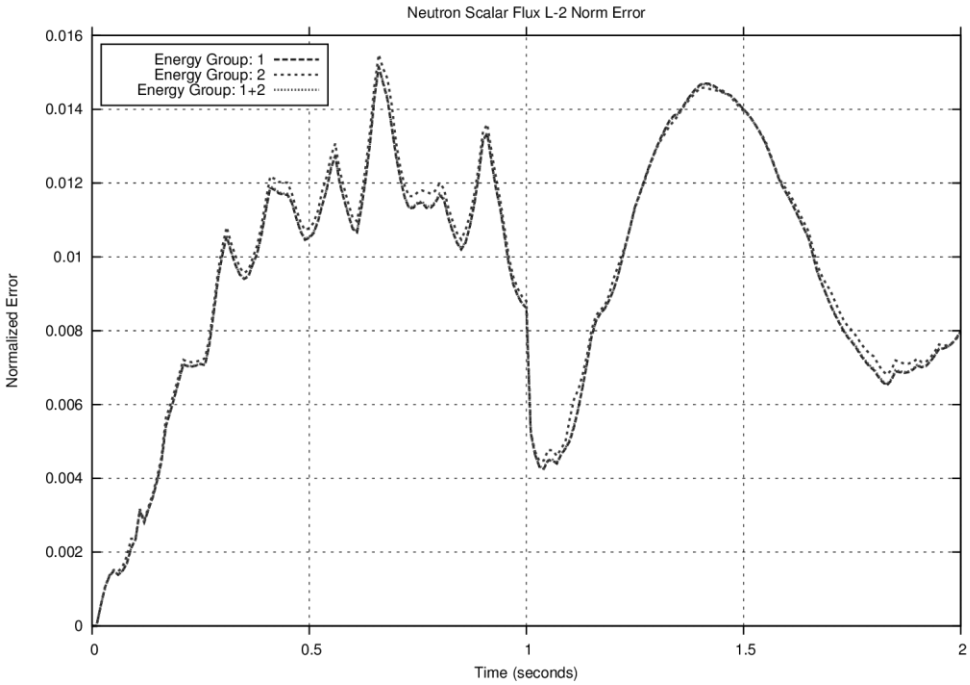

Figure 58: RMS flux error, 2 second transient, 0.05 second projection operator set, update at 1 second, original restart parameters: (0.001 second time-steps).

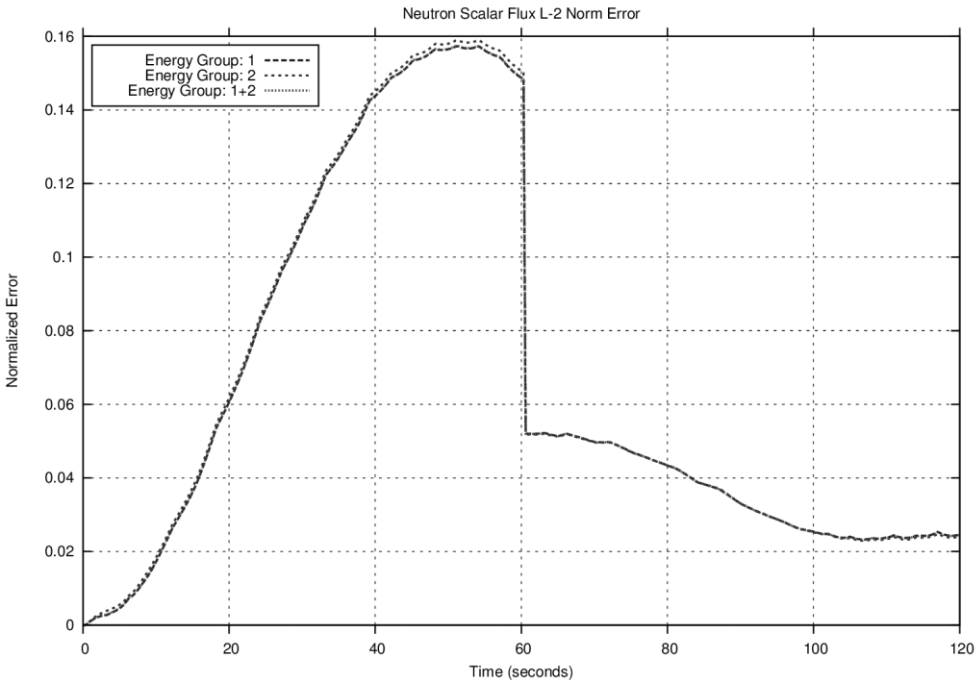

Figure 59: RMS flux error, 120 second transient, 0.002 second projection operator set, update at 60 seconds, original restart parameters: (0.01 second time-steps).

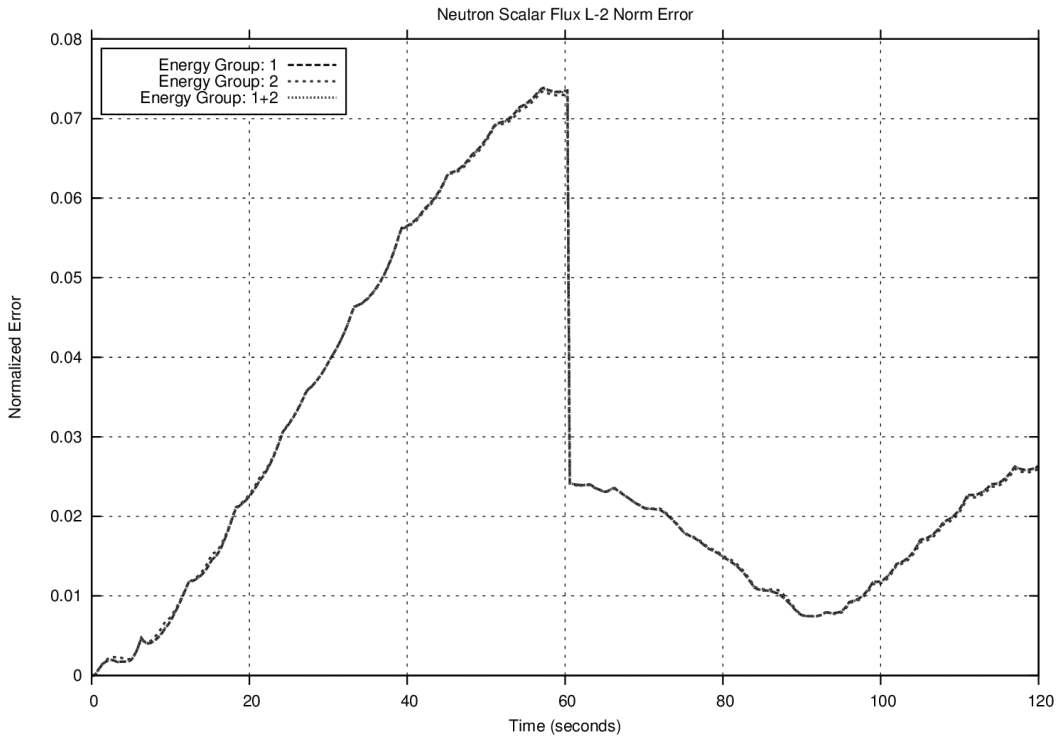

Figure 60: RMS flux error, 120 second transient, 0.05 second projection operator set, update at 60 seconds, original restart parameters: (0.01 second time-steps).

In order to reduce model error after the update, tests were run on several of the factors defining the restart transient to determine ideal values. It was decided to use the 120 second restart parameters as the base case for both the 2 second and 120 second restart parameter analyses, from which each parameter was varied in turn. Figure 61 shows the effect of using a time-step of 0.01 seconds instead of 0.001 seconds for annealing and production portions of the 2 second transient update. The annealing and projection operator production time-steps were individually tested at 0.005 and 0.05 seconds. Additional parameters tested were increasing the number of steps back in the low-fidelity transient history where the annealing process started from 2 to 3, and doubling the number or frequency of snapshots produced following the update. All tests were performed using the 0.05 second projection operator set prior to the update. In addition to examining the RMS flux error, the CPU run-time of the NESTLE restart was used to determine the relative computational cost of each parameter modification.

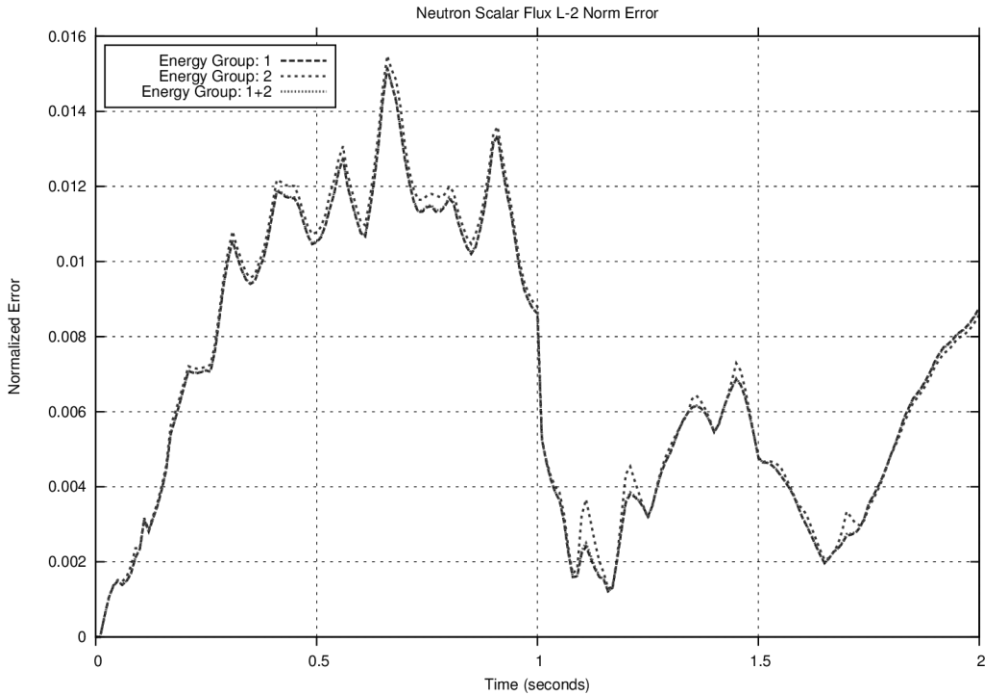

Figure 61: RMS flux error, 2 second transient, update at 1 second, 0.01 time-step for annealing and operator production.

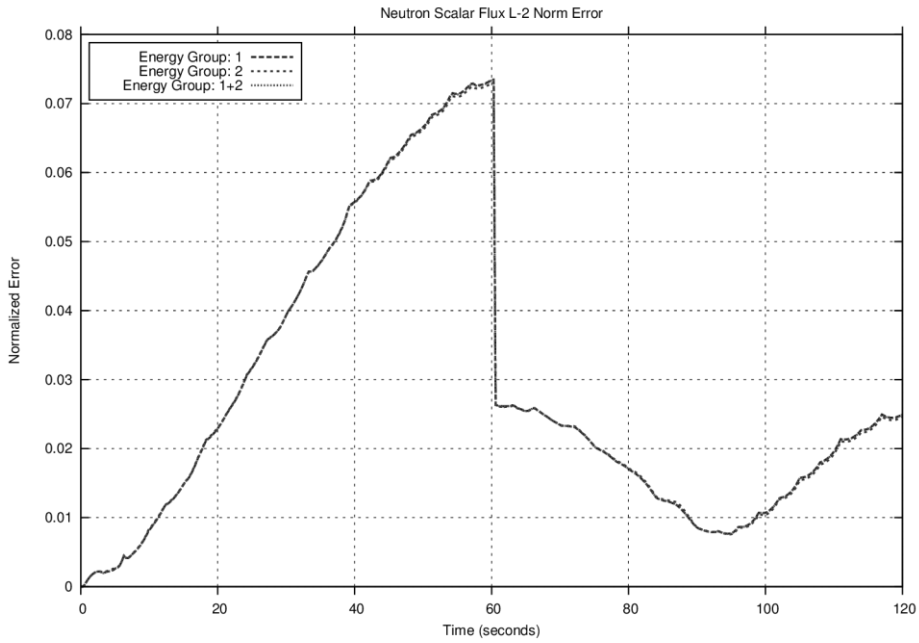

Figure 62: RMS flux error, 120 second transient, update at 60 seconds, 0.05 second annealing time-step.

Results from the annealing time-step tests showed no difference in error reduction with a shorter time-step, though it caused a ~30-147% increase in CPU time. The longer annealing time-step saved ~10% CPU time, but provided slightly less error reduction immediately following the update, as seen in Figure 62 compared to Figure 60 for the 120 second transient update. There is therefore no motivation to shorten the annealing time-step from 0.01 seconds and little motivation to lengthen it.

Changes to the projection operator production time-step initially appeared inconsequential in the tested range. CPU time varied minimally, and the range of time-steps, 0.005-0.05 seconds, caused minimal change in the error following the update. In order to reproduce the error seen in Figure 58, the time-step was shortened further for the 2 second transient; this generated more interesting effects. In Figure 63, with a 0.001 second projection operator production time-step, the error seen in Figure 58 has been entirely reproduced. This suggests that the entirety of the extraneous error after the update is caused by having too short a time-step for projection operator production. Figure 64, with a 0.002 second production time-step, still shows slightly more error than Figure 61 after the update. Projection operator production time-steps 0.005 seconds or greater provided no further decrease in error. This fits with the shape-factor errors caused by prompt neutron effects as discussed in Section 3.3.1. It is important, therefore, to ensure that the projection operator production time-step does not become shorter than ~0.005 seconds with this setup, if extraneous error is to be minimized.

Increasing the number of time steps back from 2 to 3 showed a very small improvement in error reduction in the 120 second test, and no change in error reduction in the 2 second test. Increasing the number of time steps back increased CPU time by ~6-11%. This leaves insufficient motivation to retain the increase in number of time steps back.

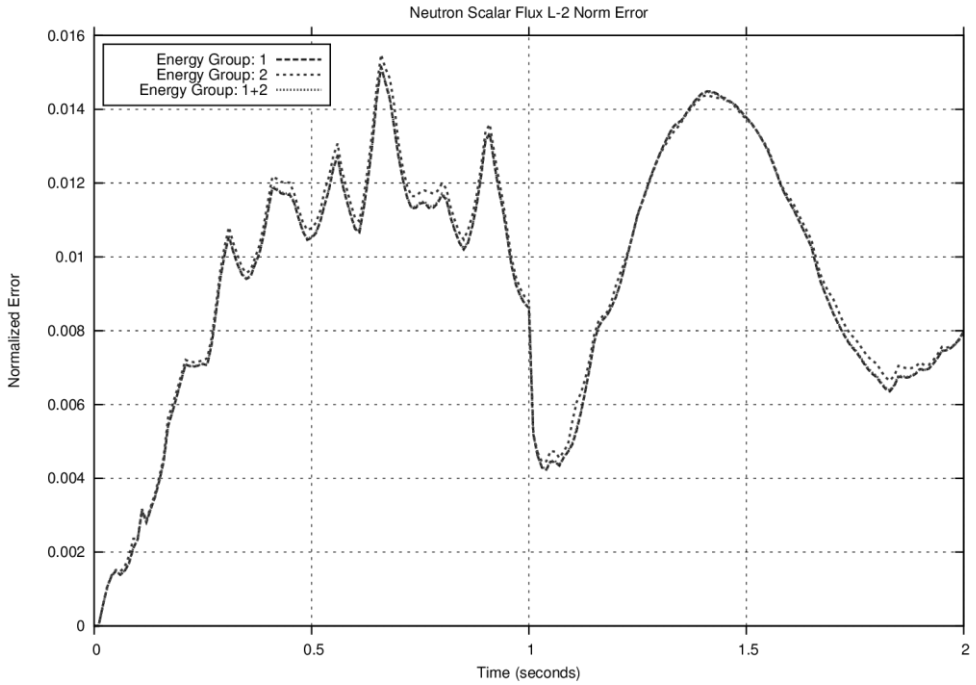

Figure 63: RMS flux error, 2 second transient, update at 1 second, 0.001 second operator production time-step

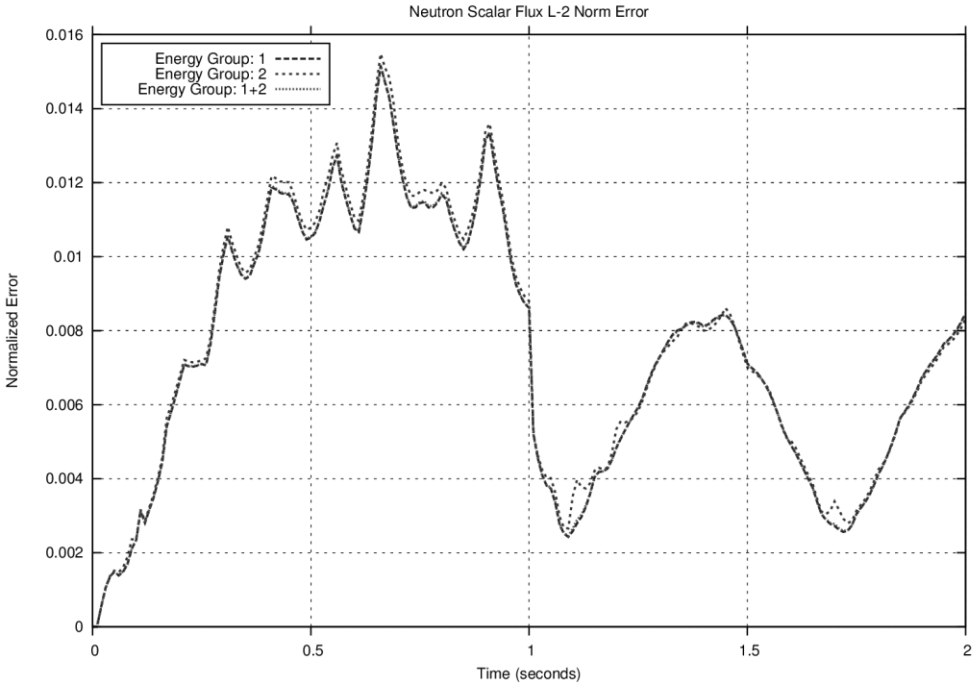

Figure 64: RMS flux error, 2 second transient, update at 1 second, 0.002 second operator production time-step.

The last restart parameter tested was the number or frequency of projection operators following the update. As seen in Figure 65, doubling the frequency of the projection operators does not significantly change the RMS flux error for the 2 second transient. The RMS flux error for the 120 second transient did not change noticeably at all. In accordance with the results shown in Section 3.3.4, however, the maximum flux error does change significantly when the frequency of projection operators is changed. Comparing Figure 66 to Figure 67 shows the effect on the 2 second transient, and comparing Figure 68 to Figure 69 shows the effect on the 120 second transient. Once again, the maximum flux error is significantly reduced for the 2 second transient. Notably, the maximum flux error following the update for the 120 second transient is also significantly reduced. In agreement with the results in 3.3.4, the hot spot flux error was unaffected by changing the frequency of the operators after the update.

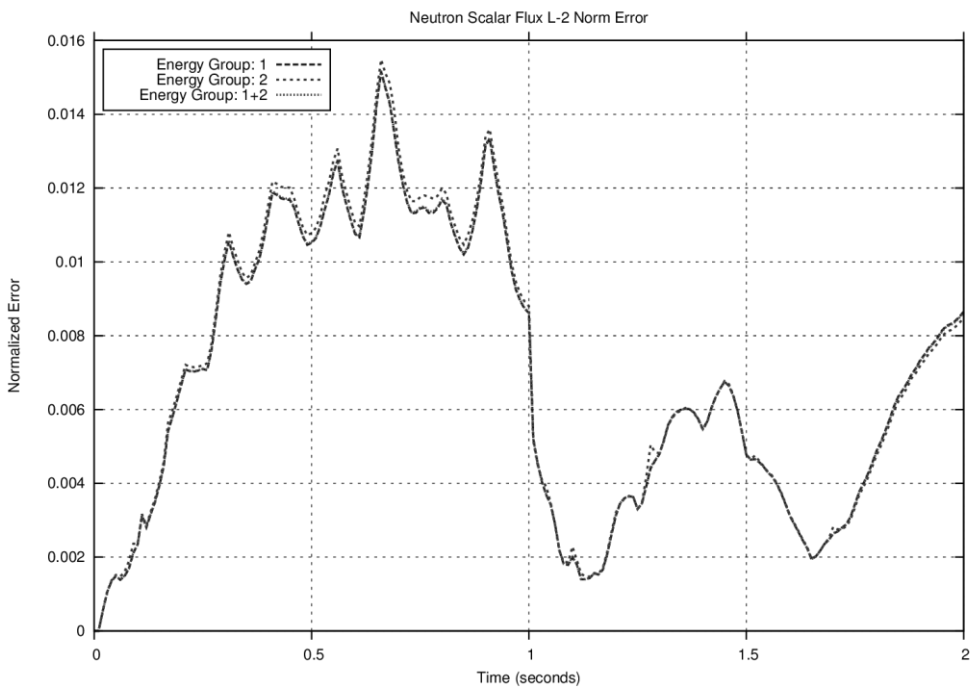

Figure 65: RMS flux error, 2 second transient, update at 1 second, doubled projection operator frequency.

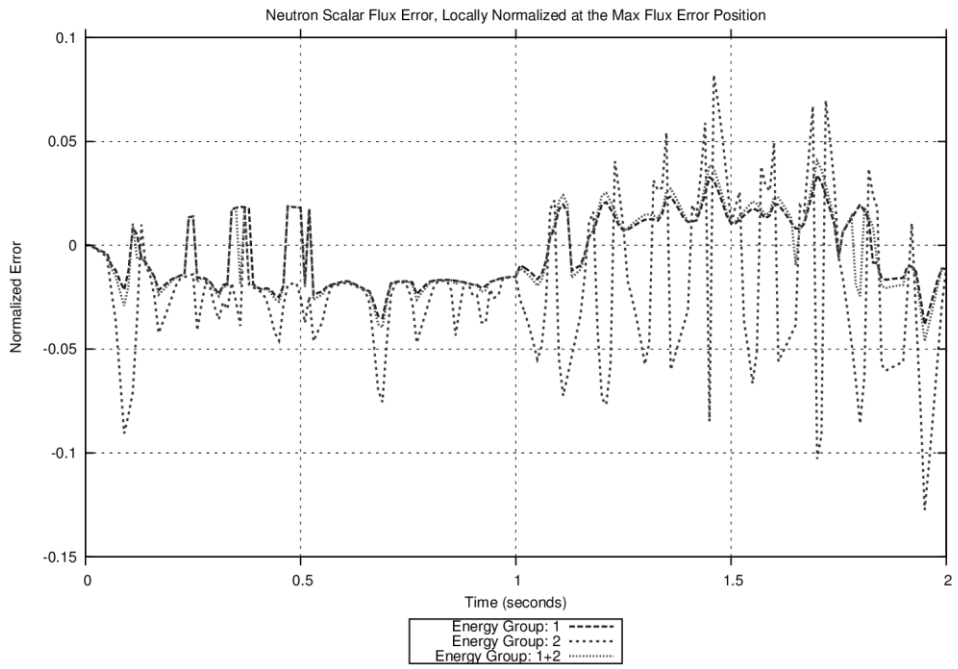

Figure 66: Maximum flux error, 2 second transient, update at 1 second, original projection operator frequency.

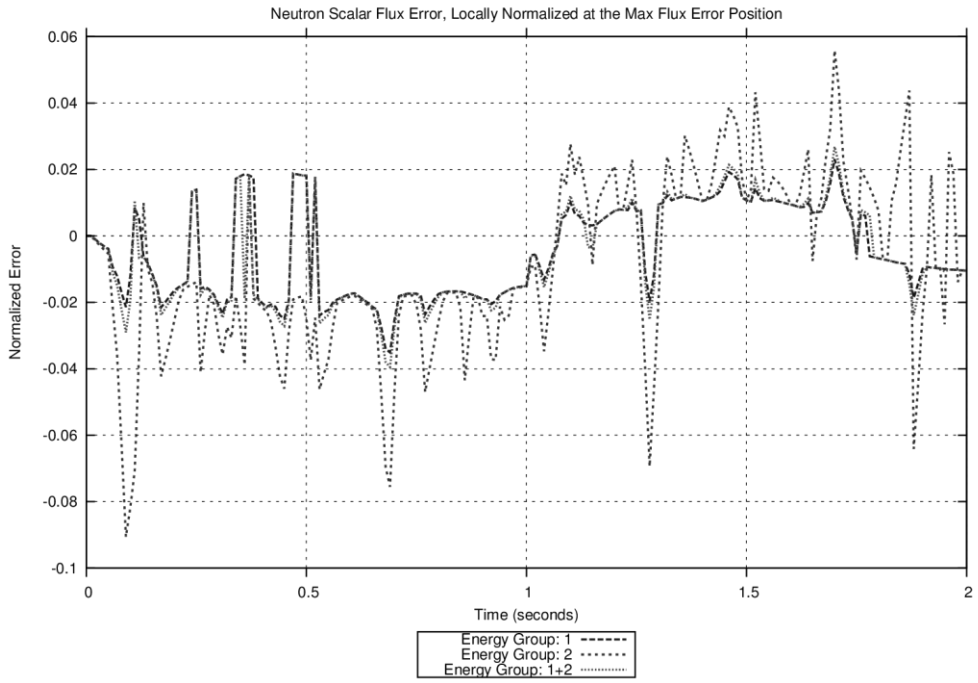

Figure 67: Maximum flux error, 2 second transient, update at 1 second, doubled projection operator frequency.

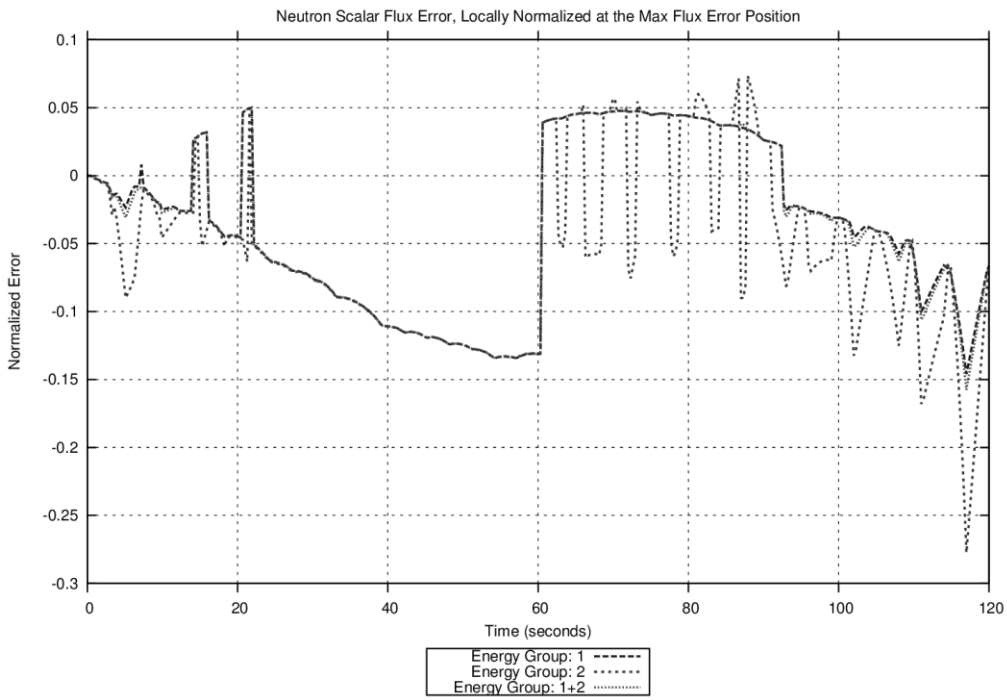

Figure 68: Maximum flux error, 120 second transient, update at 1 second, original projection operator frequency.

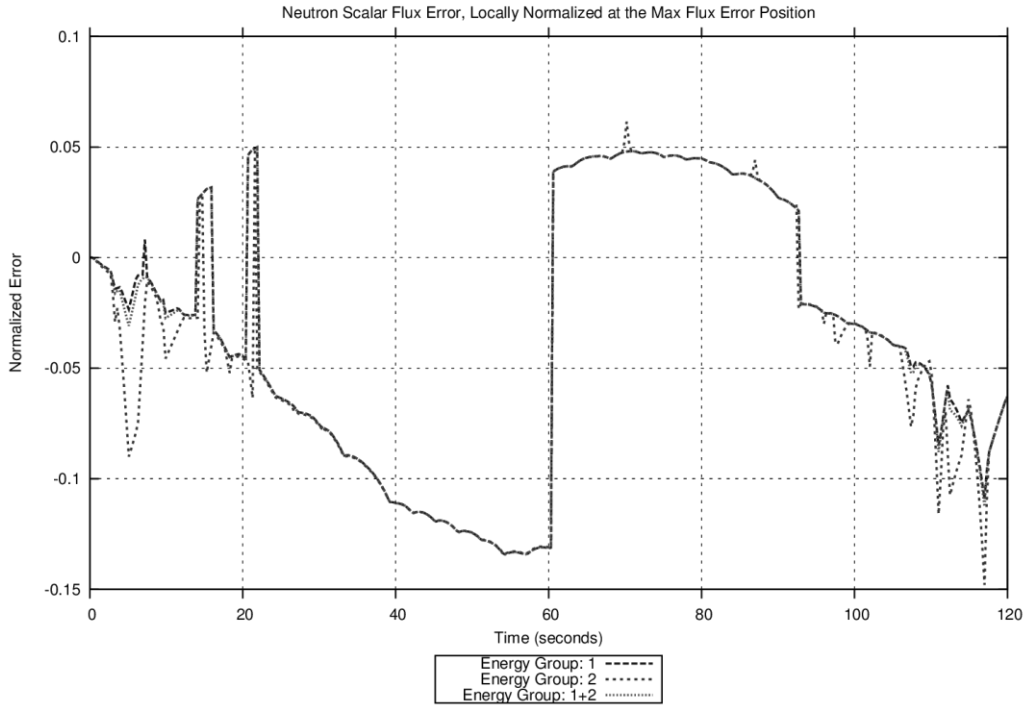

Figure 69: Maximum flux error, 120 second transient, update at 1 second, doubled projection operator frequency.

The restart parameter sensitivity analysis revealed several important details. The annealing time-step may be lengthened to reduce CPU cost, but provides minimal benefit to modify. While modifying the projection operator production time-step has minimal effect on accuracy or CPU cost, it is important that it not be too short in order to avoid introducing prompt neutron transient error. Increasing the number of steps back in the transient history that are solved in the high-fidelity annealing process provides no benefit and comes with a significant cost. Finally, if accuracy in the maximum flux error locations is desired, increased number of projection operators is a significant factor both before and after transient updates.

The error in the shape-factors and the flux was reduced by over 50% just by selecting a better timescale for the projection operator production run and removing prompt neutron transient error. While the maximum error values may be reduced by using more frequent shape-factors to minimize interpolation error, this has negligible effect on the maximum flux, or hot-spot, locations. Increasing the frequency of the shape factors is therefore only of significant interest when using all errors as potential update triggers. With the optimized projection operators before and after switching to the high-fidelity solution and back, the model is significantly improved. This implies that specified accuracy levels could be maintained with fewer required updates. Further decrease in error may be possible via analysis of delayed neutron behavior, assuming that the short-term prompt neutron induced errors are now minimized.

3.3.6 Delayed Neutron Effect Analysis

Several attempts were made to find a valid method to directly evaluate the contribution of precursor behavior to the flux distribution. This was initially hindered by the fact that the difference between the projection operator flux shape-factors and the true flux shape was not due solely to delayed neutron behavior. Subsequent to developing the improved shape-factors the idea was revisited.

With the original and with the optimized shape-factors, the radial and axial distributions of shape-factor error were examined for clues as to what might be contributing to the error. All flux distributions were examined using neutron energy group 2 flux shape-factors, as energy group 1 was determined to have comparable distribution and energy group 2 represents the largest error. Additionally, energy group 2 is most directly associated with the power distribution. The shape-factors were examined using 3-D plots of radial flux shape at various axial heights in the core. The horizontal axes are x and y node numbers, and the vertical axis is core-average normalized flux shape or the difference between two specified core-averaged flux shapes. Figure 70 show flux shapes with control rods half-way inserted during the 2 second transient. Visually, the differences in flux shape between the 2 second and 120 second transient, and the rapid insertion transients are difficult to detect.

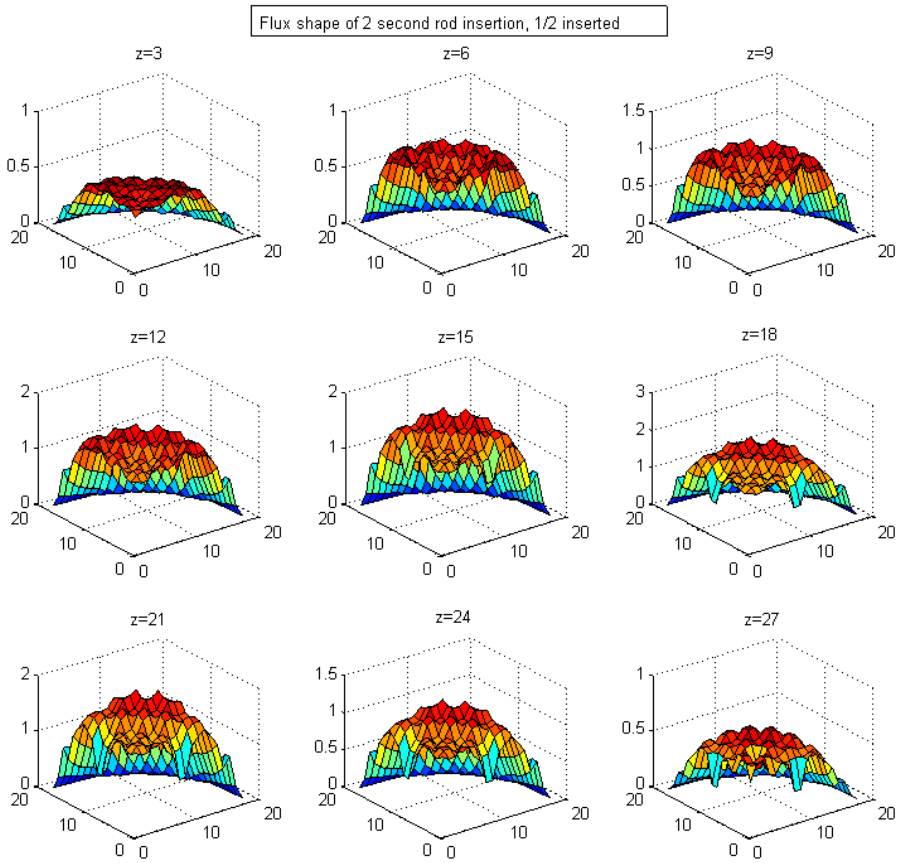

Figure 70: Flux shape, 2 second transient, rods ½ inserted.

Figure 71-Figure 74 show the normalized error in the flux shapes with the rods 4/5ths inserted. In each case, the error is normalized to the high-fidelity flux shape.

$$\varepsilon_{1,flux\cdot shape,(g=2),m} = \frac{S_{2,m}^{(\phi)}(t) - \tilde{S}_{2,m}^{(\phi)}(t)}{S_{2,m}^{(\phi)}(t)} \tag{3.1}$$

The location (0,0) on the graphs represents the center of the core. The control rods in use for the test cases are split along the horizontal axes and located at nodes (8-9,1) and (1,8-9) on the quarter core slice modeled. With locally normalized flux shape error there were noticeable spikes around the edges, in non-fueled regions of the core. A filter was applied to the flux shape errors to remove values representing non-fueled regions, as these regions provide no value to the model comparison or results in this study.

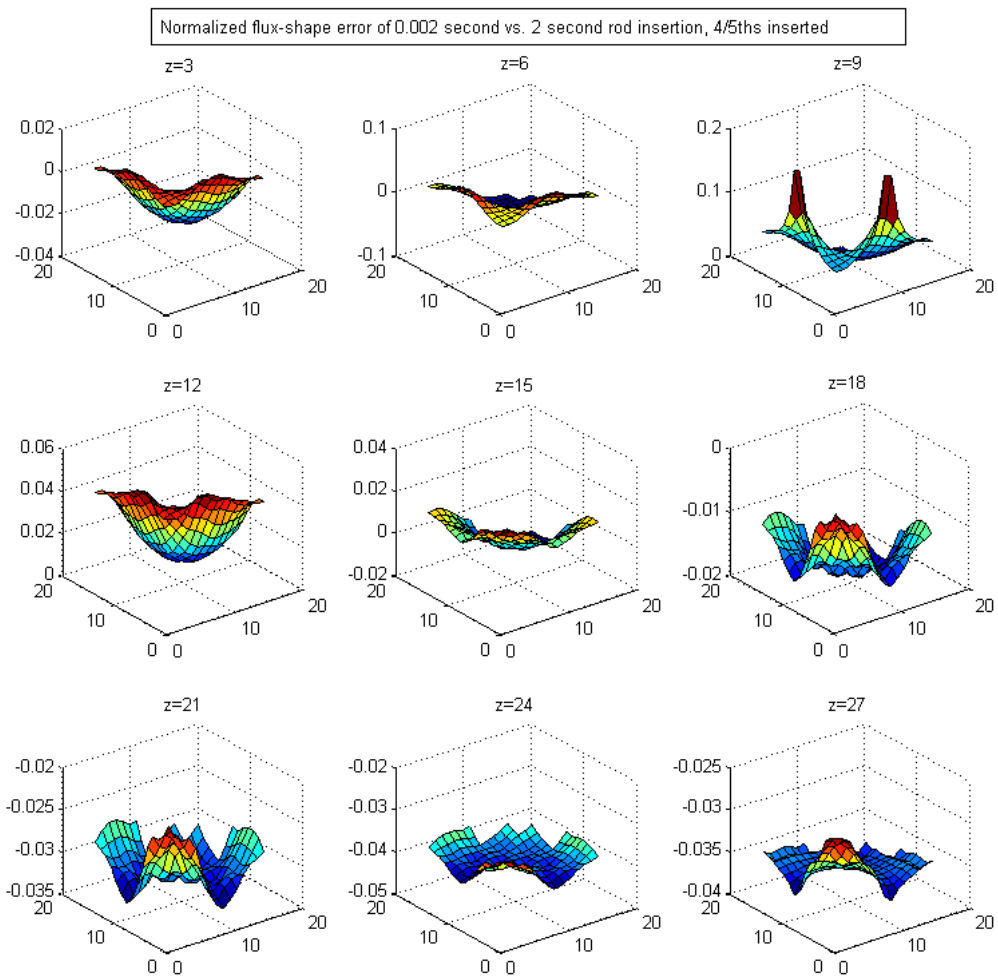

Figure 71: Normalized flux shape error, 2 second transient, 0.002 lo-fi, rods 4/5 inserted.

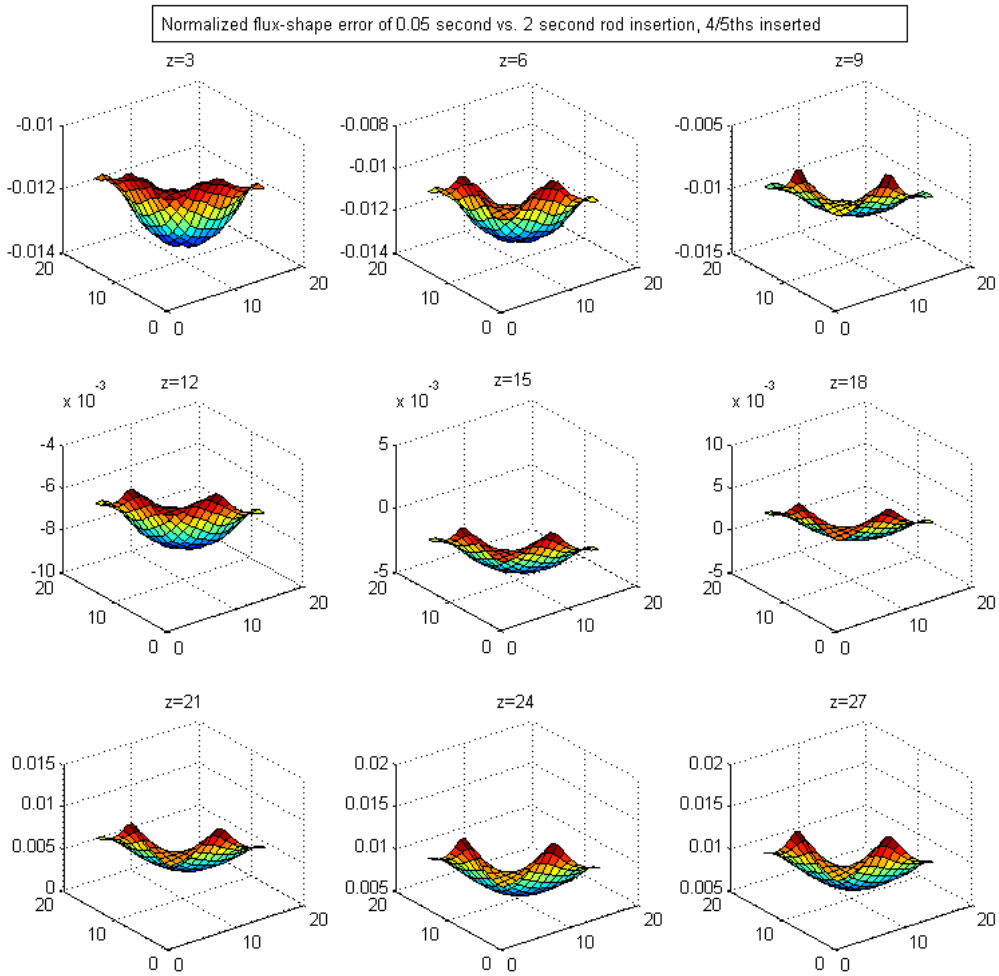

Figure 72: Normalized flux shape error, 2 second transient, 0.05 lo-fi, rods 4/5 inserted.

The largest normalized flux shape error is at the rod tip. Radially, the error is clearly dependent on distance from the control rods. Axially, the flux shape error showed a distinct difference in axial flux shift for a given rod insertion predicted by the rapid insertion vs. the true transients. With the rods 4/5 inserted in the two second transient, the 0.002 second low-fidelity transient error is larger than the 0.05 second error; additionally, it is quite clear that there are different error behaviors in the two sets of low fidelity flux shapes.

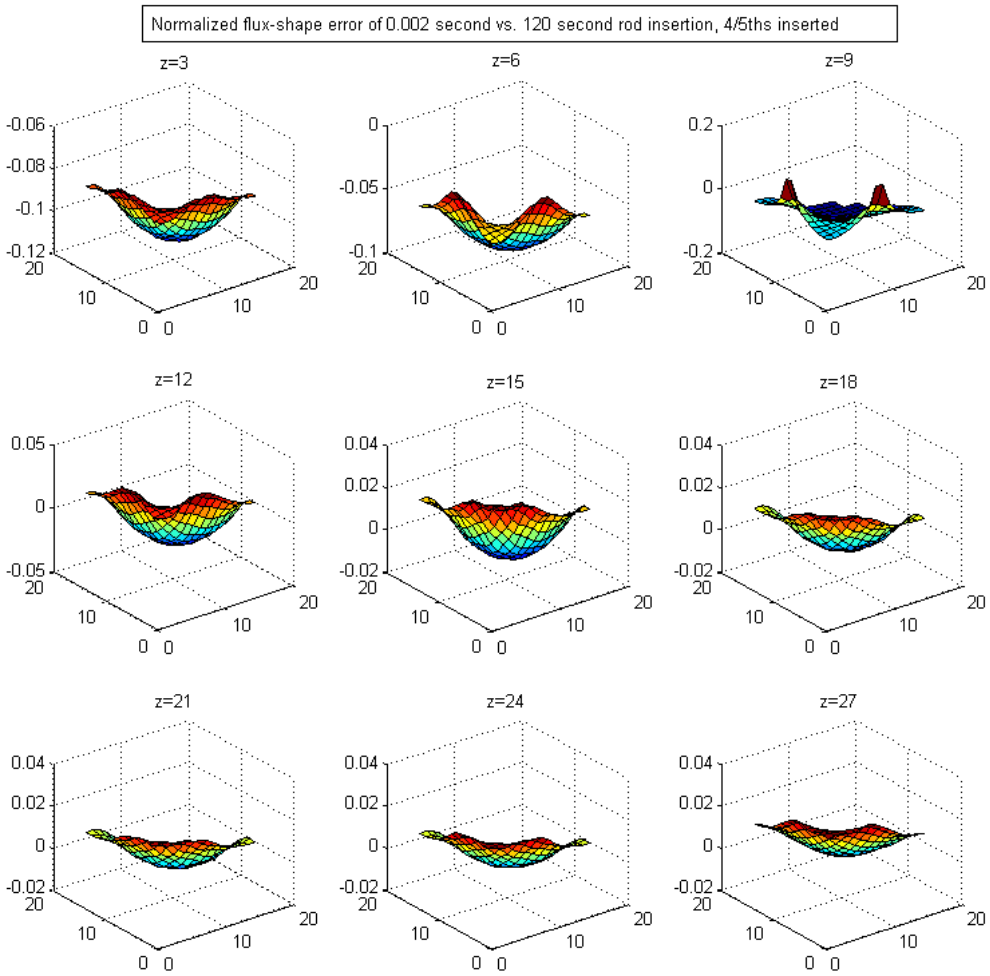

Figure 73: Normalized flux shape error, 120 second transient, 0.002 lo-fi, rods 4/5 inserted.

For the 120 second transient, the error given by the two low-fidelity transients is more comparable, as delayed neutron have had more time to change and result in a much more significant influence on the flux shape. As shown in Sections 3.3.2 and 3.3.3, the maximum error in the 120 second transient occurs closer to 60 seconds than 96 seconds when the rods are 4/5ths inserted; although the shown error for the 0.002 low-fidelity transient in Figure 73 is smaller than for the 0.05 low-fidelity in Figure 74, these are not representative of earlier in the transient where the opposite would be true. Figure 100 - Figure 105 of the Appendix show flux shape error distributions at other points in the 2 second and 120 second rod insertion transients.

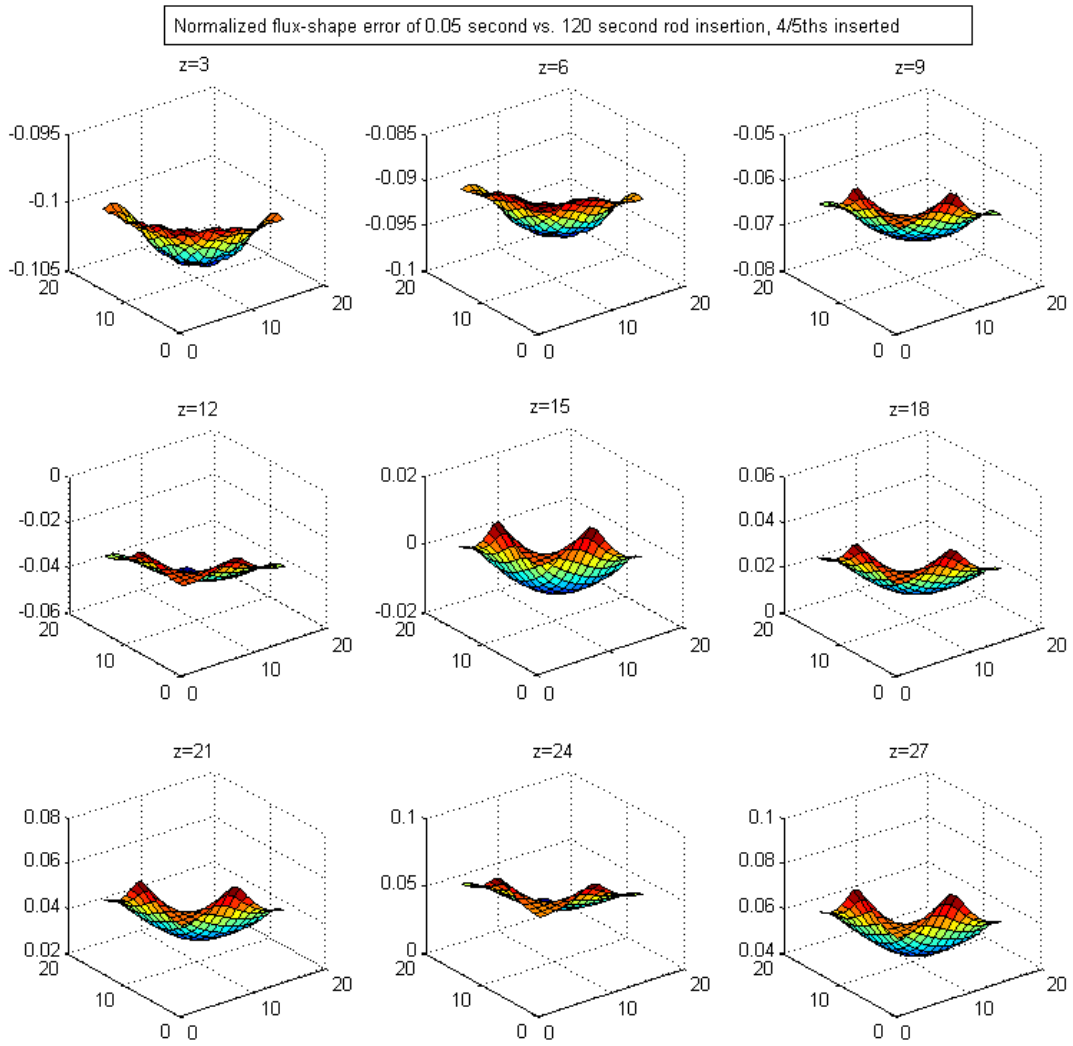

Figure 74: Normalized flux shape error, 120 second transient, 0.05 lo-fi, rods 4/5 inserted.

The 3-D plots of normalized flux shape error were compared to similar 3-D plots of delayed neutron distribution, where the vertical axis corresponds to the change in normalized delayed neutron production at a given time versus the original values.

$$\Delta_{DN,m} = \frac{\sum\left(\lambda_{i,m}C_{i,m}(0) - \lambda_{i,m}C_{i,m}(t)\right)}{\sum \lambda_{i,m}C_{i,m}(t)} \tag{3.2}$$

Since DNP concentration can be assumed to undergo negligible change during the 0.002 second and 0.05 second rapid insertion transients, the initial delayed neutron values may be used for every interval of the rapid insertions when compared to a full transient.

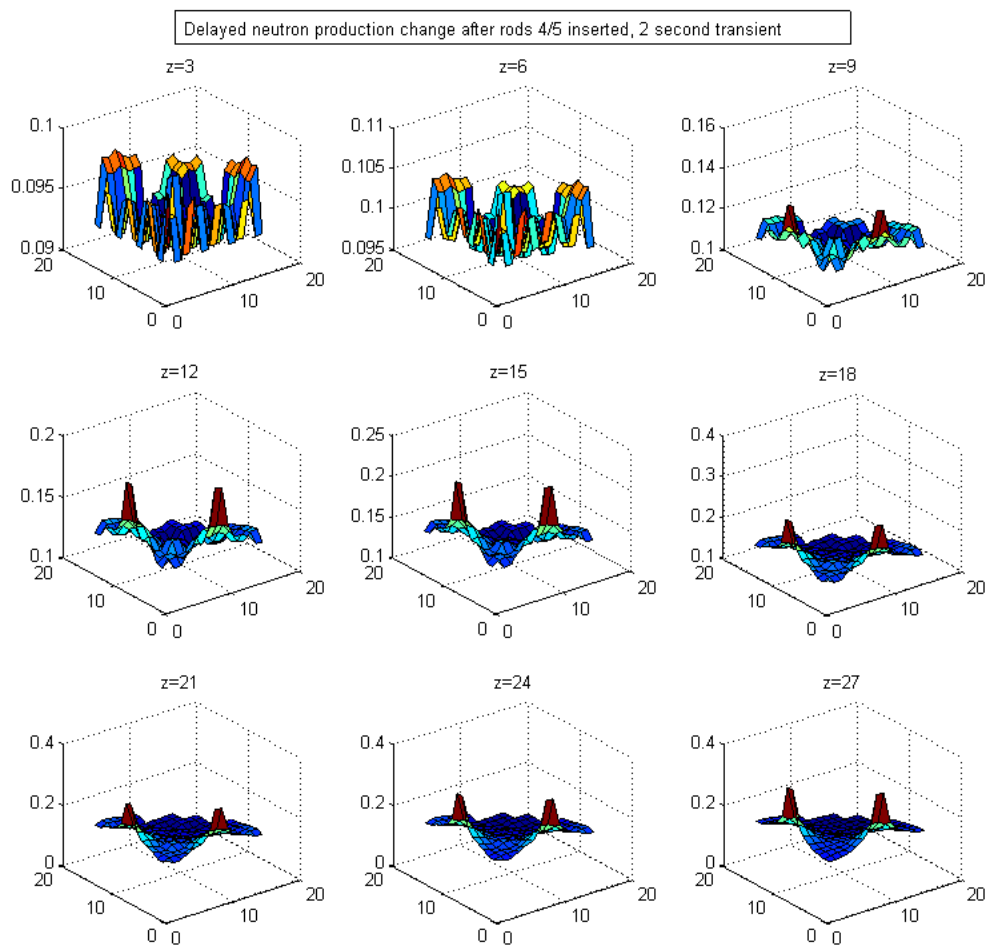

Figure 75: Normalized precursor delta, 2 second transient, rods 4/5 inserted.

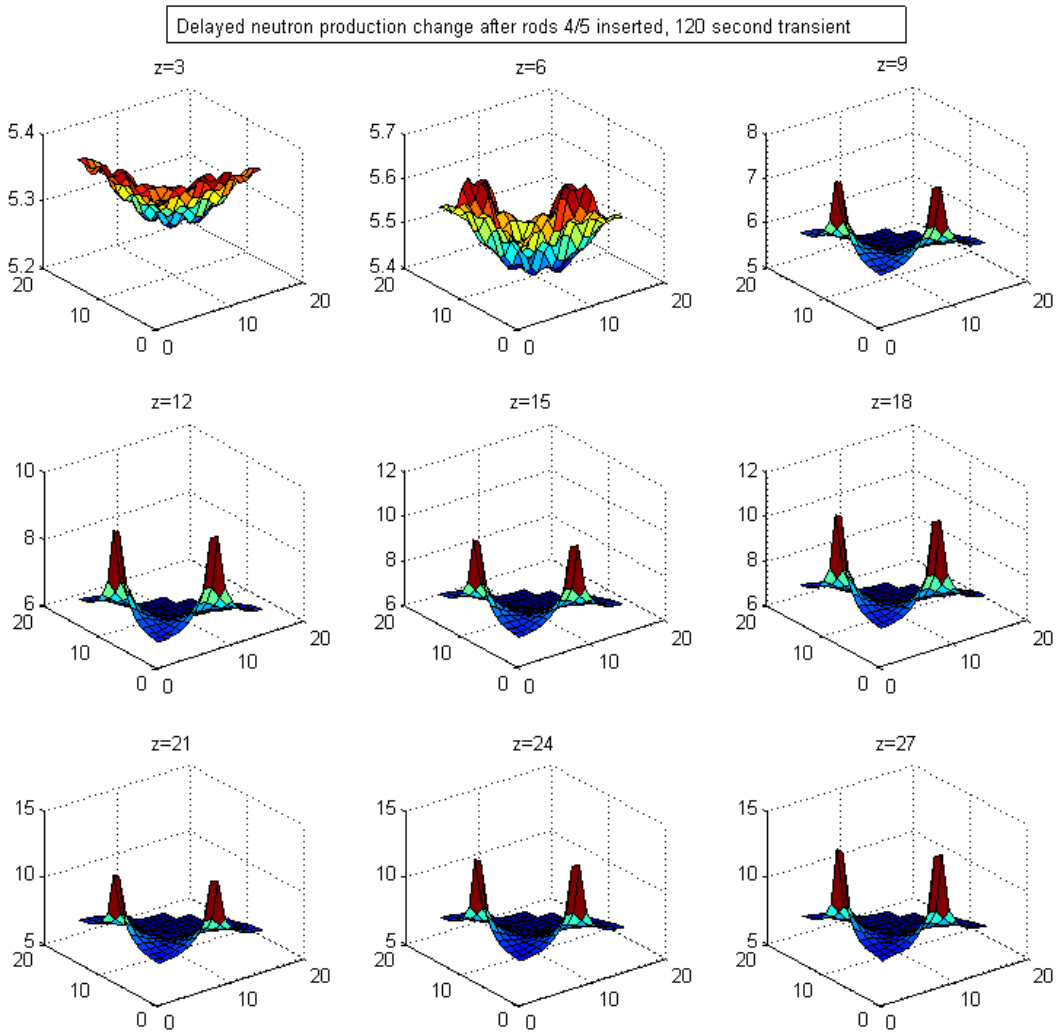

Figure 76: Normalized precursor delta, 120 second transient, rods 4/5 inserted.

Of similar, or potentially more interest, is the group-averaged and core-average normalized DNP shape delta at a given time versus the original distribution.

$$\Delta_{DNP-shape,m} = \sum \beta_i \frac{(S_{i,m}^{(C)}(0) - S_{i,m}^{(C)}(t))}{S_{i,m}^{(C)}(t)} \Big/ \sum \beta_i \tag{3.3}$$

In the DNP shape format, the correlation between delayed neutrons and the error in the flux shape is a little clearer. As can be seen in Figure 77 and Figure 78 as

compared to Figure 72 and Figure 74, there is a definite shared axial tilt in the distribution. Additionally, it is clear the normalized change in the delayed neutron distribution has a much smaller spread than the normalized flux shape error. Assuming the error in the flux shape in Figure 72 and Figure 74 is due to the contribution of delayed neutrons, the evidence suggests significant diffusion of the delayed neutrons from their birth location; because of this, the DNP concentration cannot be used in a simple manner to predict the difference in flux-shape between a 0.05 and a 2 or 120 second rod motion transient.

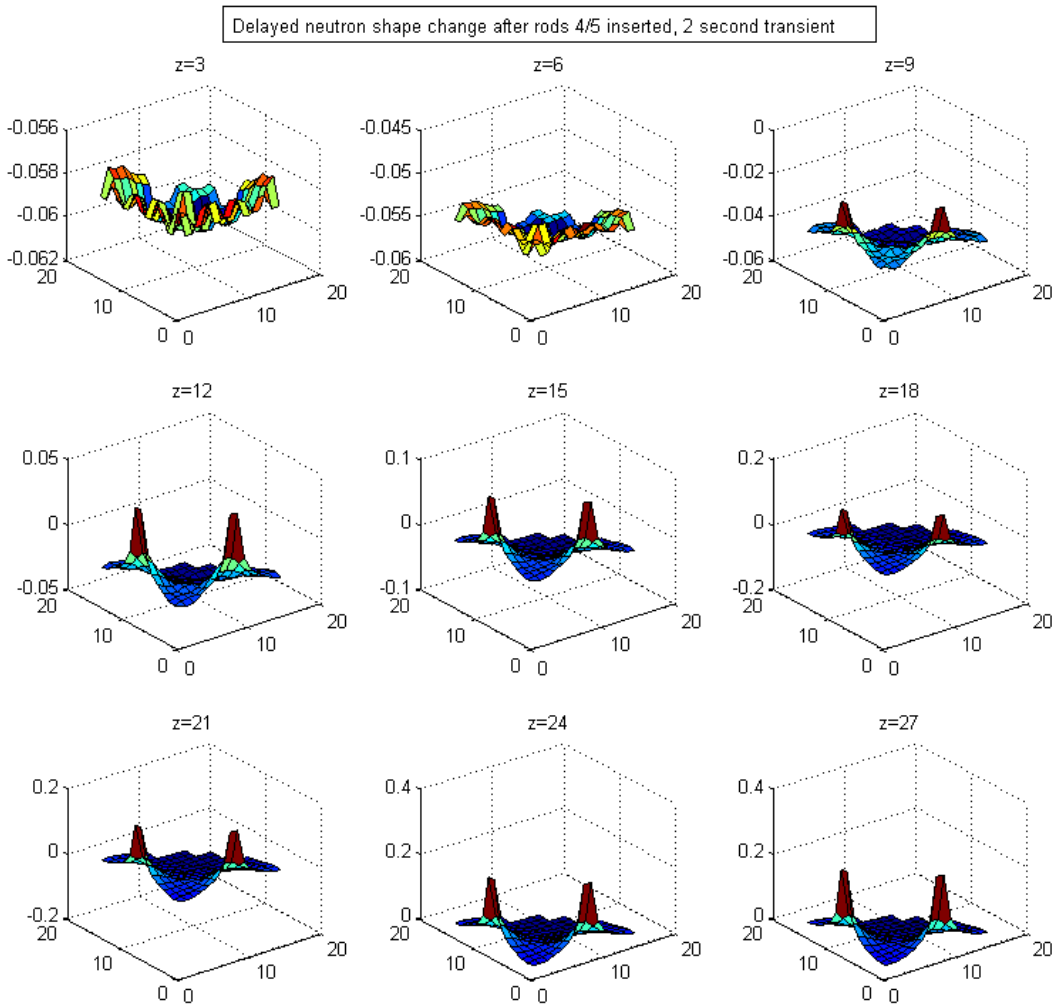

Figure 77: Normalized delayed neutron shape delta, 2 second transient, rods 4/5 inserted.

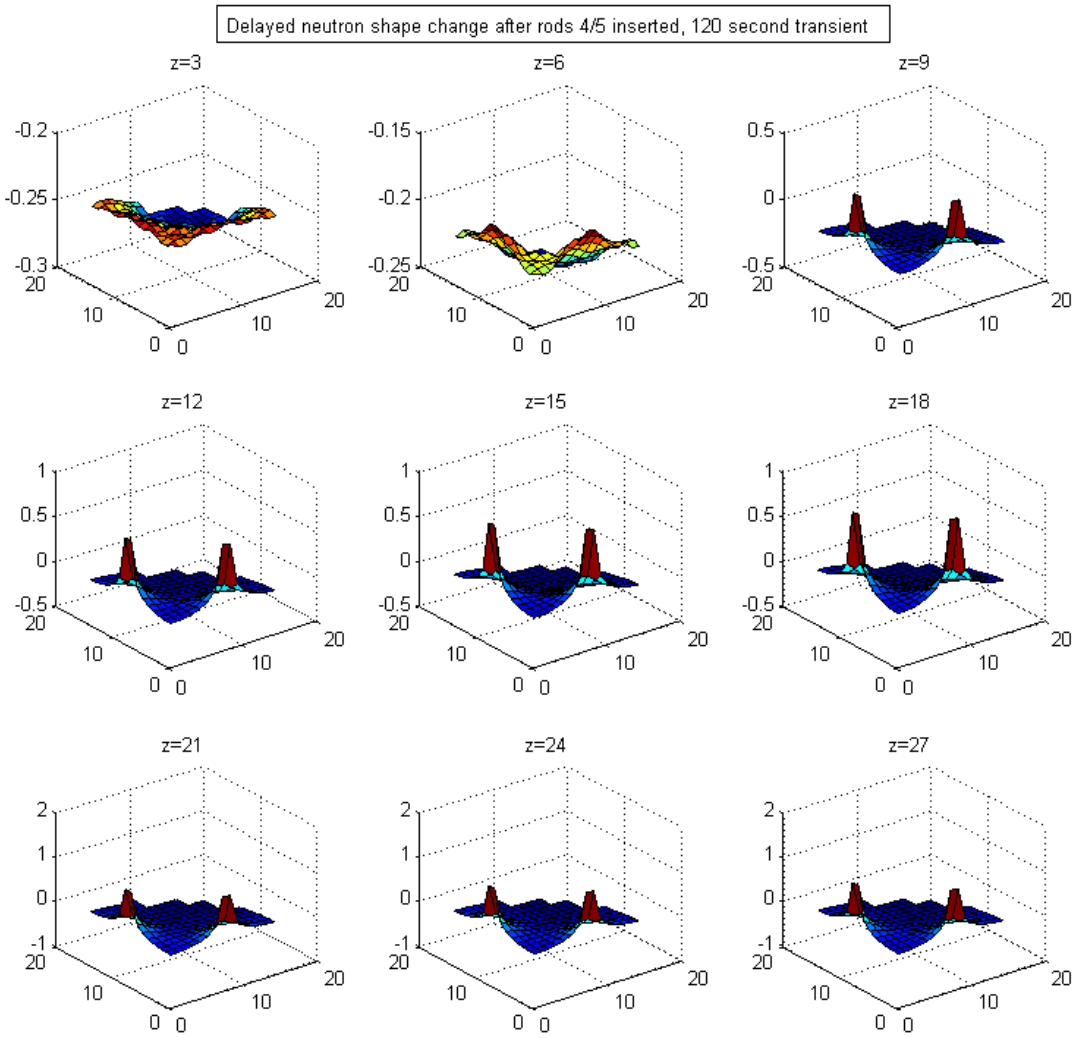

Figure 78: Normalized delayed neutron shape delta, 120 second transient, rods 4/5 inserted.

Figure 106 - Figure 111 of the Appendix show delayed neutron delta distributions at other points in the 2 second and 120 second rod insertion transients.

With prompt neutron transient error contributions removed from the low-fidelity solution, there is a clearer, if not simple correlation between the remaining normalized flux shape error and the normalized change in delayed neutron distribution. It may still be possible to further reduce the error in the low-fidelity model by applying appropriate transformations to the delayed neutron shape delta. One potential technique for this could be to develop a mathematical relationship between the DNP and their effect on flux via an expansion using Fourier overtones to describe the relationship. Fourier analysis of precursor distribution and changes could potentially assist in determining the relationship.

3.3.7 Isolation Test of Distribution Effects

An attempt to find direct correlations between the error in the flux shape-factors and the precursor shape behavior was performed using a simulated single step rod-drop counteracted by an equivalent simultaneous step decrease in boron concentration to hold the core nearly critical. Rather than directly using the precursor shape, this attempt was focused on isolating the flux-shape changes that occur following rod insertion that can be attributed solely to local changes in DNP concentration. The simulated transient began at 100% power, with a time-step of 0.01 seconds. As with the normal rod insertion transients bank 9 was inserted, but over a single time-step. Simultaneously boron was dropped from 1899.83 ppm to near its bank 9 rods-inserted steady state value of 1817.41ppm. This in effect keeps the reactor approximately critical, while swapping the source of some of the negative reactivity. Small variations were made to the boron value to find a concentration which led to an approximately steady or slowly changing power after sufficient time had passed.

An interesting and potentially critical flaw was discovered in the results of this transient. Immediately following the counteracting step reactivity changes, power underwent noticeable oscillations before settling to a slowly changing value, dependent on how closely the rod and boron reactivities were matched. The oscillations were present regardless of any variations in parameters within the scope of the test.

Parameters tested included minor variations in final boron concentration, time-step, neutron velocity, DNP beta values, and changing from a step reactivity change to a 0.1 second ramp. Comparing Figure 79 and Figure 80, it is apparent that a small change in the final boron concentration has very little effect on the oscillations, though it does change the rate of change of power in general. Comparing Figure 82 to Figure 80, it can be seen that a larger time-step produces a correspondingly slower oscillation, though the amplitude is largely unchanged. While doubling neutron velocity from Figure 81 to Figure 80 changed the frequency of the oscillations, the amplitude was unchanged. Doubled neutron velocity had no perceptible effect on the oscillations with a longer time step as seen when comparing Figure 83 to Figure 82. The overall time frame of the oscillations and the relative indifference to neutron velocity indicate that this is likely not a prompt neutron specific effect. In Figure 84, with delayed neutrons at minimal values, the oscillations are larger and slower. If the oscillations were due to a delayed neutron phenomenon, expectations are that the oscillations would disappear or be greatly reduced, corresponding to the decrease in delayed neutrons. Instead the oscillations are magnified, appearing as if a negative feedback from the delayed neutrons had been largely removed. In Figure 85 where the rods are inserted and boron decreased in a ramp fashion over 0.1 seconds, it can be seen that during the ramp there is a corresponding power transient due to mismatching changes in rod-worth vs. boron worth, after which the oscillations are still present. They are certainly smaller than the changes during the 0.1 second ramp reactivity swap, but are not actually smaller or less frequent than following a step reactivity swap.

There being no clear cause of the oscillations after the various sensitivity tests, the assumption can be made that the oscillations are most likely an artifact of the numerical algorithms within NESTLE that only becomes apparent in this specific set of circumstances.

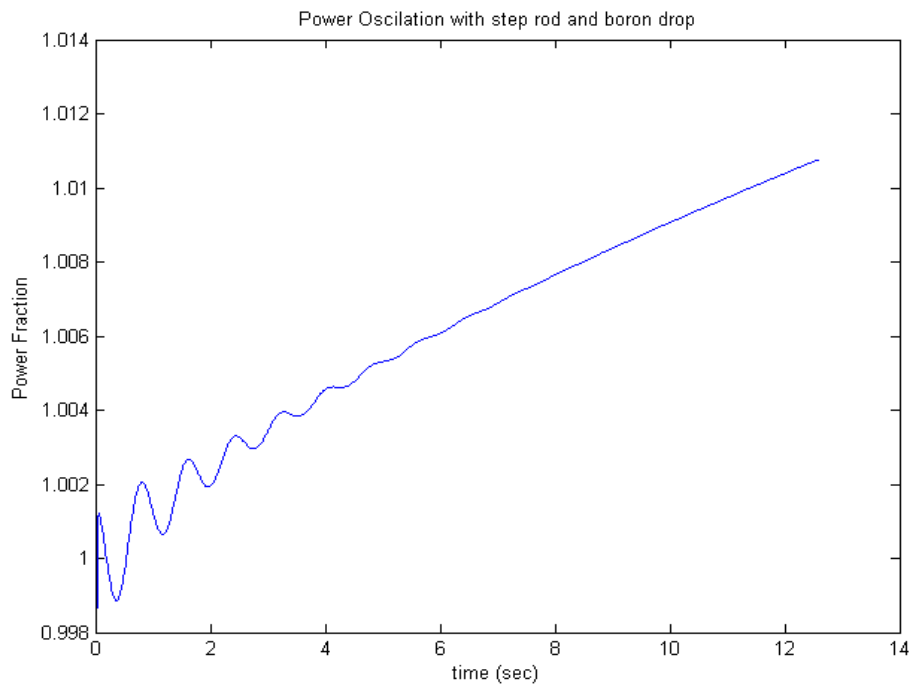

Figure 79: Power oscillations following step rod and boron decreases, 0.01 second time-step, 1817.30ppm final boron.

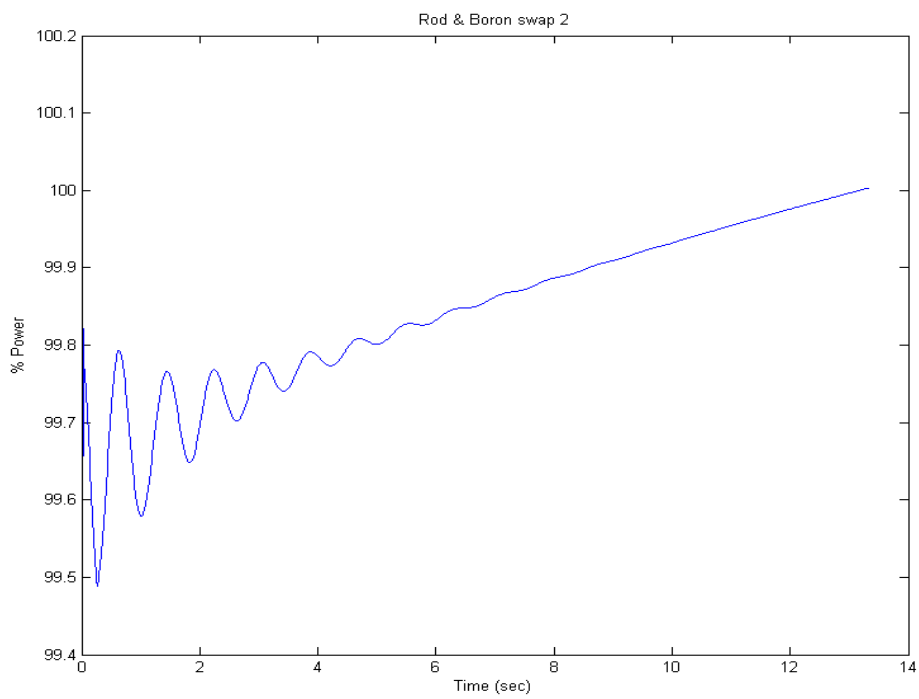

Figure 80: Power oscillations following step rod and boron decreases, 0.01 second time-step, 1817.40ppm final boron.

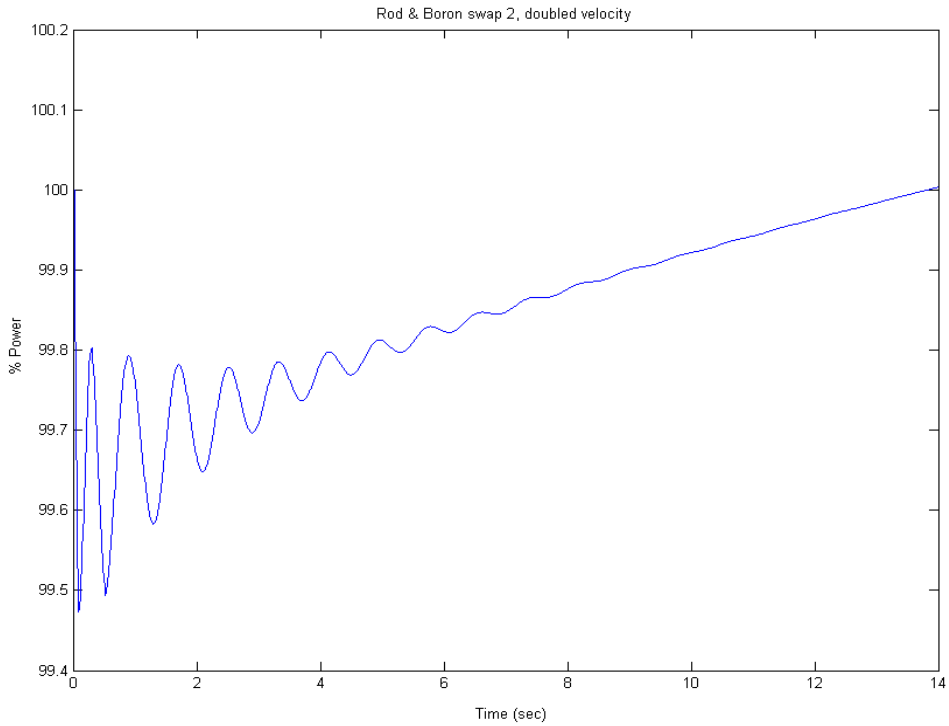

Figure 81: Power oscillations following step rod and boron decreases, 0.01 second time-step, 1817.40ppm final boron, doubled velocity.

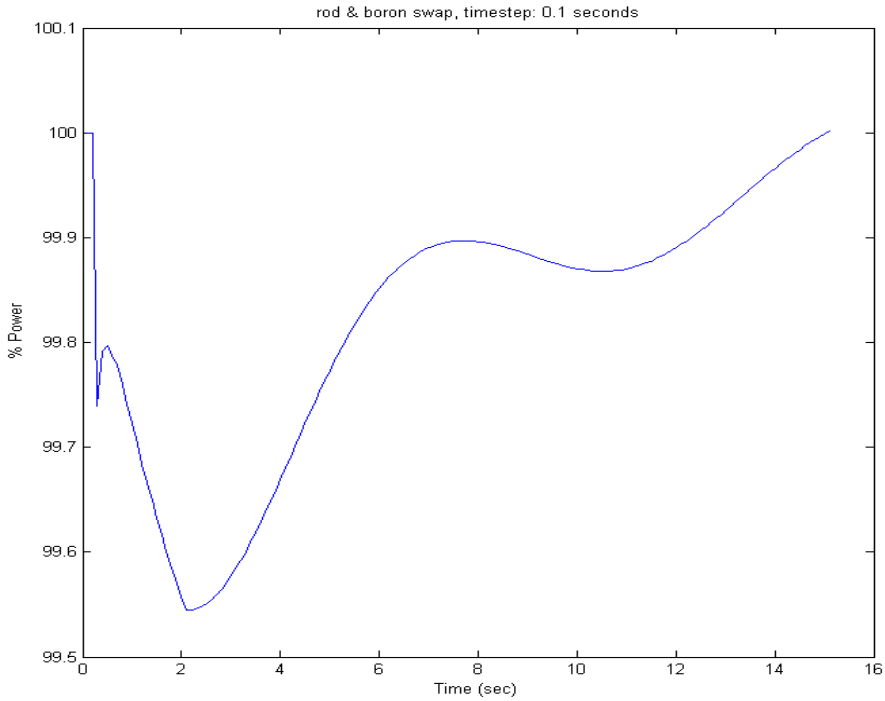

Figure 82: Power oscillations following step rod and boron decreases, 0.1 second time-step, 1817.40ppm final boron.

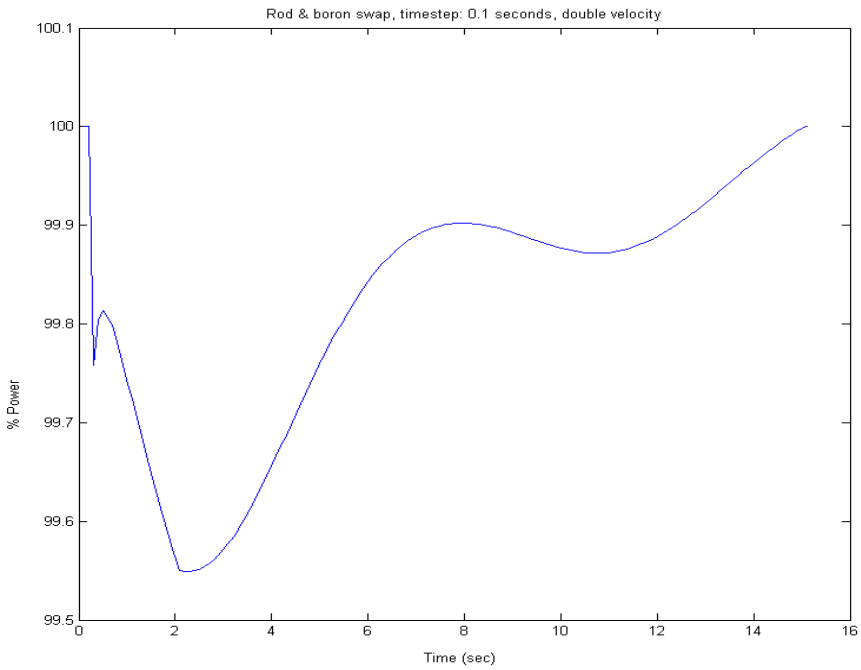

Figure 83: Power oscillations following step rod and boron decreases, 0.1 second time-step, 1817.40ppm final boron, doubled velocity.

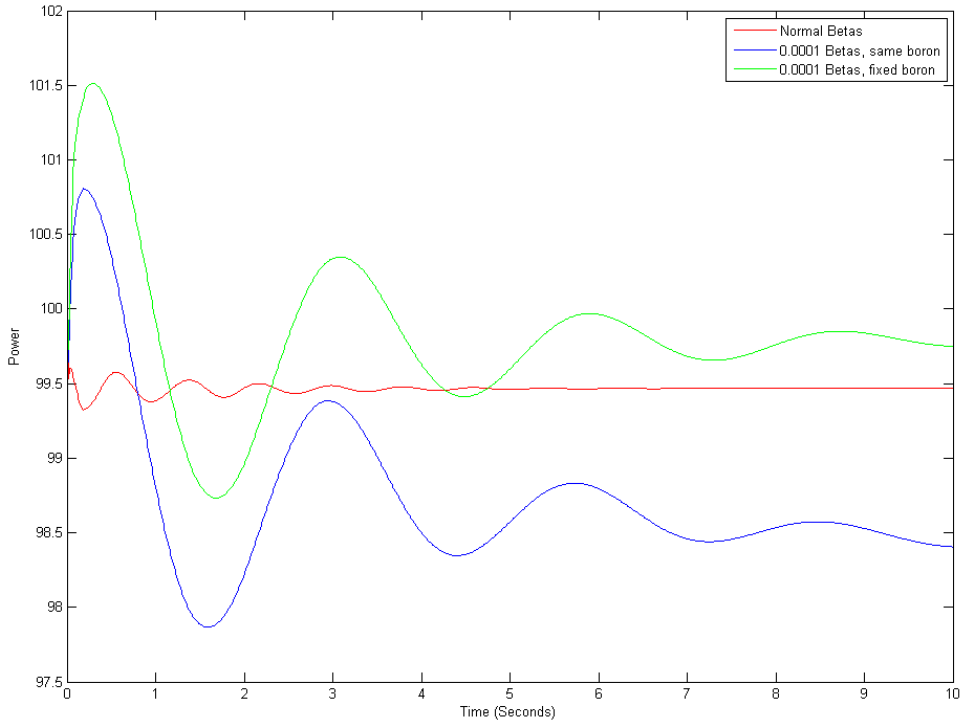

Figure 84: Power oscillations following step rod and boron decreases, 0.01 second time-step, 1817.445ppm final boron, normal vs. suppressed betas, 1817.43ppm fixed boron.

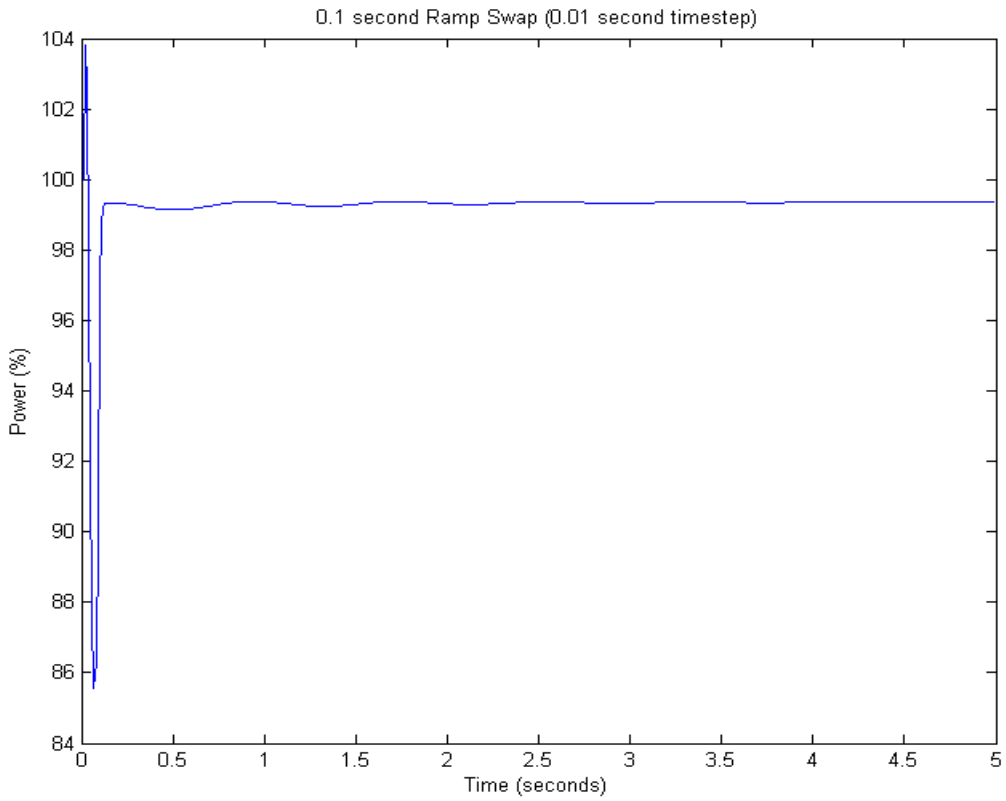

Figure 85: Power oscillations following step rod and boron decreases, 0.01 second time-step, 1817.445ppm final boron, 0.1 second ramp reactivity change.

Despite the oscillations in power following the step reactivity swap, the flux shape-factor results show potential, even with the fact that the step reactivity swap shape-factors did not entirely match steady state flux shape even after 500 seconds. Figure 86 displays the radial flux shape at various axial heights in the core for bank 9 control rods in at steady state. The pseudo-steady state following the step boron and rod swap appeared virtually identical to the steady state, but had minor differences. After 1000 seconds the difference was not noticeably changed, suggesting further settling of the flux shape would not have much effect and that the difference would remain no matter how long the simulation was allowed to run. Figure 112 and Figure 113 in the appendix show the normalized distribution deltas for flux and delayed neutron production between 500 and 1000 seconds after the reactivity swap.

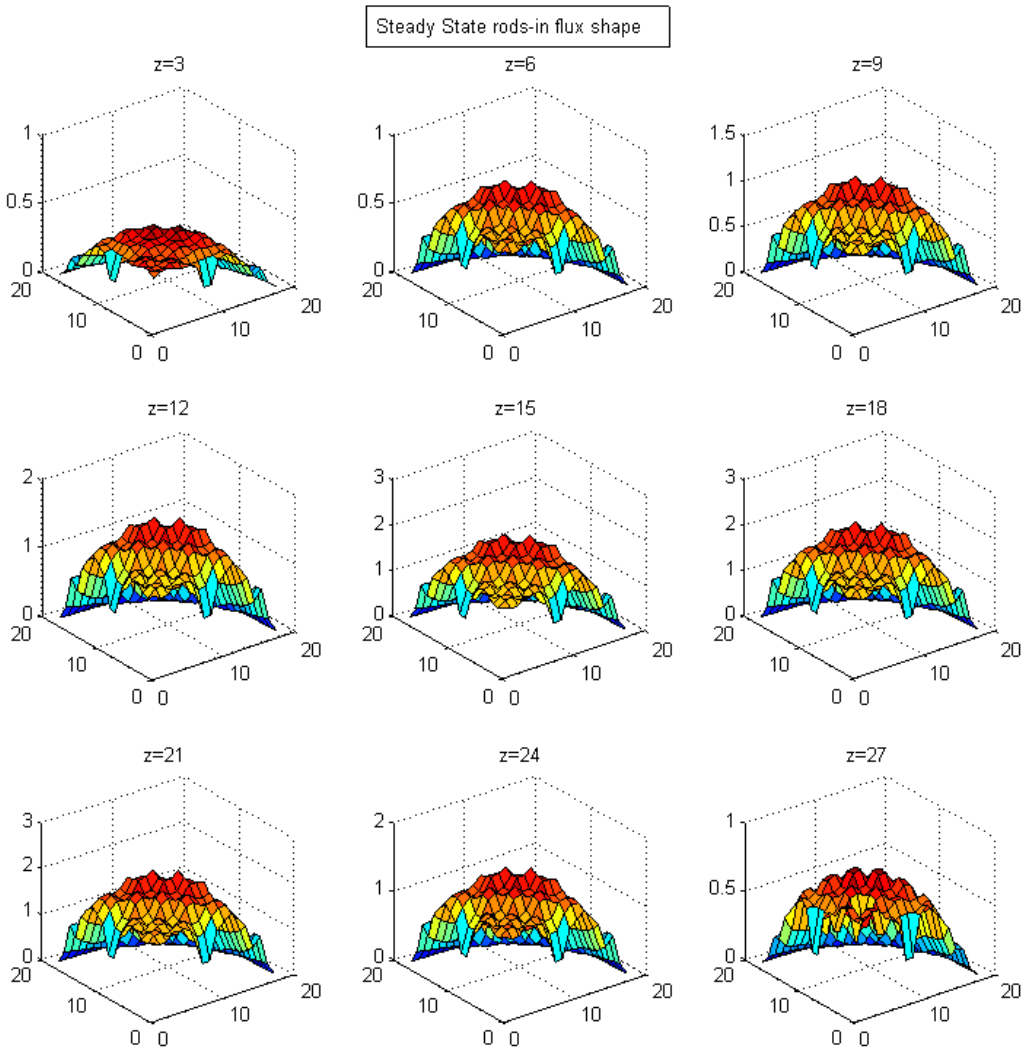

Figure 86: Steady state radial flux shape at various axial heights in the core with bank 9 control rods fully inserted.

Comparisons between flux shapes at various times in the transient after the reactivity-swap revealed definite similarities to sample error distributions in the flux shape-factors for both the 120 and 2 second transient cases, though more-so for the 120 second case. The comparisons were done using the following formulation,

$$\Delta_{flux\cdot shape,(g=2),m} = \frac{S_{2,m}^{(\phi)}(t_1) - S_{2,m}^{(\phi)}(t_2)}{S_{2,m}^{(\phi)}(t_2)}. \tag{3.4}$$

Examining Figure 87 and Figure 88, which show the change in the distribution of the flux over periods of 1 second and 1000 seconds after the reactivity swap, reveals a similar radial profile to the rodded radial slices shown in Figure 74 for the 120 second rod insertion transient. There is also some similarity to the rodded slices of Figure 72 for the 2 second rod insertion transient. While there is some development of an axial tilt in the transient following the reactivity swap, it is not nearly as significant as in the 2 second and 120 second rod insertion transients. Observing the error in Figure 74, the difference in axial tilt impacts the relative average magnitude of each radial slice, however the total variation in flux delta at each height is quite similar to that shown in Figure 88.

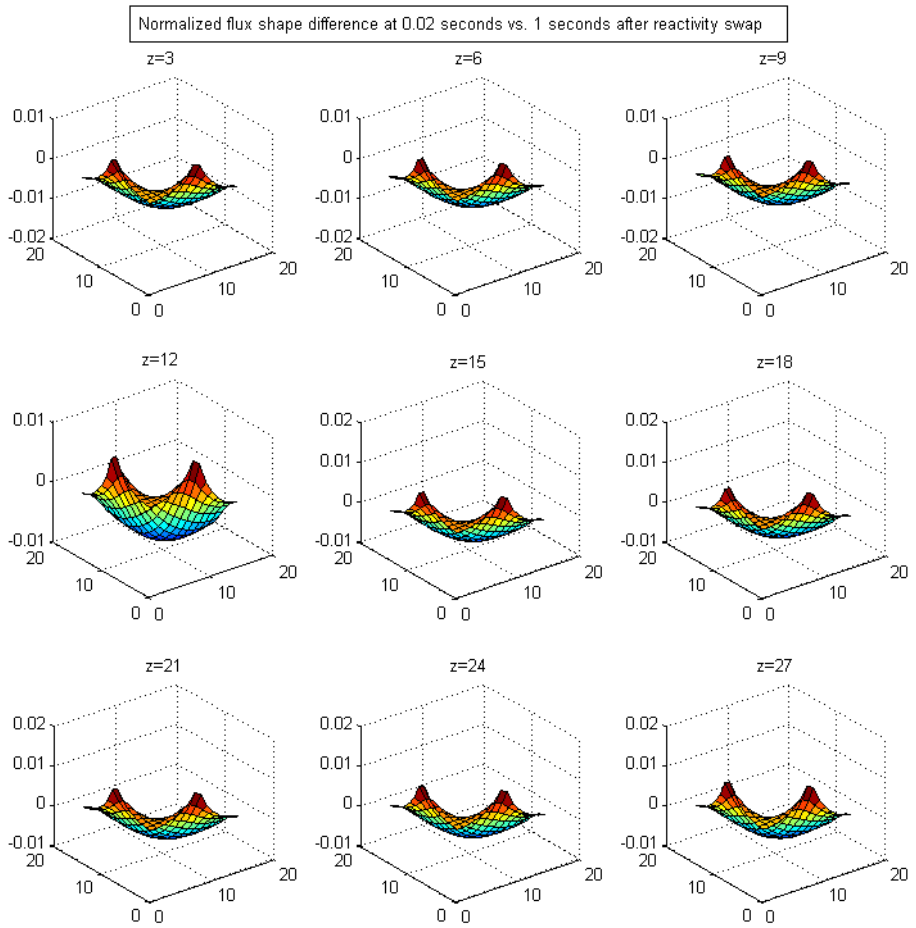

Figure 87: Normalized difference in radial flux shape at various axial heights at 0.02 seconds versus 1 seconds.

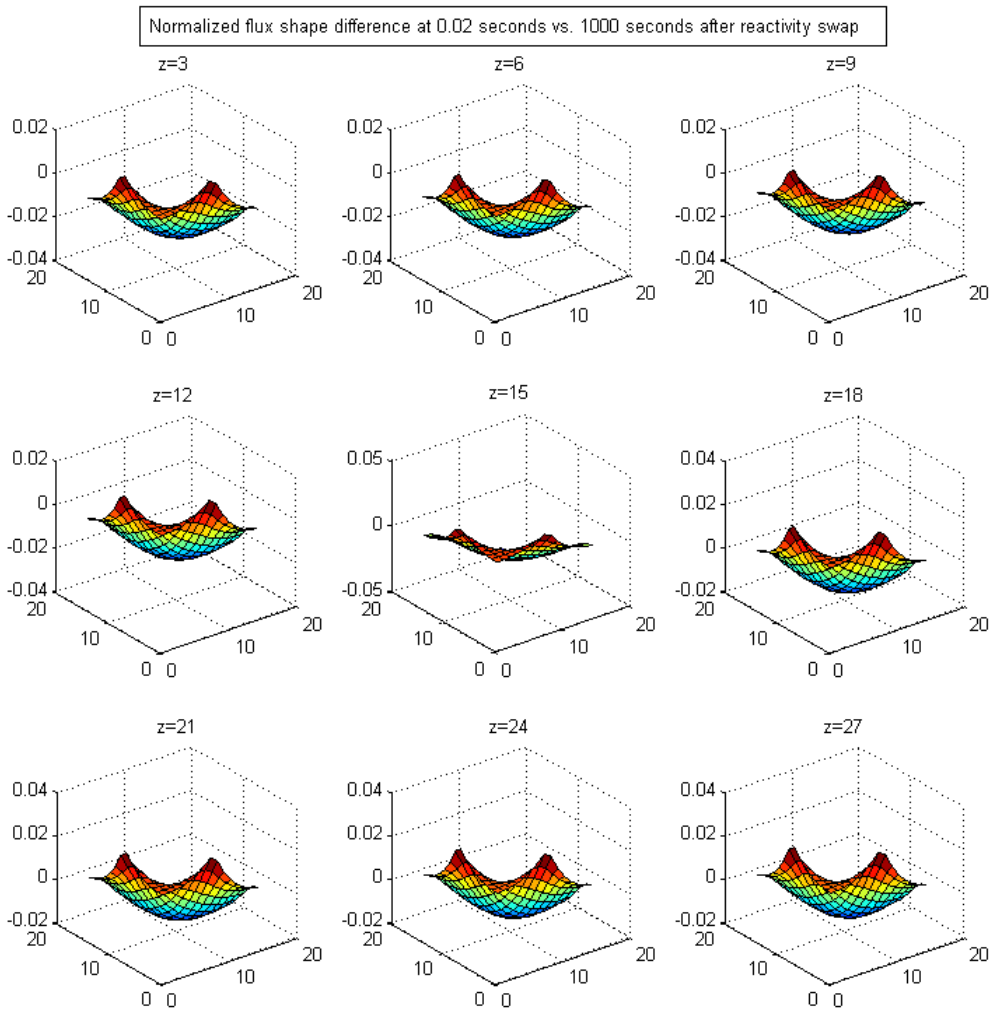

Figure 88: Normalized difference in radial flux shape at various axial heights at 0.02 seconds versus 1000 seconds.

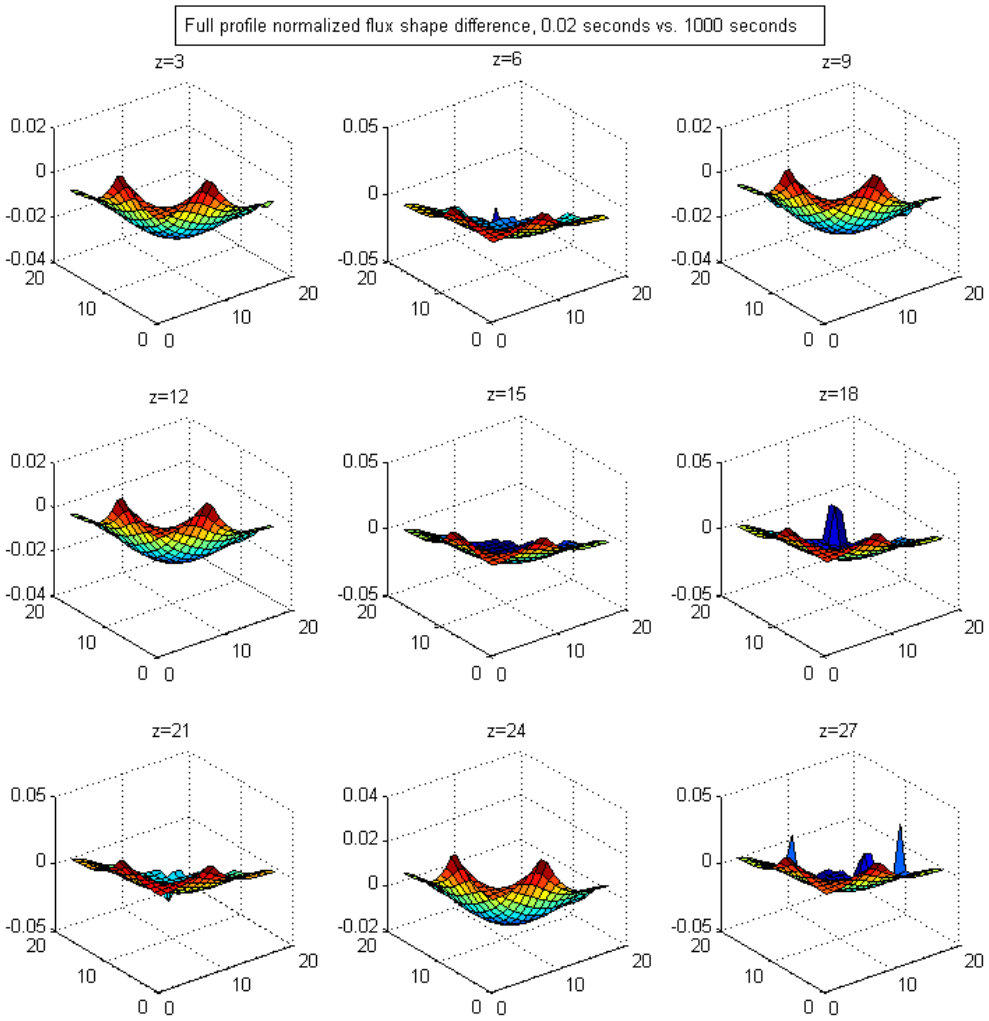

Figure 89: Normalized difference in radial flux shape, including non-fueled regions, at various axial heights at 0.02 seconds versus 1000 seconds.

Figure 89 contains normalized difference values over the entire radial range of the flux shape, including non-fuel regions, where the majority of the negative values occur. These were excluded from the preceding analysis for the same reasons previously described in Section 3.3.6. They are shown here to demonstrate that the delta in the shape-factors should integrate to 0 when all values are included.

Normalized delayed neutron production delta profiles over the corresponding time periods show matching behavior, as seen in Figure 90 and Figure 91. The axial tilt seen in the 2 second and 120 second ramp insertion transients is still absent, but otherwise the behavior is very similar.

The reactivity swap test provides a clear demonstration of the effect of control rods on delayed neutron production and its effect on flux shape without the complications of ramp transient effects such as axial tilt. They support the conclusions reached in Section 3.3.6 about the relationship between delayed neutron production and the error in the flux shape between a rapid transient and a transient which is affected by delayed neutrons. These results could be used to assist in developing a mathematical relationship between delayed neutron production and flux distribution changes.

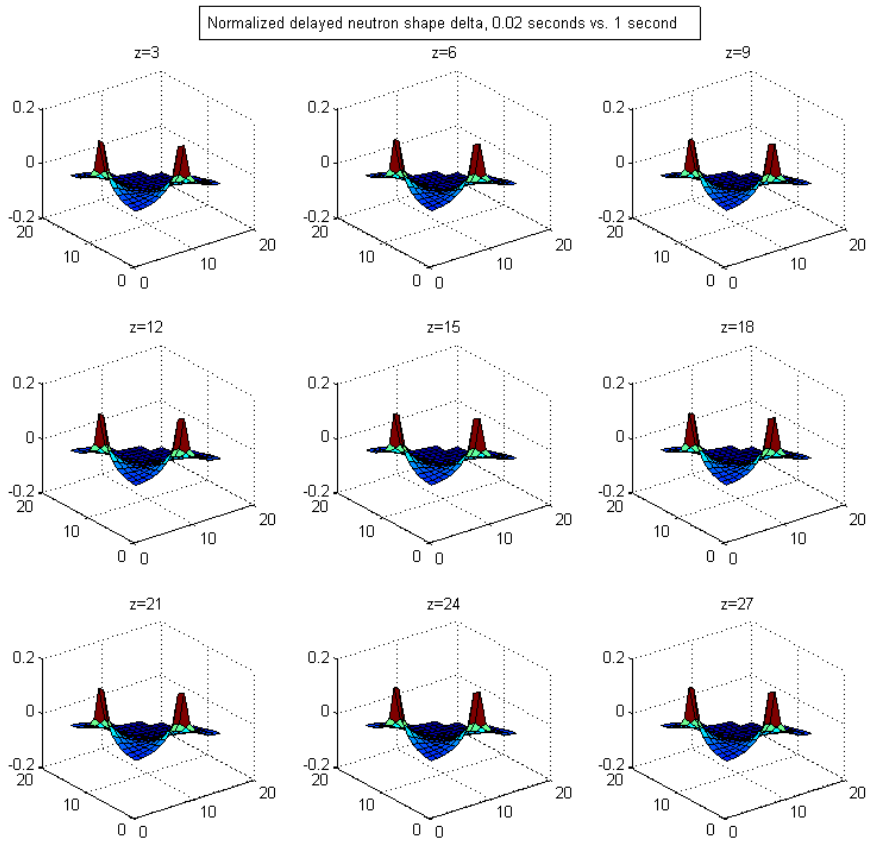

Figure 90: Normalized difference in radial delayed neutron production distribution, at various axial heights at 0.02 seconds versus 1 second.

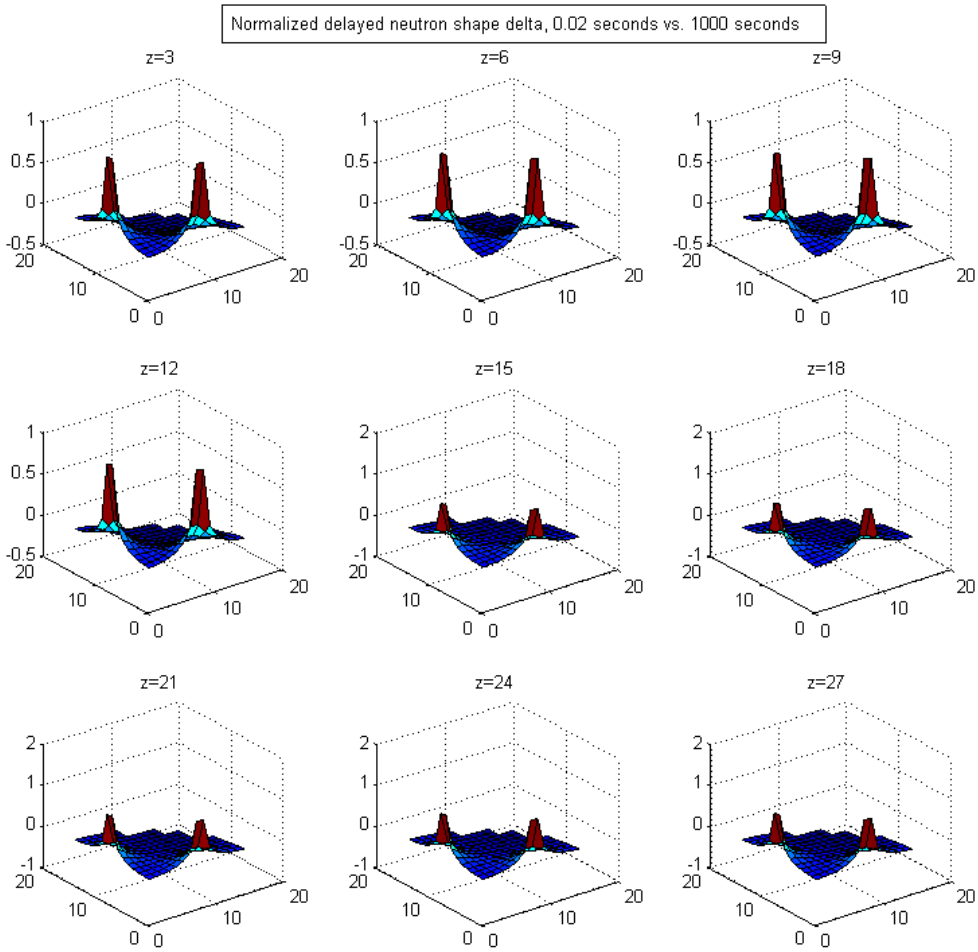

Figure 91: Normalized difference in radial delayed neutron production distribution, at various axial heights at 0.02 seconds versus 1000 seconds.

These results make it clear that the majority of the error in the low-fidelity model derives from the axial tilt difference between a rapid and a realistic ramp rod insertion transient. This suggests that a 1-D simulation with axially normalized shape-factors could provide a low-fidelity model with very reasonable fidelity and predictable error behavior. The largest flux error would likely be on the order of 2%. This should be relatively simple to implement and could provide interesting analysis opportunities relating to the prediction of error in the low-fidelity solution.

4. Conclusions and Recommendations:

The AMoR model requires further work on the generalized adjoint solution to allow it to be utilized as intended. Despite this, the quasi-statics based low-fidelity model developed to assist in the proof of concept has turned out to be reasonably accurate for short transients. If an easily computed prediction of the delayed neutron effects on flux shape can be developed, the low-fidelity model should maintain accuracy for a significant range of potential transients. In regards to the low-fidelity model used here, a key observation is that the error in the projected solution is very sensitive to certain changes in the projection operator generation, especially in regards to using a rapid transient with inherent prompt neutron behavior differences from the solution it is intended to represent. The sensitivity also holds to some degree during high-fidelity updates to the low-fidelity solution. These prompt neutron behavior artifacts were present in the previous work on this topic. This sensitivity is something to be watchful of in all future permutations of the AMoR method.

With prompt neutron transient error contributions removed from the low-fidelity solution, there is a clear correlation between the neutron flux error and the change in delayed neutron precursor distribution, both amplitude and shape, during the transient. The hybrid precursor solution has sufficient accuracy that it may be possible to use it to further reduce the error in the low-fidelity model by developing and applying appropriate mathematical relationships to correct for the delayed neutron effects on flux distribution, which are not included when the projection operators are produced using a rapid insertion transient on the order of 0.05 seconds. Alternately, a 1-D axial core model, generated in a consistent manner as used to generate the PKE, could be substituted for the PKE model for the low-fidelity solution, providing reasonable accuracy as well as potential opportunities for error prediction.

4.1 Future Work

Potential features that would make the low-fidelity model more comprehensive would include adding thermal-hydraulics, as well as enabling the ability to model boron induced transients in the PKP, PKE-solver, and AMoR subroutines. With these additions and a completed means of correcting for delayed neutron error contributions, the low-fidelity model using rapid insertion projection factors and PKE-solver could be quite accurate in a wide range of realistic reactor transients.

Pursuing radial 2-D projection of a 1-D axial model for the low-fidelity solution may provide a straightforward way to correct for the majority of the delayed neutron induced flux error evident in the PKE projected model, without needing to develop complicated mathematical relationships. Subsequently, there may be easily predictable relationships between the error in the low-fidelity model and DNP behavior or rod position.

Additionally, it might be of interest to examine the AMoR method with a true quasi-static method employed to create the multi-fidelity model. This would provide a more mathematically rigorous formulation of the coupling between the low-fidelity solution and the high-fidelity solution, which may offer more accurate predictions when switching between them.

The AMoR method itself, while showing some merit, still requires a way to estimate the error without solving the high-fidelity transient to function as envisioned. All metrics used in the error analysis performed here, and even the error response measurement as it currently functions, require that the full high-fidelity forward transient be calculated beforehand. Using time-spatial dependent generalized perturbation theory, as implemented in NESTLE, the ability to predict an error metric independent of the forward solution has been demonstrated; however, the CPU time associated with solving for the generalized adjoint flux is much greater than solving the forward problem. To be computationally efficient, a low-fidelity generalized adjoint solution formulation with sufficient accuracy to determine an error metric is required.

REFERENCES

[1] S. J. Satterfield, "The Application of Adaptive Model Refinement to Nuclear Reactor Core Simulation," Master's Thesis, NCSU, 2013.

[2] Electric Power Research Center, *NESTLE version 5.2.1,* NCSU, 2003.

[3] S. Dulla, E. H. Mund and P. Ravetto, "The quasi-static method revisited," *Progress in Nuclear Energy,* vol. 50, pp. 908-920, 2008.

[4] J. J. Duderstadt and L. J. Hamilton, Nuclear Reactor Analysis, New York: Wiley, 1976.

[5] J. R. Lamarsh and A. J. Baratta, Introduction to Nuclear Engineering, New Jersey: Prentice-Hall, Inc., 2001.

[6] Electric Power Research Center, User's Manual: RAMBO Version 1.0.1 "Dynamic Reactivity Measurement of Rod Worth", NCSU, 2002.

[7] G. I. Bell and S. Glasstone, Nuclear Reactor Theory, U.S.: Van Nostrand Reinhold Inc., 1970.

APPENDIX

Sample Error Response Output

Step,	Time,	<f, dPsi>,	<Psi*, r>
1,	0.1000000E-01,	0.0000000E+00,	-0.6986282E+09
2,	0.2000000E-01,	0.0000000E+00,	-0.9393274E+11
3,	0.3000000E-01,	0.0000000E+00,	-0.7232380E+09
4,	0.4000000E-01,	0.0000000E+00,	-0.7218498E+09
5,	0.5000000E-01,	0.0000000E+00,	-0.7210865E+09
6,	0.5999999E-01,	0.0000000E+00,	-0.7201150E+09
7,	0.6999999E-01,	0.0000000E+00,	-0.7192879E+09
8,	0.7999999E-01,	0.0000000E+00,	-0.7179455E+09
9,	0.8999999E-01,	0.0000000E+00,	-0.7171660E+09
10,	0.1000000E+00,	0.0000000E+00,	-0.7161688E+09
11,	0.1100000E+00,	0.0000000E+00,	-0.7153466E+09
12,	0.1200000E+00,	0.0000000E+00,	-0.7143168E+09
13,	0.1300000E+00,	0.0000000E+00,	-0.7134843E+09
14,	0.1400000E+00,	0.0000000E+00,	-0.7112076E+09
15,	0.1500000E+00,	0.0000000E+00,	-0.7104298E+09
16,	0.1600000E+00,	0.0000000E+00,	-0.7093535E+09
17,	0.1700000E+00,	0.0000000E+00,	-0.7084226E+09
18,	0.1800000E+00,	0.0000000E+00,	-0.7074026E+09
19,	0.1900000E+00,	0.0000000E+00,	-0.7064349E+09
20,	0.2000000E+00,	0.0000000E+00,	-0.7054096E+09
21,	0.2100000E+00,	0.0000000E+00,	-0.7045327E+09
22,	0.2200000E+00,	0.0000000E+00,	-0.7040438E+09
23,	0.2300000E+00,	0.0000000E+00,	-0.7031025E+09
24,	0.2400000E+00,	0.0000000E+00,	-0.7020376E+09
25,	0.2500000E+00,	0.0000000E+00,	-0.7010223E+09
26,	0.2600000E+00,	0.0000000E+00,	-0.6999512E+09
27,	0.2700000E+00,	0.0000000E+00,	-0.6989963E+09
28,	0.2800000E+00,	0.0000000E+00,	-0.6978735E+09
29,	0.2900000E+00,	0.0000000E+00,	-0.6967511E+09
30,	0.3000000E+00,	0.0000000E+00,	-0.6956222E+09
31,	0.3100000E+00,	0.0000000E+00,	-0.6946283E+09
32,	0.3200000E+00,	0.0000000E+00,	-0.6934692E+09
33,	0.3300000E+00,	0.0000000E+00,	-0.6923857E+09
34,	0.3399999E+00,	0.0000000E+00,	-0.6912023E+09
35,	0.3499999E+00,	0.0000000E+00,	-0.6901124E+09
36,	0.3599999E+00,	0.0000000E+00,	-0.6889005E+09
37,	0.3699999E+00,	0.0000000E+00,	-0.6877902E+09
38,	0.3799999E+00,	0.0000000E+00,	-0.6865626E+09
39,	0.3899999E+00,	0.0000000E+00,	-0.6854335E+09
40,	0.3999999E+00,	0.0000000E+00,	-0.6841793E+09
41,	0.4099999E+00,	0.0000000E+00,	-0.6830159E+09
42,	0.4199999E+00,	0.0000000E+00,	-0.6817313E+09
43,	0.4299999E+00,	0.0000000E+00,	-0.6805386E+09
44,	0.4399998E+00,	0.0000000E+00,	-0.6792141E+09
45,	0.4499998E+00,	0.0000000E+00,	-0.6779731E+09
46,	0.4599998E+00,	0.0000000E+00,	-0.6766016E+09
47,	0.4699998E+00,	0.0000000E+00,	-0.6752304E+09
48,	0.4799998E+00,	0.0000000E+00,	-0.6736227E+09
49,	0.4899998E+00,	0.0000000E+00,	-0.6719548E+09
50,	0.4999998E+00,	0.0000000E+00,	-0.6697777E+09

51,	0.5099998E+00,	0.0000000E+00,	-0.2030219E+09
52,	0.5199998E+00,	0.0000000E+00,	-0.1558049E+08
53,	0.5299998E+00,	0.0000000E+00,	-0.2303756E+09
54,	0.5399998E+00,	0.0000000E+00,	-0.8381209E+09
55,	0.5499998E+00,	0.0000000E+00,	-0.1828266E+10
56,	0.5599998E+00,	0.0000000E+00,	-0.3289465E+10
57,	0.5699998E+00,	0.0000000E+00,	-0.5114168E+10
58,	0.5799997E+00,	0.0000000E+00,	-0.7124509E+10
59,	0.5899997E+00,	0.0000000E+00,	-0.9173578E+10
60,	0.5999997E+00,	0.0000000E+00,	-0.9461042E+10
61,	0.6099997E+00,	0.0000000E+00,	-0.9439774E+10
62,	0.6199997E+00,	0.0000000E+00,	-0.1012127E+11
63,	0.6299997E+00,	0.0000000E+00,	-0.1142735E+11
64,	0.6399997E+00,	0.0000000E+00,	-0.1327567E+11
65,	0.6499997E+00,	0.0000000E+00,	-0.1613627E+11
66,	0.6599997E+00,	0.0000000E+00,	-0.1947934E+11
67,	0.6699997E+00,	0.0000000E+00,	-0.2361767E+11
68,	0.6799996E+00,	0.0000000E+00,	-0.2396679E+11
69,	0.6899996E+00,	0.0000000E+00,	-0.2423403E+11
70,	0.6999996E+00,	0.0000000E+00,	-0.2531336E+11
71,	0.7099996E+00,	0.0000000E+00,	-0.2691193E+11
72,	0.7199996E+00,	0.0000000E+00,	-0.2912939E+11
73,	0.7299996E+00,	0.0000000E+00,	-0.3183835E+11
74,	0.7399996E+00,	0.0000000E+00,	-0.3505755E+11
75,	0.7499996E+00,	0.0000000E+00,	-0.3874766E+11
76,	0.7599996E+00,	0.0000000E+00,	-0.4120492E+11
77,	0.7699996E+00,	0.0000000E+00,	-0.4058801E+11
78,	0.7799996E+00,	0.0000000E+00,	-0.4130200E+11
79,	0.7899995E+00,	0.0000000E+00,	-0.4303485E+11
80,	0.7999995E+00,	0.0000000E+00,	-0.4540257E+11
81,	0.8099995E+00,	0.0000000E+00,	-0.4815949E+11
82,	0.8199995E+00,	0.0000000E+00,	-0.5141827E+11
83,	0.8299995E+00,	0.0000000E+00,	-0.5514279E+11
84,	0.8399995E+00,	0.0000000E+00,	-0.5928910E+11
85,	0.8499995E+00,	0.0000000E+00,	-0.5931522E+11
86,	0.8599995E+00,	0.0000000E+00,	-0.5929078E+11
87,	0.8699995E+00,	0.0000000E+00,	-0.6024112E+11
88,	0.8799995E+00,	0.0000000E+00,	-0.6190893E+11
89,	0.8899994E+00,	0.0000000E+00,	-0.6427566E+11
90,	0.8999994E+00,	0.0000000E+00,	-0.6721823E+11
91,	0.9099994E+00,	0.0000000E+00,	-0.7071068E+11
92,	0.9199994E+00,	0.0000000E+00,	-0.7505093E+11
93,	0.9299994E+00,	0.0000000E+00,	-0.7794897E+11
94,	0.9399994E+00,	0.0000000E+00,	-0.7748144E+11
95,	0.9499994E+00,	0.0000000E+00,	-0.7805134E+11
96,	0.9599994E+00,	0.0000000E+00,	-0.7943767E+11
97,	0.9699994E+00,	0.0000000E+00,	-0.8140301E+11
98,	0.9799994E+00,	0.0000000E+00,	-0.8389941E+11
99,	0.9899994E+00,	0.0000000E+00,	-0.8685807E+11
100,	0.9999993E+00,	0.0000000E+00,	-0.9018950E+11
101,	0.1009999E+01,	0.0000000E+00,	-0.9370046E+11
102,	0.1019999E+01,	0.0000000E+00,	-0.9294447E+11
103,	0.1029999E+01,	0.0000000E+00,	-0.9216433E+11
104,	0.1039999E+01,	0.0000000E+00,	-0.9229273E+11
105,	0.1049999E+01,	0.0000000E+00,	-0.9266101E+11
106,	0.1059999E+01,	0.0000000E+00,	-0.9370482E+11
107,	0.1069999E+01,	0.0000000E+00,	-0.9532449E+11
108,	0.1079999E+01,	0.0000000E+00,	-0.9748739E+11
109,	0.1089999E+01,	0.0000000E+00,	-0.1000257E+12
110,	0.1099999E+01,	0.0000000E+00,	-0.1012636E+12
111,	0.1109999E+01,	0.0000000E+00,	-0.9929171E+11
112,	0.1119999E+01,	0.0000000E+00,	-0.9838564E+11
113,	0.1129999E+01,	0.0000000E+00,	-0.9831016E+11
114,	0.1139999E+01,	0.0000000E+00,	-0.9899783E+11
115,	0.1149999E+01,	0.0000000E+00,	-0.1002439E+12

116,	0.1159999E+01,	0.0000000E+00,	-0.1020653E+12
117,	0.1169999E+01,	0.0000000E+00,	-0.1043193E+12
118,	0.1179999E+01,	0.0000000E+00,	-0.1075627E+12
119,	0.1189999E+01,	0.0000000E+00,	-0.1068711E+12
120,	0.1199999E+01,	0.0000000E+00,	-0.1061708E+12
121,	0.1209999E+01,	0.0000000E+00,	-0.1061699E+12
122,	0.1219999E+01,	0.0000000E+00,	-0.1067969E+12
123,	0.1229999E+01,	0.0000000E+00,	-0.1079116E+12
124,	0.1239999E+01,	0.0000000E+00,	-0.1094830E+12
125,	0.1249999E+01,	0.0000000E+00,	-0.1113870E+12
126,	0.1259999E+01,	0.0000000E+00,	-0.1136098E+12
127,	0.1269999E+01,	0.0000000E+00,	-0.1143195E+12
128,	0.1279999E+01,	0.0000000E+00,	-0.1121116E+12
129,	0.1289999E+01,	0.0000000E+00,	-0.1108290E+12
130,	0.1299999E+01,	0.0000000E+00,	-0.1102807E+12
131,	0.1309999E+01,	0.0000000E+00,	-0.1099220E+12
132,	0.1319999E+01,	0.0000000E+00,	-0.1098230E+12
133,	0.1329999E+01,	0.0000000E+00,	-0.1102694E+12
134,	0.1339999E+01,	0.0000000E+00,	-0.1111079E+12
135,	0.1349999E+01,	0.0000000E+00,	-0.1123551E+12
136,	0.1359999E+01,	0.0000000E+00,	-0.1097641E+12
137,	0.1369999E+01,	0.0000000E+00,	-0.1072927E+12
138,	0.1379999E+01,	0.0000000E+00,	-0.1057065E+12
139,	0.1389999E+01,	0.0000000E+00,	-0.1047702E+12
140,	0.1399999E+01,	0.0000000E+00,	-0.1044542E+12
141,	0.1409999E+01,	0.0000000E+00,	-0.1046925E+12
142,	0.1419999E+01,	0.0000000E+00,	-0.1053320E+12
143,	0.1429999E+01,	0.0000000E+00,	-0.1064252E+12
144,	0.1439999E+01,	0.0000000E+00,	-0.1063023E+12
145,	0.1449999E+01,	0.0000000E+00,	-0.1040352E+12
146,	0.1459999E+01,	0.0000000E+00,	-0.1026196E+12
147,	0.1469999E+01,	0.0000000E+00,	-0.1018523E+12
148,	0.1479999E+01,	0.0000000E+00,	-0.1015660E+12
149,	0.1489999E+01,	0.0000000E+00,	-0.1017137E+12
150,	0.1499999E+01,	0.0000000E+00,	-0.1022470E+12
151,	0.1509999E+01,	0.0000000E+00,	-0.1032244E+12
152,	0.1519999E+01,	0.0000000E+00,	-0.1043863E+12
153,	0.1529999E+01,	0.0000000E+00,	-0.1017557E+12
154,	0.1539999E+01,	0.0000000E+00,	-0.9916832E+11
155,	0.1549999E+01,	0.0000000E+00,	-0.9731912E+11
156,	0.1559999E+01,	0.0000000E+00,	-0.9597935E+11
157,	0.1569999E+01,	0.0000000E+00,	-0.9515937E+11
158,	0.1579999E+01,	0.0000000E+00,	-0.9464363E+11
159,	0.1589999E+01,	0.0000000E+00,	-0.9453430E+11
160,	0.1599999E+01,	0.0000000E+00,	-0.9469862E+11
161,	0.1609999E+01,	0.0000000E+00,	-0.9360396E+11
162,	0.1619999E+01,	0.0000000E+00,	-0.8994859E+11
163,	0.1629999E+01,	0.0000000E+00,	-0.8712809E+11
164,	0.1639999E+01,	0.0000000E+00,	-0.8494269E+11
165,	0.1649999E+01,	0.0000000E+00,	-0.8327901E+11
166,	0.1659999E+01,	0.0000000E+00,	-0.8210561E+11
167,	0.1669999E+01,	0.0000000E+00,	-0.8137078E+11
168,	0.1679999E+01,	0.0000000E+00,	-0.8094341E+11
169,	0.1689999E+01,	0.0000000E+00,	-0.8078465E+11
170,	0.1699999E+01,	0.0000000E+00,	-0.7702814E+11
171,	0.1709999E+01,	0.0000000E+00,	-0.7367090E+11
172,	0.1719999E+01,	0.0000000E+00,	-0.7106485E+11
173,	0.1729999E+01,	0.0000000E+00,	-0.6901844E+11
174,	0.1739999E+01,	0.0000000E+00,	-0.6738437E+11
175,	0.1749999E+01,	0.0000000E+00,	-0.6619662E+11
176,	0.1759999E+01,	0.0000000E+00,	-0.6531858E+11
177,	0.1769999E+01,	0.0000000E+00,	-0.6469855E+11
178,	0.1779999E+01,	0.0000000E+00,	-0.6267630E+11
179,	0.1789999E+01,	0.0000000E+00,	-0.5831233E+11
180,	0.1799999E+01,	0.0000000E+00,	-0.5471103E+11

181,	0.1809999E+01,	0.0000000E+00,	-0.5198170E+11
182,	0.1819999E+01,	0.0000000E+00,	-0.4968528E+11
183,	0.1829999E+01,	0.0000000E+00,	-0.4780787E+11
184,	0.1839999E+01,	0.0000000E+00,	-0.4626101E+11
185,	0.1849999E+01,	0.0000000E+00,	-0.4495439E+11
186,	0.1859999E+01,	0.0000000E+00,	-0.4391259E+11
187,	0.1869999E+01,	0.0000000E+00,	-0.3945764E+11
188,	0.1879999E+01,	0.0000000E+00,	-0.3507214E+11
189,	0.1889999E+01,	0.0000000E+00,	-0.3136382E+11
190,	0.1899999E+01,	0.0000000E+00,	-0.2816220E+11
191,	0.1909999E+01,	0.0000000E+00,	-0.2575747E+11
192,	0.1919999E+01,	0.0000000E+00,	-0.2369095E+11
193,	0.1929999E+01,	0.0000000E+00,	-0.2183970E+11
194,	0.1939999E+01,	0.0000000E+00,	-0.2028450E+11
195,	0.1949998E+01,	0.0000000E+00,	-0.1749476E+11
196,	0.1959998E+01,	0.0000000E+00,	-0.1240921E+11
197,	0.1969998E+01,	0.0000000E+00,	-0.8099294E+10
198,	0.1979998E+01,	0.0000000E+00,	-0.4187734E+10
199,	0.1989998E+01,	0.0000000E+00,	-0.7387608E+09
200,	0.1999998E+01,	0.0000000E+00,	0.2441692E+10
201,	0.2009999E+01,	0.0000000E+00,	0.4752803E+10
202,	0.2019999E+01,	0.0000000E+00,	0.6783672E+10
203,	0.2029999E+01,	0.0000000E+00,	0.8573959E+10
204,	0.2039999E+01,	0.0000000E+00,	0.1358619E+11
205,	0.2049999E+01,	0.0000000E+00,	0.1844229E+11
206,	0.2059999E+01,	0.0000000E+00,	0.2256381E+11
207,	0.2069999E+01,	0.0000000E+00,	0.2624571E+11
208,	0.2079998E+01,	0.0000000E+00,	0.2998437E+11
209,	0.2089998E+01,	0.0000000E+00,	0.3305414E+11
210,	0.2099998E+01,	0.0000000E+00,	0.3583447E+11
211,	0.2109998E+01,	0.0000000E+00,	0.3785989E+11
212,	0.2119998E+01,	0.0000000E+00,	0.4105933E+11
213,	0.2129998E+01,	0.0000000E+00,	0.4628984E+11
214,	0.2139998E+01,	0.0000000E+00,	0.5073597E+11
215,	0.2149998E+01,	0.0000000E+00,	0.5476216E+11
216,	0.2159998E+01,	0.0000000E+00,	0.5849460E+11
217,	0.2169998E+01,	0.0000000E+00,	0.6191561E+11
218,	0.2179998E+01,	0.0000000E+00,	0.6492625E+11
219,	0.2189998E+01,	0.0000000E+00,	0.6766601E+11
220,	0.2199998E+01,	0.0000000E+00,	0.7017015E+11
221,	0.2209998E+01,	0.0000000E+00,	0.7480060E+11
222,	0.2219998E+01,	0.0000000E+00,	0.7954028E+11
223,	0.2229998E+01,	0.0000000E+00,	0.8347950E+11
224,	0.2239998E+01,	0.0000000E+00,	0.8686977E+11
225,	0.2249998E+01,	0.0000000E+00,	0.9036680E+11
226,	0.2259998E+01,	0.0000000E+00,	0.9335793E+11
227,	0.2269998E+01,	0.0000000E+00,	0.9589259E+11
228,	0.2279998E+01,	0.0000000E+00,	0.9815450E+11
229,	0.2289998E+01,	0.0000000E+00,	0.1018077E+12
230,	0.2299998E+01,	0.0000000E+00,	0.1066648E+12
231,	0.2309998E+01,	0.0000000E+00,	0.1102217E+12
232,	0.2319998E+01,	0.0000000E+00,	0.1133184E+12
233,	0.2329998E+01,	0.0000000E+00,	0.1159983E+12
234,	0.2339998E+01,	0.0000000E+00,	0.1185991E+12
235,	0.2349998E+01,	0.0000000E+00,	0.1210217E+12
236,	0.2359998E+01,	0.0000000E+00,	0.1234114E+12
237,	0.2369998E+01,	0.0000000E+00,	0.1253028E+12
238,	0.2379998E+01,	0.0000000E+00,	0.1279569E+12
239,	0.2389998E+01,	0.0000000E+00,	0.1308086E+12
240,	0.2399998E+01,	0.0000000E+00,	0.1333731E+12
241,	0.2409998E+01,	0.0000000E+00,	0.1356778E+12
242,	0.2419998E+01,	0.0000000E+00,	0.1377247E+12
243,	0.2429998E+01,	0.0000000E+00,	0.1395345E+12
244,	0.2439998E+01,	0.0000000E+00,	0.1411102E+12
245,	0.2449998E+01,	0.0000000E+00,	0.1426161E+12

246,	0.2459998E+01,	0.0000000E+00,	0.1441824E+12
247,	0.2469998E+01,	0.0000000E+00,	0.1684876E+12
248,	0.2479998E+01,	0.0000000E+00,	0.5846469E+12
249,	0.2489998E+01,	0.0000000E+00,	0.7742568E+13
250,	0.2499998E+01,	0.1700331E+15,	0.1671914E+15
251,	0.2509998E+01,	0.0000000E+00,	0.0000000E+00
252,	0.2519998E+01,	0.0000000E+00,	0.0000000E+00
253,	0.2529998E+01,	0.0000000E+00,	0.0000000E+00
254,	0.2539998E+01,	0.0000000E+00,	0.0000000E+00
255,	0.2549998E+01,	0.0000000E+00,	0.0000000E+00
256,	0.2559998E+01,	0.0000000E+00,	0.0000000E+00
257,	0.2569998E+01,	0.0000000E+00,	0.0000000E+00
258,	0.2579998E+01,	0.0000000E+00,	0.0000000E+00
259,	0.2589998E+01,	0.0000000E+00,	0.0000000E+00
260,	0.2599998E+01,	0.0000000E+00,	0.0000000E+00
261,	0.2609998E+01,	0.0000000E+00,	0.0000000E+00
262,	0.2619998E+01,	0.0000000E+00,	0.0000000E+00
263,	0.2629998E+01,	0.0000000E+00,	0.0000000E+00
264,	0.2639998E+01,	0.0000000E+00,	0.0000000E+00
265,	0.2649998E+01,	0.0000000E+00,	0.0000000E+00
266,	0.2659998E+01,	0.0000000E+00,	0.0000000E+00
267,	0.2669998E+01,	0.0000000E+00,	0.0000000E+00
268,	0.2679998E+01,	0.0000000E+00,	0.0000000E+00
269,	0.2689998E+01,	0.0000000E+00,	0.0000000E+00
270,	0.2699998E+01,	0.0000000E+00,	0.0000000E+00
271,	0.2709998E+01,	0.0000000E+00,	0.0000000E+00
272,	0.2719998E+01,	0.0000000E+00,	0.0000000E+00
273,	0.2729998E+01,	0.0000000E+00,	0.0000000E+00
274,	0.2739998E+01,	0.0000000E+00,	0.0000000E+00
275,	0.2749998E+01,	0.0000000E+00,	0.0000000E+00
276,	0.2759998E+01,	0.0000000E+00,	0.0000000E+00
277,	0.2769998E+01,	0.0000000E+00,	0.0000000E+00
278,	0.2779998E+01,	0.0000000E+00,	0.0000000E+00
279,	0.2789998E+01,	0.0000000E+00,	0.0000000E+00
280,	0.2799998E+01,	0.0000000E+00,	0.0000000E+00
281,	0.2809998E+01,	0.0000000E+00,	0.0000000E+00
282,	0.2819998E+01,	0.0000000E+00,	0.0000000E+00
283,	0.2829998E+01,	0.0000000E+00,	0.0000000E+00
284,	0.2839998E+01,	0.0000000E+00,	0.0000000E+00
285,	0.2849998E+01,	0.0000000E+00,	0.0000000E+00
286,	0.2859998E+01,	0.0000000E+00,	0.0000000E+00
287,	0.2869998E+01,	0.0000000E+00,	0.0000000E+00
288,	0.2879998E+01,	0.0000000E+00,	0.0000000E+00
289,	0.2889998E+01,	0.0000000E+00,	0.0000000E+00
290,	0.2899998E+01,	0.0000000E+00,	0.0000000E+00
291,	0.2909998E+01,	0.0000000E+00,	0.0000000E+00
292,	0.2919998E+01,	0.0000000E+00,	0.0000000E+00
293,	0.2929998E+01,	0.0000000E+00,	0.0000000E+00
294,	0.2939998E+01,	0.0000000E+00,	0.0000000E+00
295,	0.2949998E+01,	0.0000000E+00,	0.0000000E+00
296,	0.2959998E+01,	0.0000000E+00,	0.0000000E+00
297,	0.2969998E+01,	0.0000000E+00,	0.0000000E+00
298,	0.2979998E+01,	0.0000000E+00,	0.0000000E+00
299,	0.2989998E+01,	0.0000000E+00,	0.0000000E+00
300,	0.2999998E+01,	0.0000000E+00,	0.0000000E+00
Total	,	0.1700331E+15,	0.1690850E+15

Rod Withdrawal with Improved Shape-factors Error

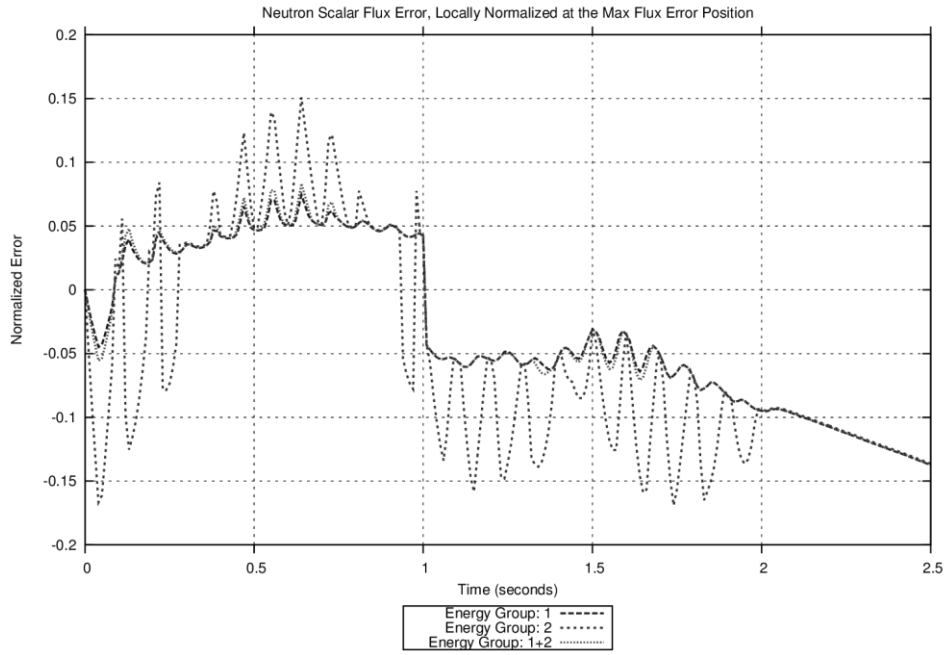

Figure 92: 2 second rod withdrawal transient maximum flux error, 0.05 second projection operator set.

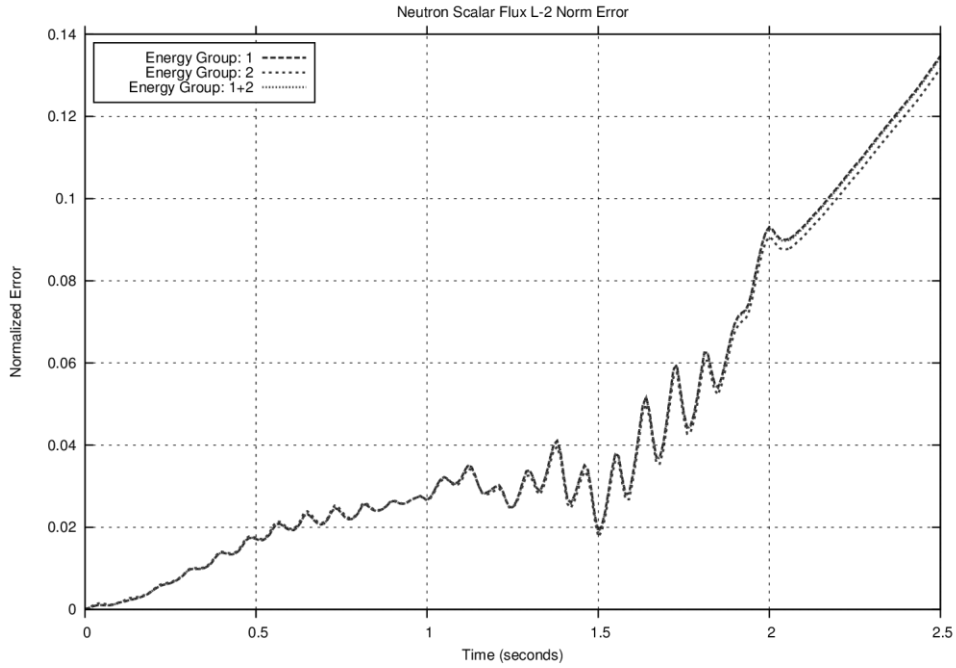

Figure 93: 2 second rod withdrawal transient RMS flux error, 0.05 second projection operator set.

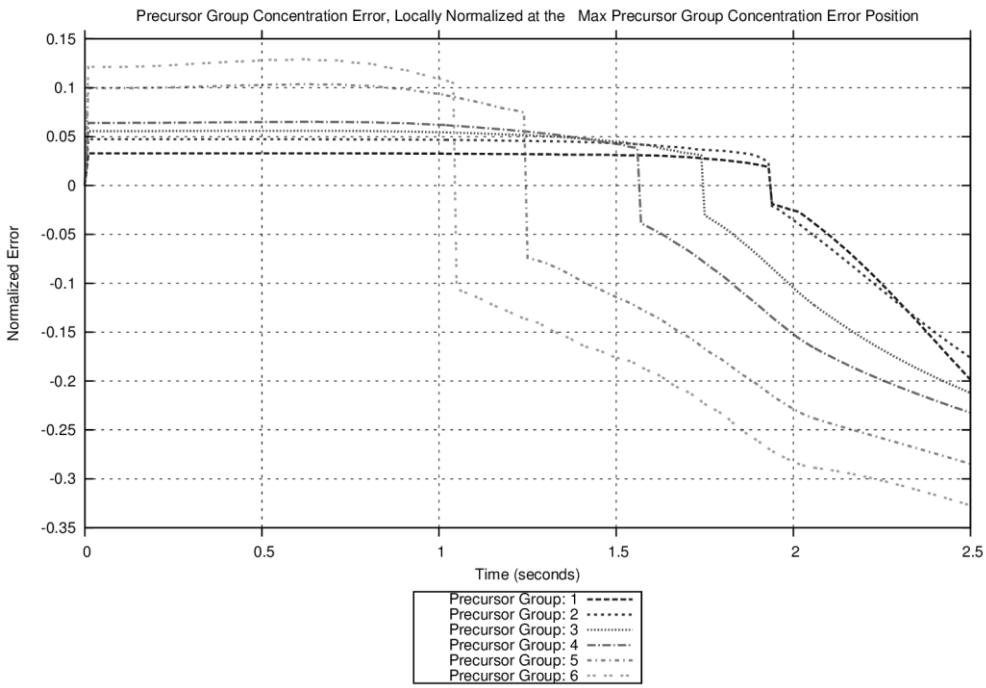

Figure 94: 2 second rod withdrawal transient maximum precursor error, 0.05 second projection operator set.

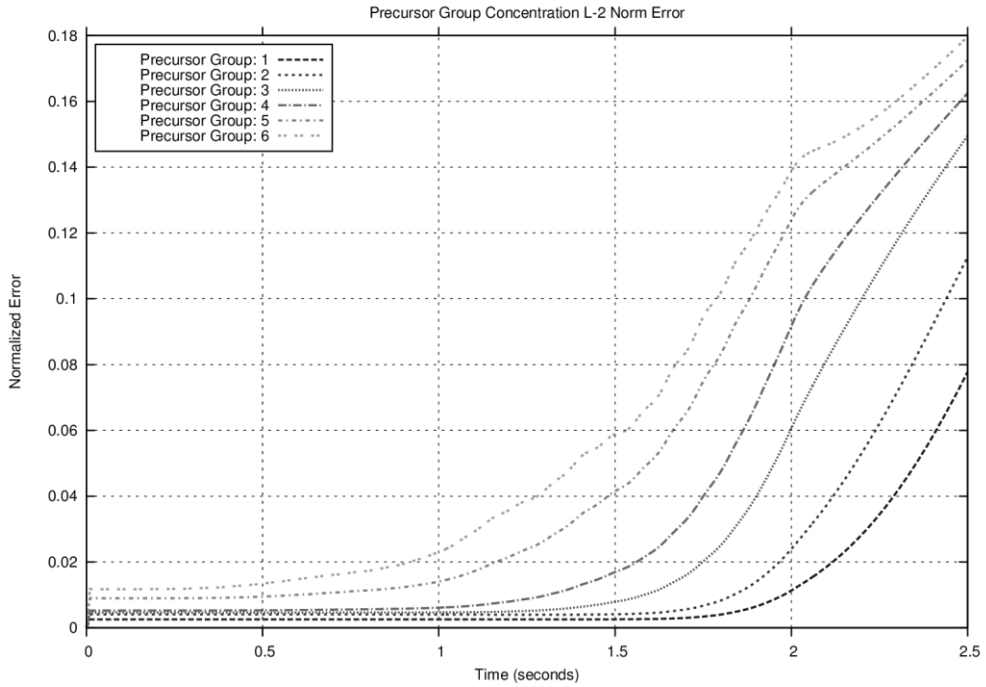

Figure 95: 2 second rod withdrawal transient RMS precursor error, 0.05 second projection operator set.

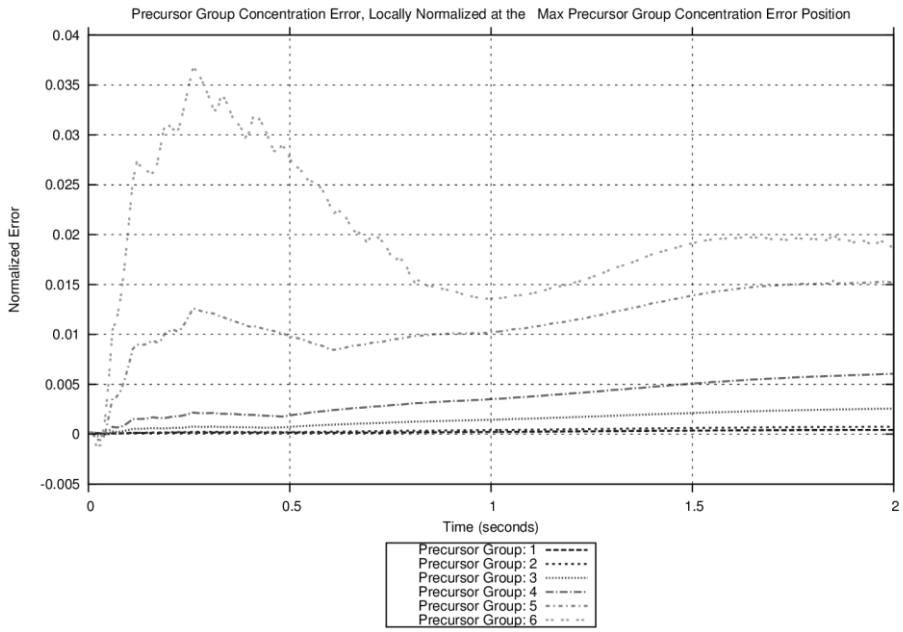

Figure 96: Maximum DNP error, 2 second transient, normal beta values, high frequency 0.05 second projection operator set.

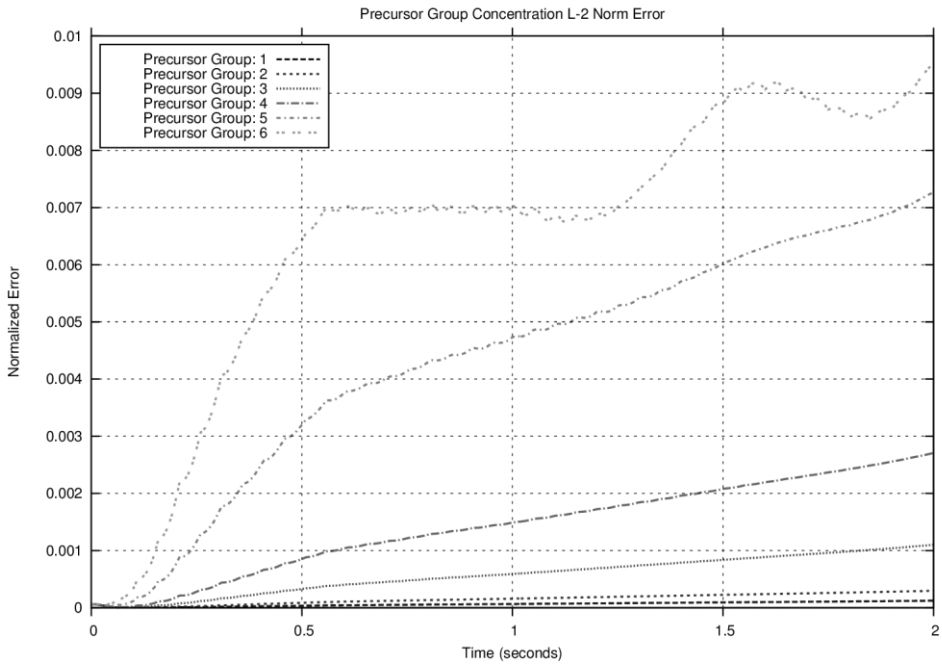

Figure 97: RMS precursor error, 2 second transient, normal beta values, high frequency 0.05 second projection operator set.

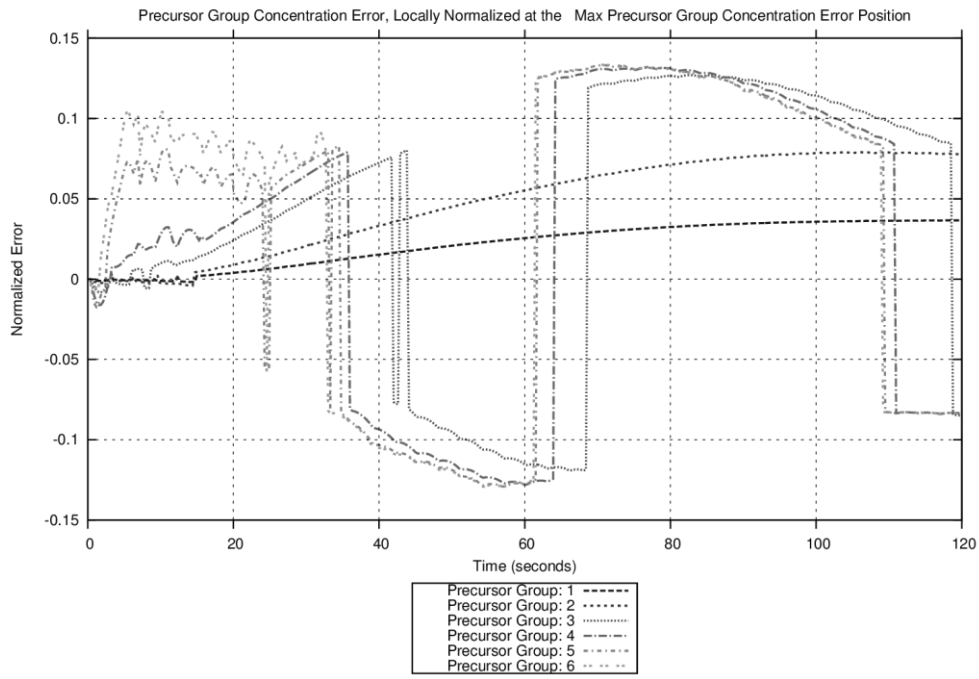

Figure 98: Maximum DNP error, 120 second transient, normal beta values, high frequency 0.05 second projection operator set.

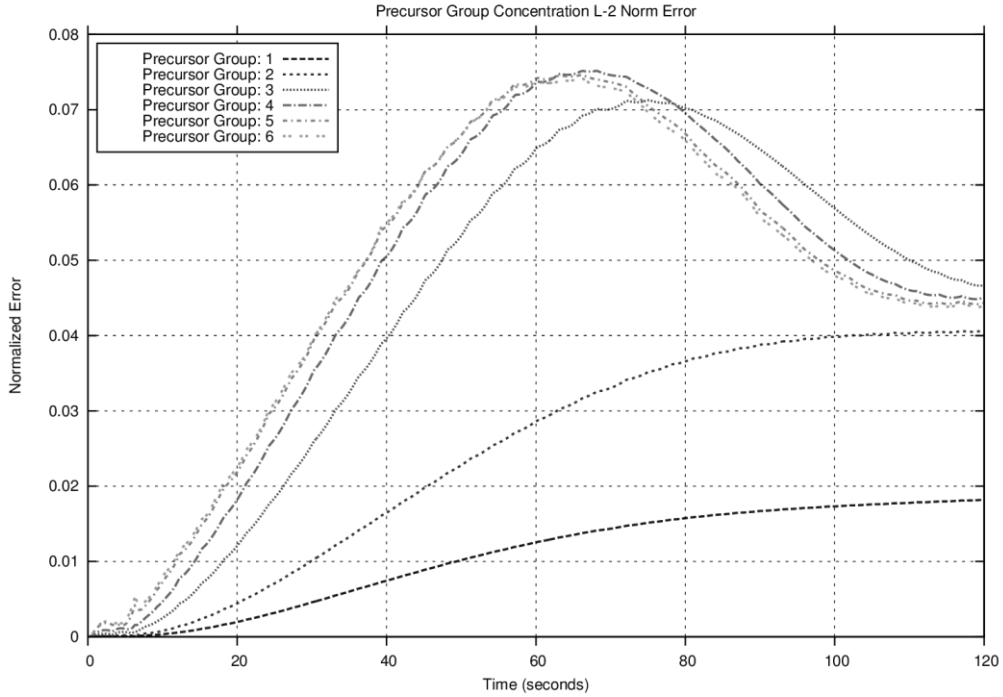

Figure 99: RMS precursor error, 120 second transient, normal beta values, high frequency 0.05 second projection operator set.

3-D Flux Shape Errors

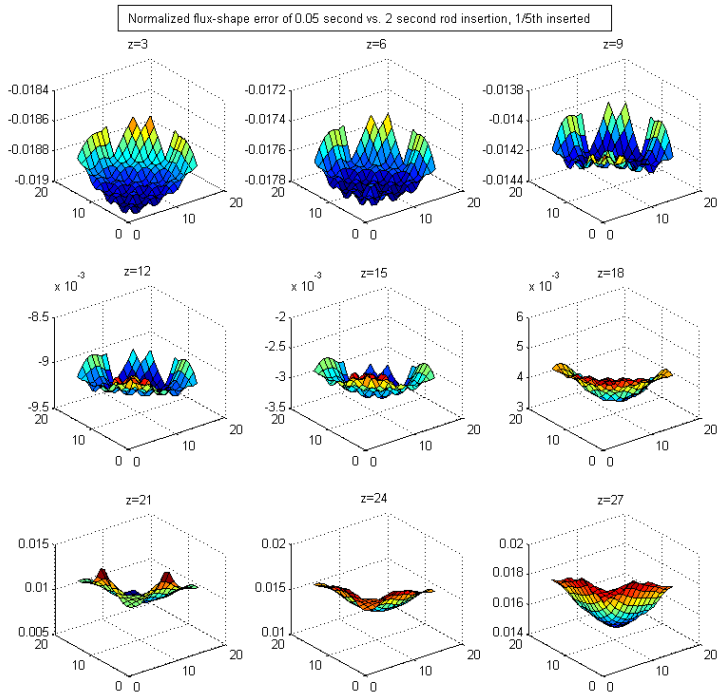

Figure 100: Normalized flux shape error, 2 second transient, 0.05 lo-fi, rods 1/5 inserted.

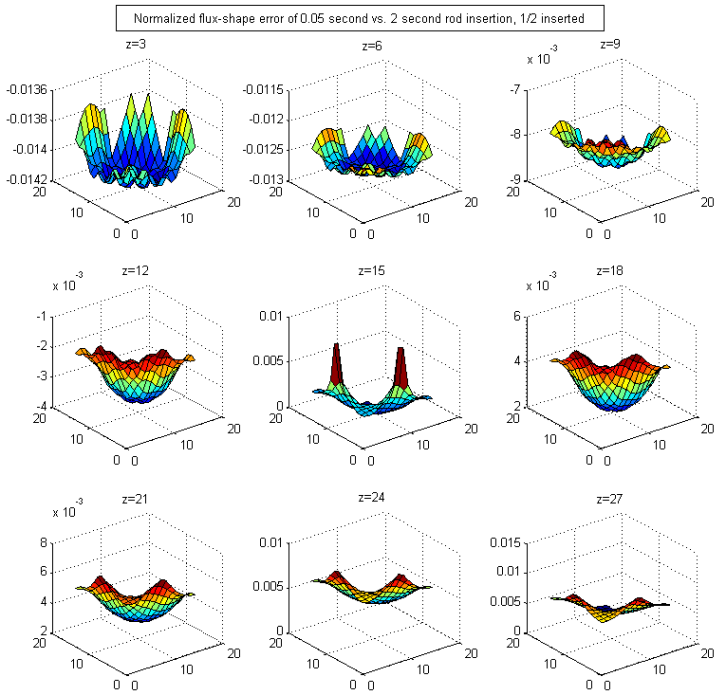

Figure 101: Normalized flux shape error, 2 second transient, 0.05 lo-fi, rods ½ inserted.

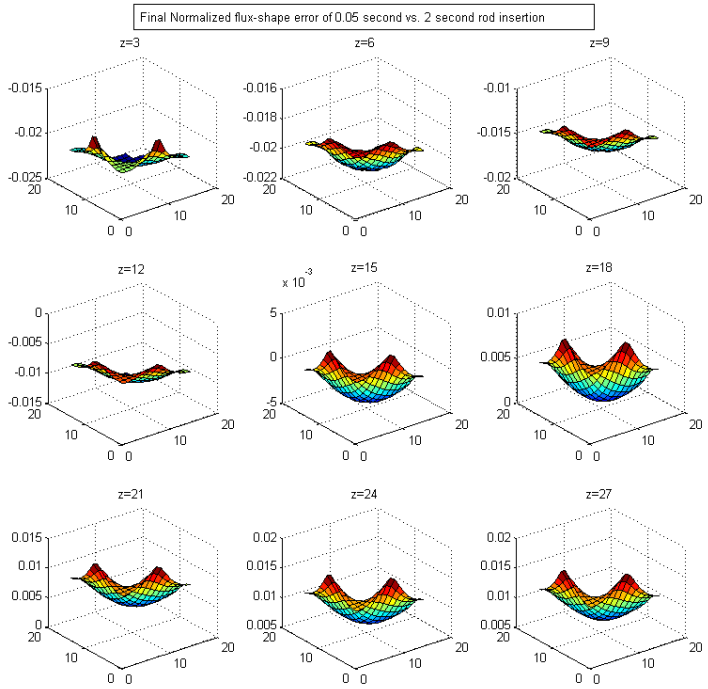

Figure 102: Normalized flux shape error, 2 second transient, 0.05 lo-fi, rods fully inserted.

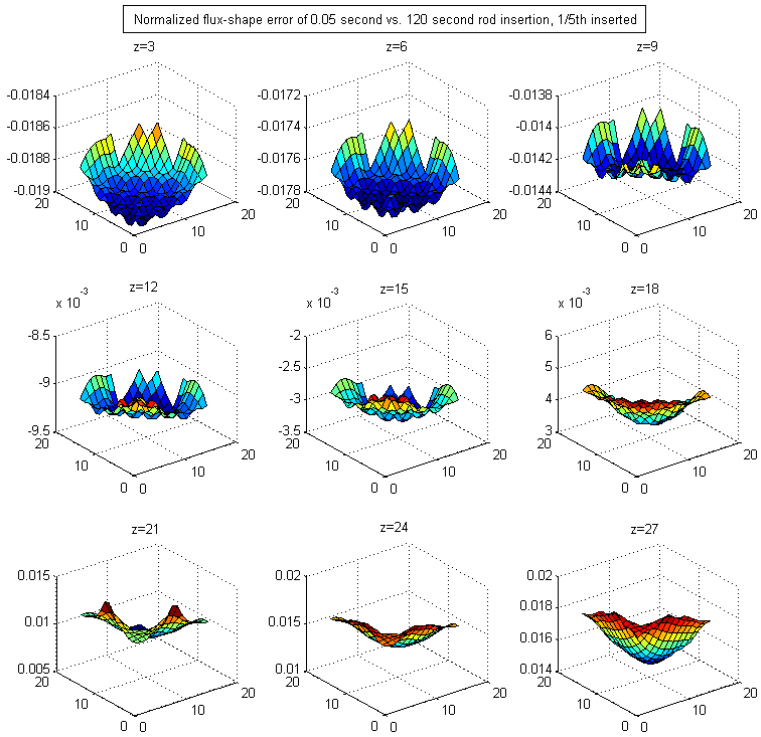

Figure 103: Normalized flux shape error, 120 second transient, 0.05 lo-fi, rods 1/5 inserted.

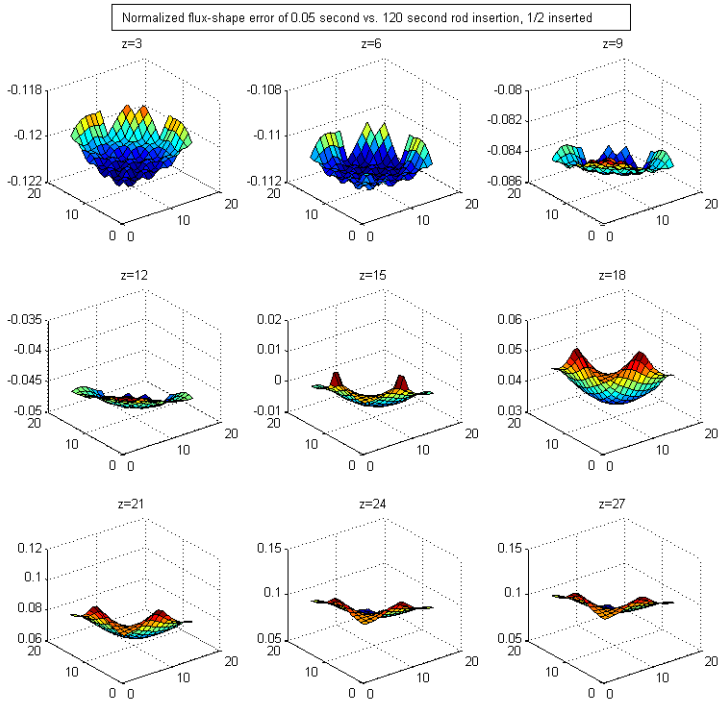

Figure 104: Normalized flux shape error, 120 second transient, 0.05 lo-fi, rods ½ inserted.

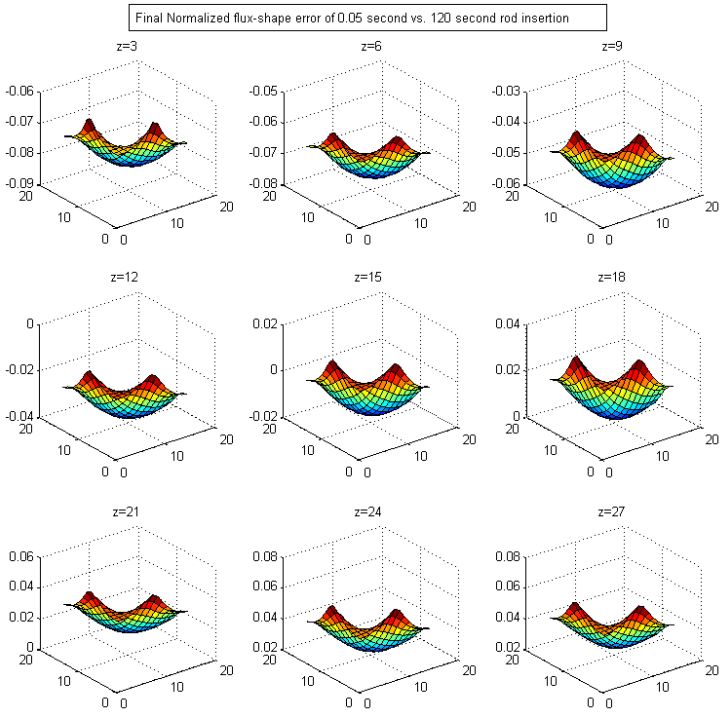

Figure 105: Normalized flux shape error, 120 second transient, 0.05 lo-fi, rods fully inserted.

3-D Delayed Neutron Production Deltas

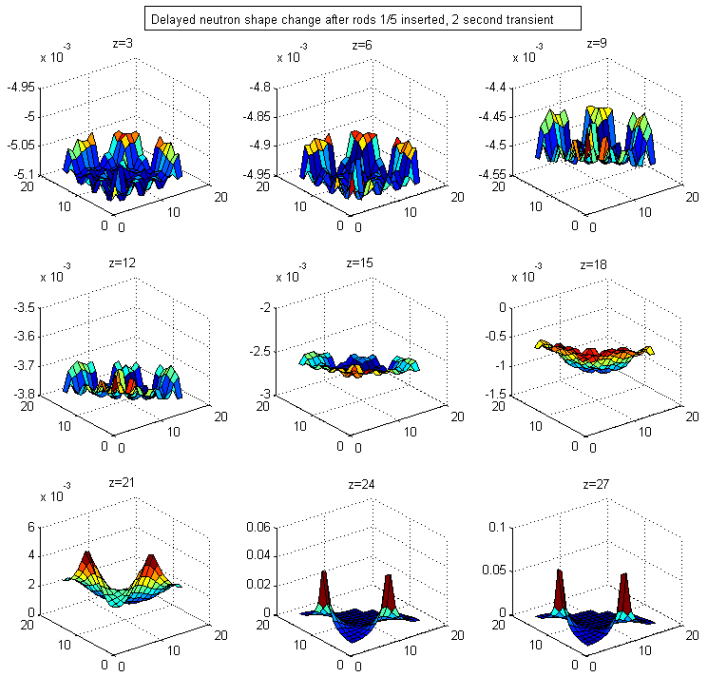

Figure 106: Normalized delayed neutron shape delta, 2 second transient, rods 1/5 inserted.

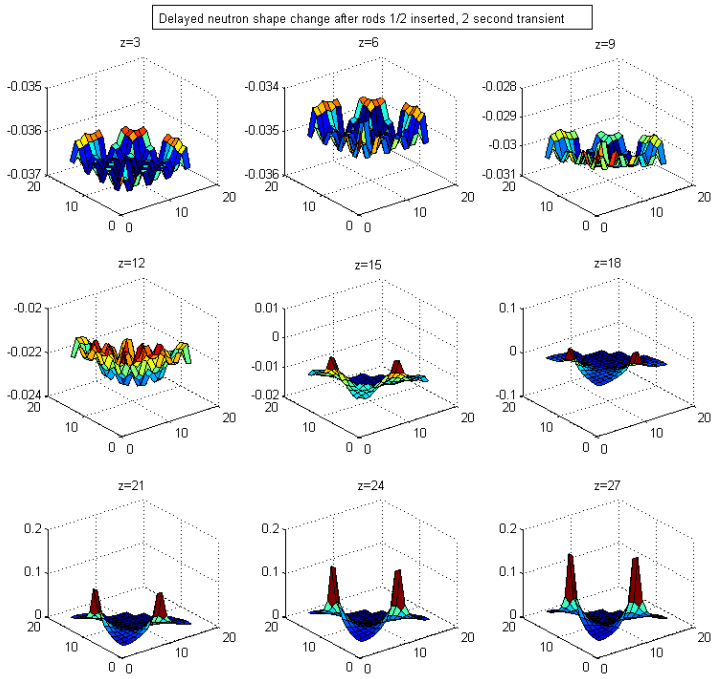

Figure 107: Normalized delayed neutron shape delta, 2 second transient, rods ½ inserted.

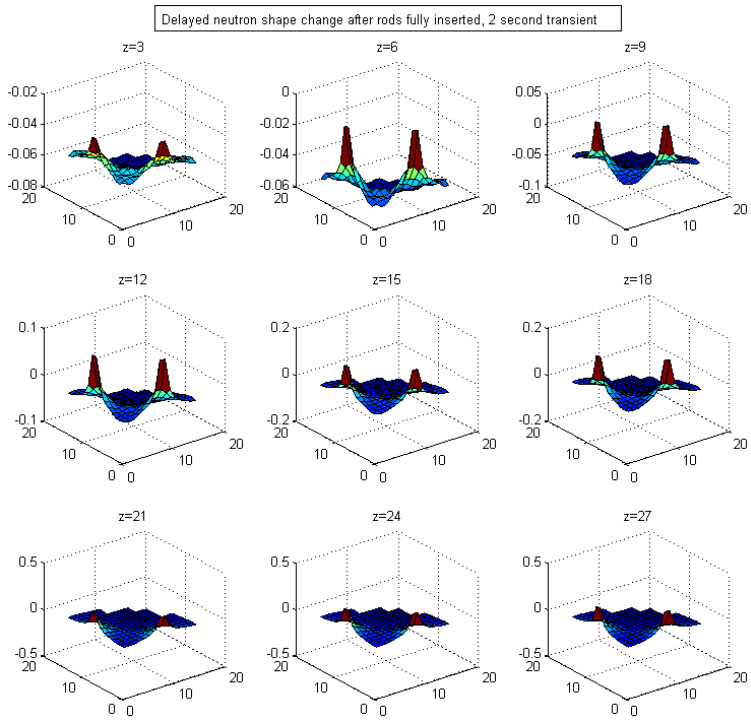

Figure 108: Normalized delayed neutron shape delta, 2 second transient, rods fully inserted.

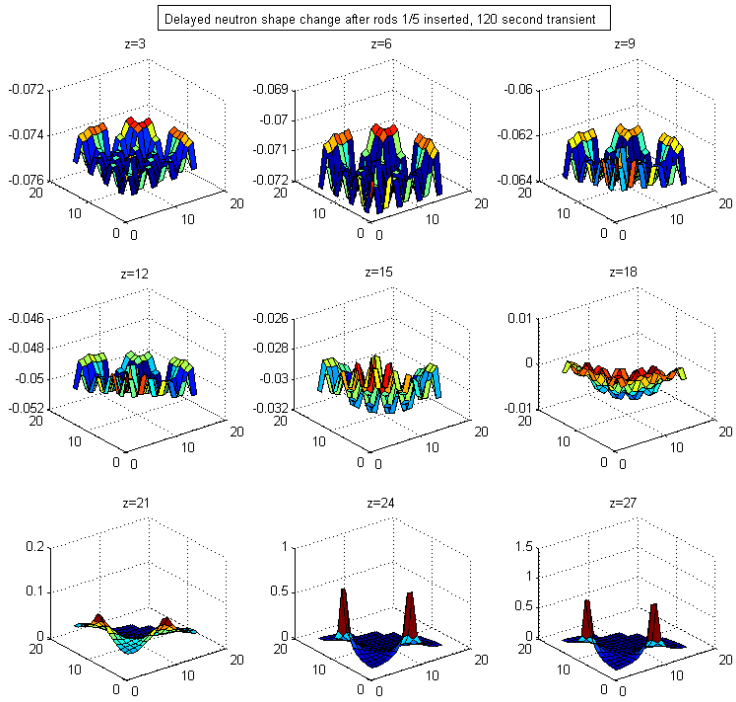

Figure 109: Normalized delayed neutron shape delta, 120 second transient, rods 1/5 inserted.

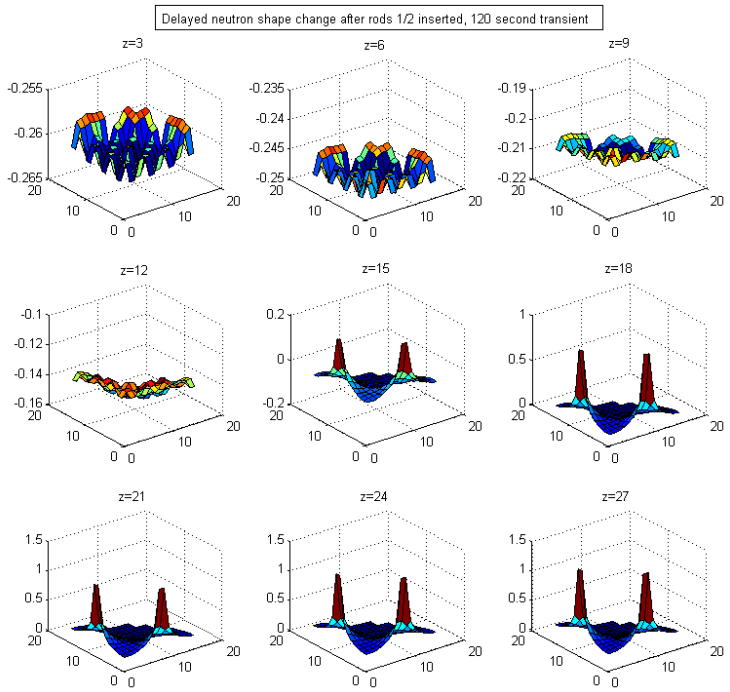

Figure 110: Normalized delayed neutron shape delta, 120 second transient, rods ½ inserted.

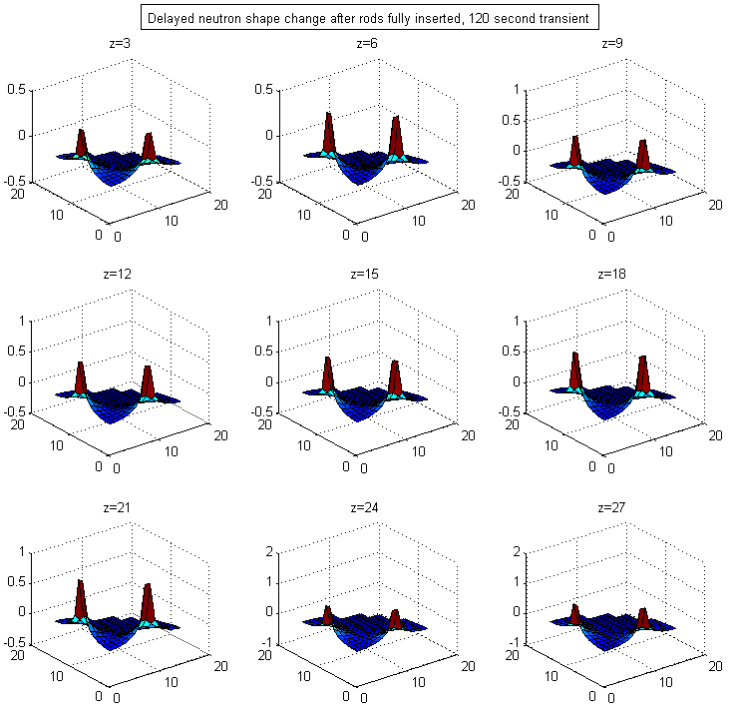

Figure 111: Normalized delayed neutron shape delta, 120 second transient, rods fully inserted.

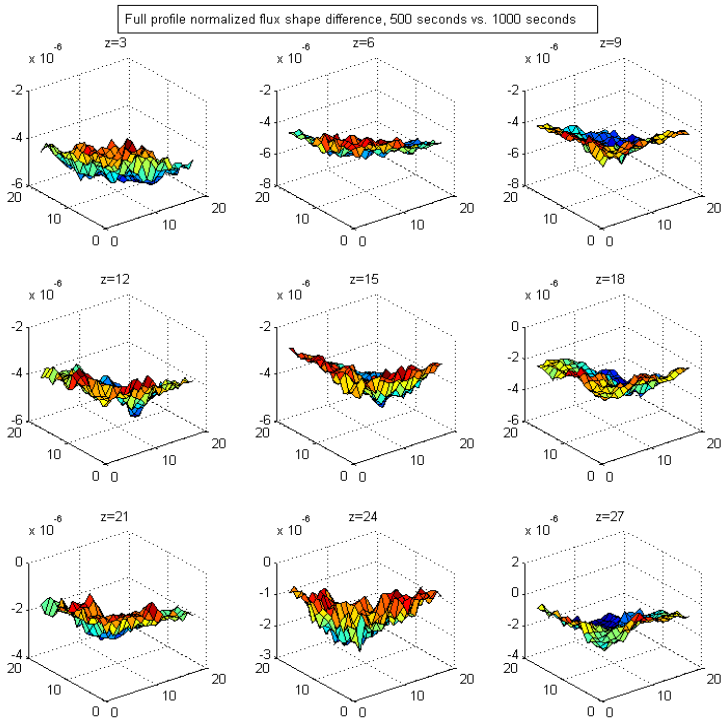

Figure 112: Normalized difference in radial flux shape, including non-fueled regions, at various axial heights at 500 seconds versus 1000 seconds..

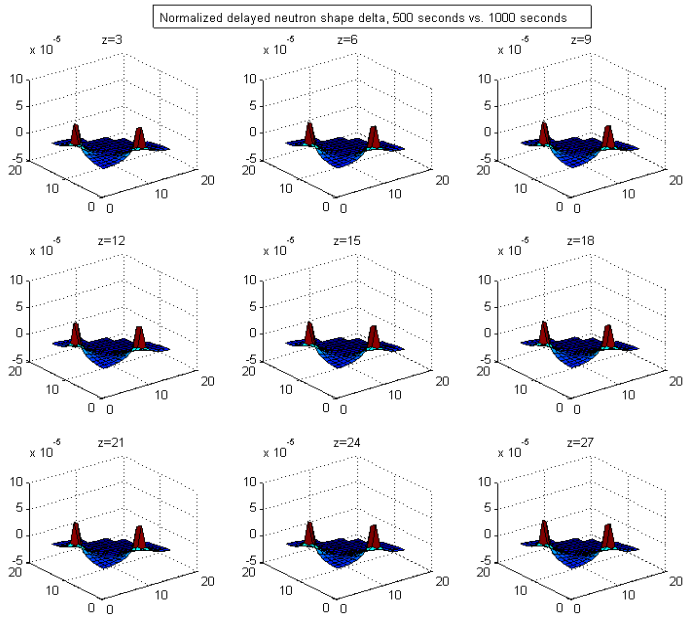

Figure 113: Normalized difference in radial delayed neutron production distribution, at various axial heights at 0.02 seconds versus 1000 seconds.